Scuola Internazionale Superiore di Studi Avanzati - Trieste

SISSA 40!

Purinergic Calcium Signaling and Calcium-Activated Chloride Channels in the Supporting Cells of the Peripheral Olfactory Systems

Thesis submitted for the degree of
"Doctor Philosophiae"

Academic Year 2017/2018

Candidate

Tiago André Ferreira Henriques

Supervisors:

Prof. Anna Menini

Dott. Simone Pifferi

SISSA - Via Bonomea 265 - 34136 TRIESTE - ITALY

Scuola Internazionale Superiore di Studi Avanzati, SISSA

International School for Advanced Studies

Trieste, Italy

Purinergic Calcium Signaling and Calcium-Activated Chloride Channels in the Supporting Cells of the Peripheral Olfactory Systems

Thesis submitted for the degree of
"Doctor Philosophiae"

Academic Year 2017/2018

Candidate

Tiago André Ferreira Henriques

Supervisors:

Prof. Anna Menini

Dott. Simone Pifferi

Acknowledgements

Dedico esta dissertação aos meus pais Carlos Henriques e Cristiana Henriques, esta tese é igual parte resultado do esforço deles, de todo o suor e lágrimas e alegrias, como é dos últimos quatro anos que dediquei a este trabalho. É graças a eles e aos seus sacrifícios para me darem uma educação, de suportarem e incentivarem os meus sonhos, que hoje este manuscrito esta perante vós, o leitor, e do mundo. Obrigado Mãe e Pai.

Gostava de agradecer também aos meus supervisores, a Professora Anna Menini e o Doutor Simone Pifferi, com quem tive o privilegio de trabalhar e por quem tenho o maior respeito e admiração, o seu rigor cientifico e dedicação marcaram me muito e vou ter-los sempre como inspiração e exemplo a seguir.

Obrigado aos meus mentores e amigos Andres Hernandez, Devendra Maurya e Gianluca Pietra pela paciência, nunca aprendi tanto na vida como quando tive a sorte de trabalhar convosco.

Aos grandes amigos amigos de Portugal, Alexandre, Caramelo, Paulo, Ricardo, Daniela, obrigado por me ensinarem a sonhar.

A todos os novos amigos de Trieste, aos que ainda cá estão e aos que partiram à procura de pastos mais verdes. Obrigado Isidro, Juan, Elena, Stefano, Ulisse, Raquel, Kevin, Abraham, Chiara, Pin-Jane, Mangesh, Negar, Diletta, Richard, Nika, e claro, uma beijo especial para a minha Phuong.

Abstract

This study is divided in three individual projects focusing on calcium signaling on non-neuronal cells of different peripheral olfactory systems. In particular, I investigated (1) the role of calcium-activated chloride channel TMEM16A in the development of the mouse olfactory epithelium, (2) the functional role of TMEM16A of mouse olfactory epithelium and (3) purinergic receptor mediated calcium signaling in the supporting cells of the vomeronasal organ (VNO).

Previous reports showed that TMEM16A is expressed in the olfactory epithelium, where it localizes at the apical surface of supporting cells, more specifically, in their microvilli. To understand the role of TMEM16A on the development of the mouse olfactory epithelium we conducted the first immunohistochemistry study comparing the morphological properties of the olfactory epithelium and nasal glands in TMEM16A wild-type and knockout littermate mice. The genetic ablation of TMEM16A did not affect the maturation of olfactory sensory neurons and the morphology of the ciliary structures. In addition, TMEM16A knockout did not significantly affect the morphology of supporting cells. The average number of supporting cells, olfactory sensory neurons, horizontal and globose basal cells were not significantly different in the two mice models. These results indicate that the genetic ablation of TMEM16A does not affect the development of the olfactory epithelium.

To further understand the functional role of TMEM16A, we investigated the presence of calcium-activated chloride currents in the supporting cells of the olfactory epithelium. Whole-cell patch clamp recordings from TMEM16A wild-type and knockout mice showed that the supporting cells of olfactory epithelium had a calcium-activated chloride current that was abolished in TMEM16A knockout mice. Moreover, we found that this calcium-activated currents can also be activated after the stimulation of the cells with ATP, in line with previous reports showing that supporting cells of mouse olfactory epithelium express purinergic receptors.

Although the expression of purinergic receptors in supporting cells in the mouse olfactory epithelium is well documented, the expression of these receptors in mouse VNO is still unknown.

Abstract

Here, we conducted the first study in mouse VNO showing that vomeronasal supporting cells also express purinergic ATP receptors. Using confocal calcium imaging recording we found that a large subset of these cells, about 75%, expressed metabotropic purinergic receptors, and a smaller subset of cells, 38%, expressing P2Y2 and/or P2Y4 receptors.

Table of Contents

1. Introduction

1.1. Anatomy and histology of the main olfactory epithelium and vomeronasal organ

The olfactory epithelium and the vomeronasal organ (VNO) are both tissues of the peripheral olfactory system that reside in the nasal cavity of most vertebrates (Figure 1). In mice, the olfactory epithelium and VNO differentiate from the olfactory placode. The olfactory placode is created from the neural tube and invaginates to form the olfactory pit, which progressively deepens, eventually forming the nasal cavity and nostrils. By embryonic day 11, the VNO forms in medial region of the nasal cavity and at embryonic day 13 the main olfactory epithelium and VNO are fully separated and easily distinguishable (Suzuki and Osumi, 2015; Zancanaro et al., 2002).

Odor molecules can reach the nasal cavity either through the nostrils during inhalation or through the nasopharynx when chewing and swallowing pushes the air back to the nasal cavity (Linforth et al., 2002).

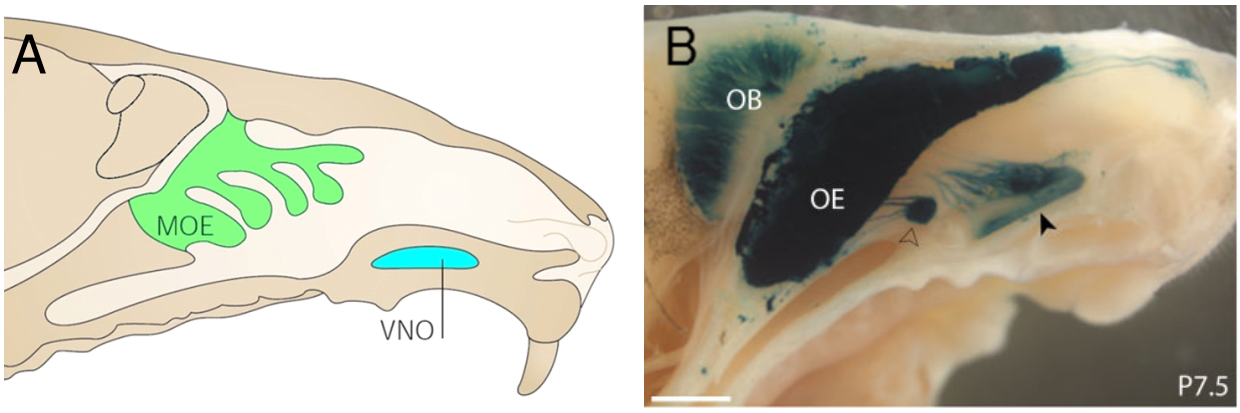

Figure 1. Anatomy of the olfactory epithelium. (A) Schematic representation of a sagittal section of the nasal cavity. The main olfactory epithelium (MOE) is in green, while the vomeronasal organ (VNO) is highlighted in cyan. Adapted from **(Mombaerts, 2004; Storan and Key, 2006)**. **(B)** Whole mount X-gal staining of sagittal section of head from of OMP:tau-LacZ transgenic mouse. In this mouse model, OMP is replaced by tau-Lac-Z, so all sensory neurons, which are part of the peripheral olfactory system are visualized with X-gal staining in blue. Main olfactory epithelium (MOE), olfactory bulb (OB), vomeronasal organ (VNO). Scale bar 500 µm Adapted from Storan and Key, 2006.

1.1.1. Olfactory epithelium

The main olfactory epithelium is a tissue in the nasal cavity responsible for the detection of odorants. It is a pseudo-stratified epithelium and is composed of olfactory sensory neurons, supporting cells, globose basal cells, horizontal basal cells, microvillar cells and the Bowman's gland duct cells (Figure 2) (Choi and Goldstein, 2018; Fletcher et al., 2017; Shipley and Ennis, 1996). The axons of the olfactory sensory neurons project to the glomeruli of the olfactory bulb, connecting the peripheral olfactory system to the central olfactory system (Tirindelli et al., 2009).

The olfactory epithelium is easily distinguishable from the surrounding respiratory epithelium due to its larger thickness, which varies from species to species, ranging from 30 µm in moles (Graziadei, 1966) to 150 µm in alligators (Hansen, 2007). The epithelial surface is usually covered by a layer of mucus 10 to 40 µm thick (Solbu and Holen, 2012).

Olfactory sensory neurons are responsible for olfactory transduction, binding odorants and converting chemical signals into electrical ones. They are bipolar neurons, with a dendrite reaching to the surface of the tissue ending in a knob-like structure that projects dozens of cilia, where the sensory apparatus is located (Pifferi et al., 2010).

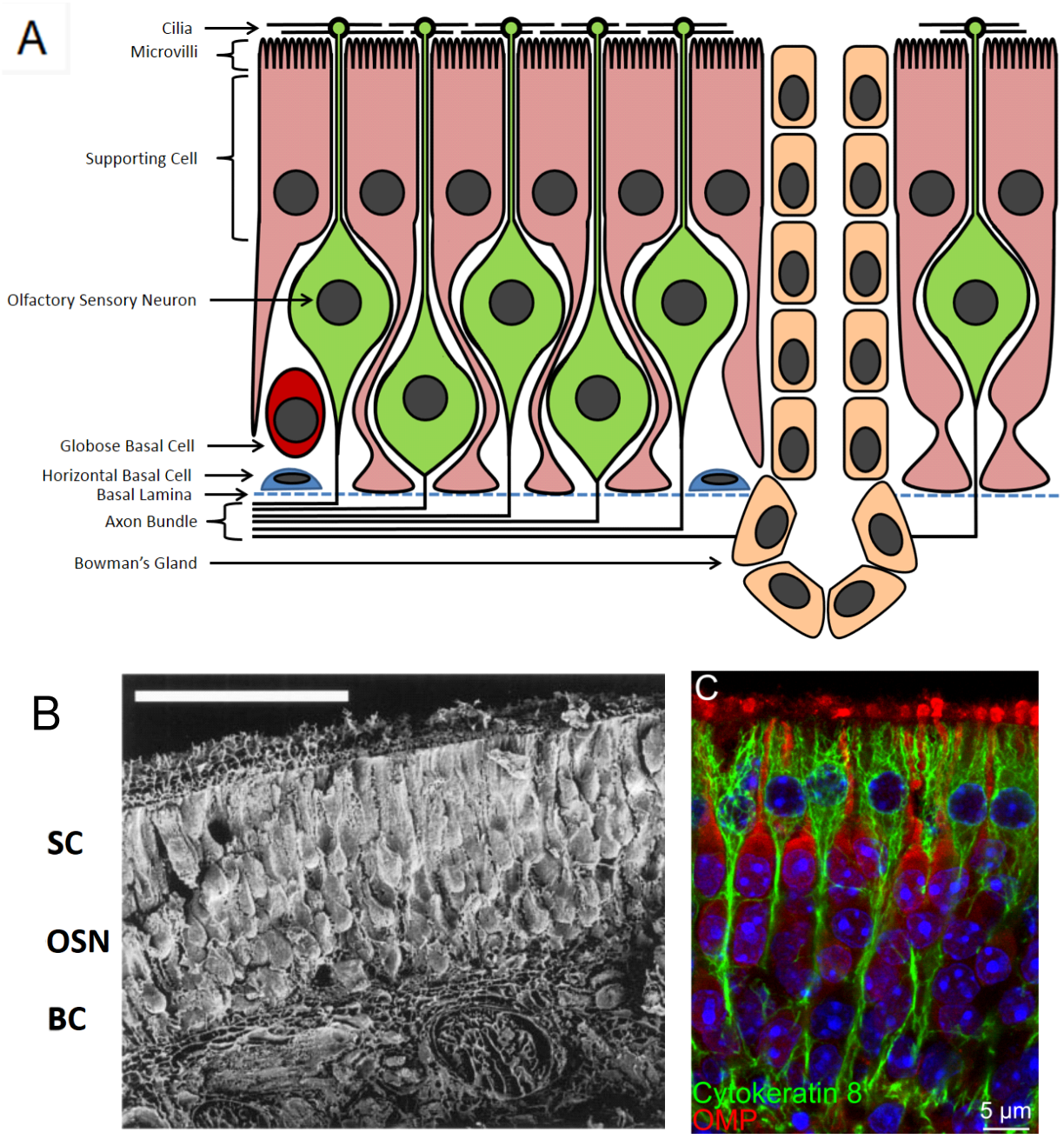

Figure 2. Histological organization of the olfactory epithelium. (A) Schematic representation of the cellular organization of the olfactory epithelium. Supporting cells are highlighted in pink, olfactory sensory neurons in green, globose basal cells in red, horizontal basal cells in blue, and the Bowman's gland in light orange. **(B)** Scanning electron micrograph of the olfactory epithelium showing a monolayer of supporting cells (SC), the somata of olfactory sensory neurons (OSN), and basal cells (BC). Scale: 100 µm. Adapted from Reuter et al., 1998. **(C)** Immunohistochemical staining of the olfactory epithelium, with an antibody for cytokeratin 8 labelling supporting cells (green) and olfactory sensory neurons marked with an antibody for olfactory marker protein, OMP (red). Adapted from Maurya et al., 2015.

Supporting cells share properties of both glial cells and epithelial cells, and have been shown to be involved in xenobiotic metabolism and phagocytosis of dead neurons (Suzuki et al., 1996; Zhuo et al., 2004). Supporting cells have a goblet-shaped cell body with processes extending to the basal lamina. The cell bodies of the supporting cells form a columnar monolayer on the most apical part of the olfactory epithelium. Many microvilli protrude towards the luminal surface, where they intermingle with the cilia of olfactory sensory neurons, completely covering the surface of the olfactory epithelium (Figure 2B-C).

Unlike other neural tissues, the olfactory epithelium regenerates throughout the lifespan of the animal. Indeed, there is a continuous turnover of olfactory sensory neurons (Graziadei et al., 1978; Mackay-Sim and Kittel, 1991), and neurons die at all stages of differentiation in physiological conditions (Mahalik, 1996). The cells responsible for this continuous replenishment of olfactory sensory neurons are called basal cells and they can be divided in two groups: globose and horizontal basal cells (Chen et al., 2004; Suzuki et al., 2013).

Globose basal cells are a multipotent stem cell population that can differentiate into both neurons and microvillar cells. Horizontal basal cells are multipotent, quiescent cells that can either differentiate directly into supporting cells or into globose basal cells, which subsequently differentiate into neurons or microvillar cells (Fletcher et al., 2017; Suzuki et al., 2013).

The olfactory epithelium of all vertebrates except for fish have a group of tubulo-alveolar glands called Bowman's gland (Eisthen, 1992), with the alveolar section located in the underlying connective tissue while their ducts extend to the apical surface of the tissue. These structures are responsible for the production of mucus; indeed, they are involved both in the transport of water to the lumen and in the production of mucin, which regulates the viscosity of the mucus (Solbu and Holen, 2012).

Microvillar cells are less abundant than supporting cells and neurons. They are located in the apical part of the olfactory epithelium and can be identified by their preeminent microvilli. They have been shown to produce neuropeptide Y and acetylcholine, both potential peripheral modulators of olfaction (Elsaesser and Paysan, 2007; Lucero, 2013; Montani et al., 2006).

1.1.2. Vomeronasal organ

The vomeronasal organ (VNO) is a mirrored tubular structure located at the base of the nasal septum. This organ is distinctively separated from the nasal cavity in most amphibians, reptiles and non-primate mammals, but it is absent in birds, apes and some monkeys (Swaney and Keverne, 2009). The VNO is enclosed in a capsule of cartilage and opens through a duct to the base of the nasal cavity. However, in some species, such as carnivores and ungulates, it is instead connected to the oral cavity (Keverne, 1999).

The sensory part of the VNO, also called vomeronasal sensory epithelium, is located in the medial section of the two crescent-shaped tubules. This sensory epithelium is composed of neurons, supporting cells and basal cells (Figure 3).

The vomeronasal sensory epithelium is responsible for the detection of pheromones, which are defined as molecules produced and released into the environment by an animal, affecting the behavior or physiology of members of its own species (Francia et al., 2014; Tirindelli et al., 2009).

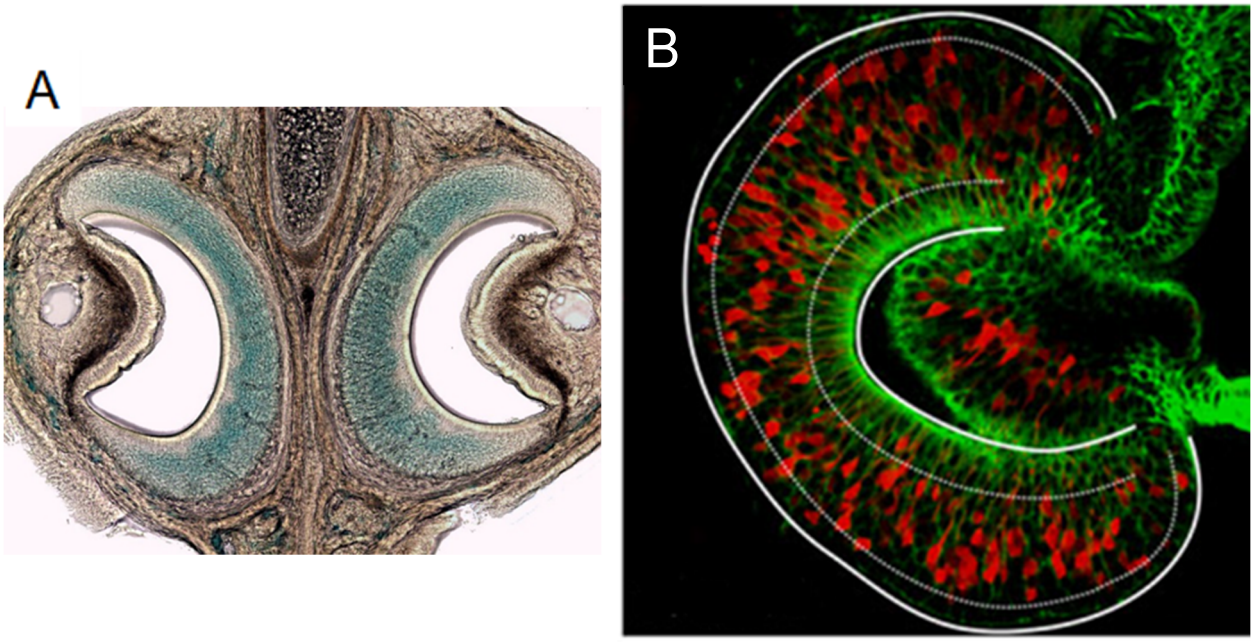

Figure 3. Histological organization of the VNO. (A) Coronal section of the VNO from mice with the vomeronasal sensory epithelium in blue, adapted from **(Ibarra-Soria et al., 2014)**. (B) Coronal section of the VNO from *Xenopus Laevis*, where we can see the vomeronasal sensory epithelium, with the supporting cells and epithelial cells labelled in green with an antibody against cytokeratin II, and vomeronasal sensory neurons filled with biocytin revealed with Alexa 546 conjugated streptavidin. Adapted from Dittrich et al., 2014.

1.2. Supporting cells of the olfactory epithelium

1.2.1. Biophysical properties

The biophysical properties of supporting cells were previously analyzed in acute olfactory epithelium slices from newborn mice. It was determined that they have an average cell capacitance of 18.6 ± 0.5 pF and a membrane resistance of 160 ± 11 MΩ.The resting membrane potential ranges between -30 mV and -50 mV (Vogalis et al., 2005a).

1.2.1.1. Gap junctions and cell syncytium

Supporting cells of adult rats and mice have been shown to express connexin 43 and connexin 45 (Rash et al., 2005). Connexins assemble in hexomers forming connexons, or hemichannels. Connexons can be homomeric or heteromeric, depending if they are formed by a single type of connexin or a combination of different ones respectively. Gap-junctions are formed when two membranes expressing connexons enter into contact usually through the aid of adhesion proteins like cadherins (Wei et al., 2004). Depending on the kind of connexins, gap-junction have different properties, such as ion conductance, permeability, voltage sensitivity and regulation by second messengers (Harris, 2001).

Gap junctions allow the diffusion of cytoplasmic solutes between neighboring cells along concentration gradients. They are permeable to molecules up to 1 kDa, but the rate of diffusion across gap junctions depends both on the size of the solute and on the connexin isoforms composing the gap-junction (Weber et al., 2004). Not only do gap junctions allow the diffusion of solutes across the concentration gradient, they are also essential for coordinating the activity of certain cells, be it through the spread of an electrical current, as in electrical synapses (Connors and Long, 2004), or the diffusion of second messengers, as in calcium waves (Weissman et al., 2004).

Although dye-coupling studies failed to observe the diffusion of Lucifer Yellow or Alexa 488 between neighboring supporting cells, the use of 18β-glycyrrhetinic acid, a gap junction blocker (Davidson and Baumgarten, 1988)., drastically decreased the leak current measured in supporting cells using whole-cell patch clamp recordings, indicating that these cells are electrically coupled through gap junctions (Figure 4A-B; Vogalis et al., 2005b). This electrical coupling means that supporting cells form a syncytium. Depending on the composition of these gap junctions, this might also allow the diffusion of the second messengers responsible for the calcium waves observed in supporting cells (Hegg et al., 2009).

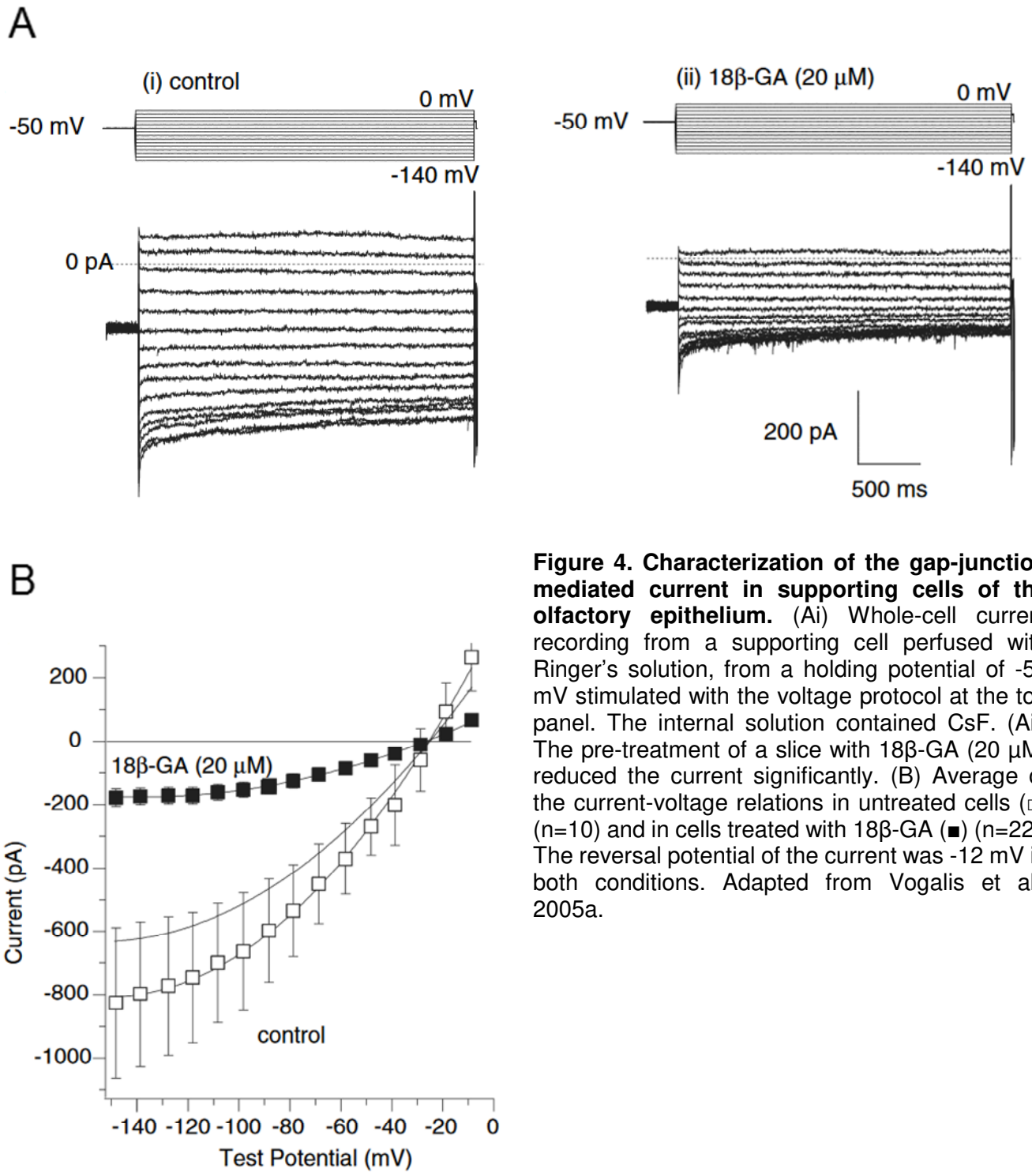

Figure 4. Characterization of the gap-junction mediated current in supporting cells of the olfactory epithelium. (Ai) Whole-cell current recording from a supporting cell perfused with Ringer's solution, from a holding potential of -50 mV stimulated with the voltage protocol at the top panel. The internal solution contained CsF. (Aii) The pre-treatment of a slice with 18β-GA (20 µM) reduced the current significantly. (B) Average of the current-voltage relations in untreated cells (□) (n=10) and in cells treated with 18β-GA (■) (n=22). The reversal potential of the current was -12 mV in both conditions. Adapted from Vogalis et al., 2005a.

1.2.1.2. Voltage-gated sodium channels

Supporting cells of the olfactory epithelium express voltage-gated sodium channels. In whole cell recordings from mouse supporting cells, depolarizing voltage steps from a holding potential of -109 mV elicited fast-inactivating inward current. Replacement of external sodium by N-methyl-D-glucamine (NMDG), a bulk cation not permeant through known voltage-gated sodium channels, ablated the current, showing that this current is mediated by sodium ions (Figure 5A; Vogalis et al., 2005a).

The application of 1 µM tetrodotoxin (TTX) only decreased the amplitude of the inward current by 48% indicating that supporting cells of the olfactory epithelium express both TTX sensitive and insensitive voltage-gated sodium channels (Figure 5B).

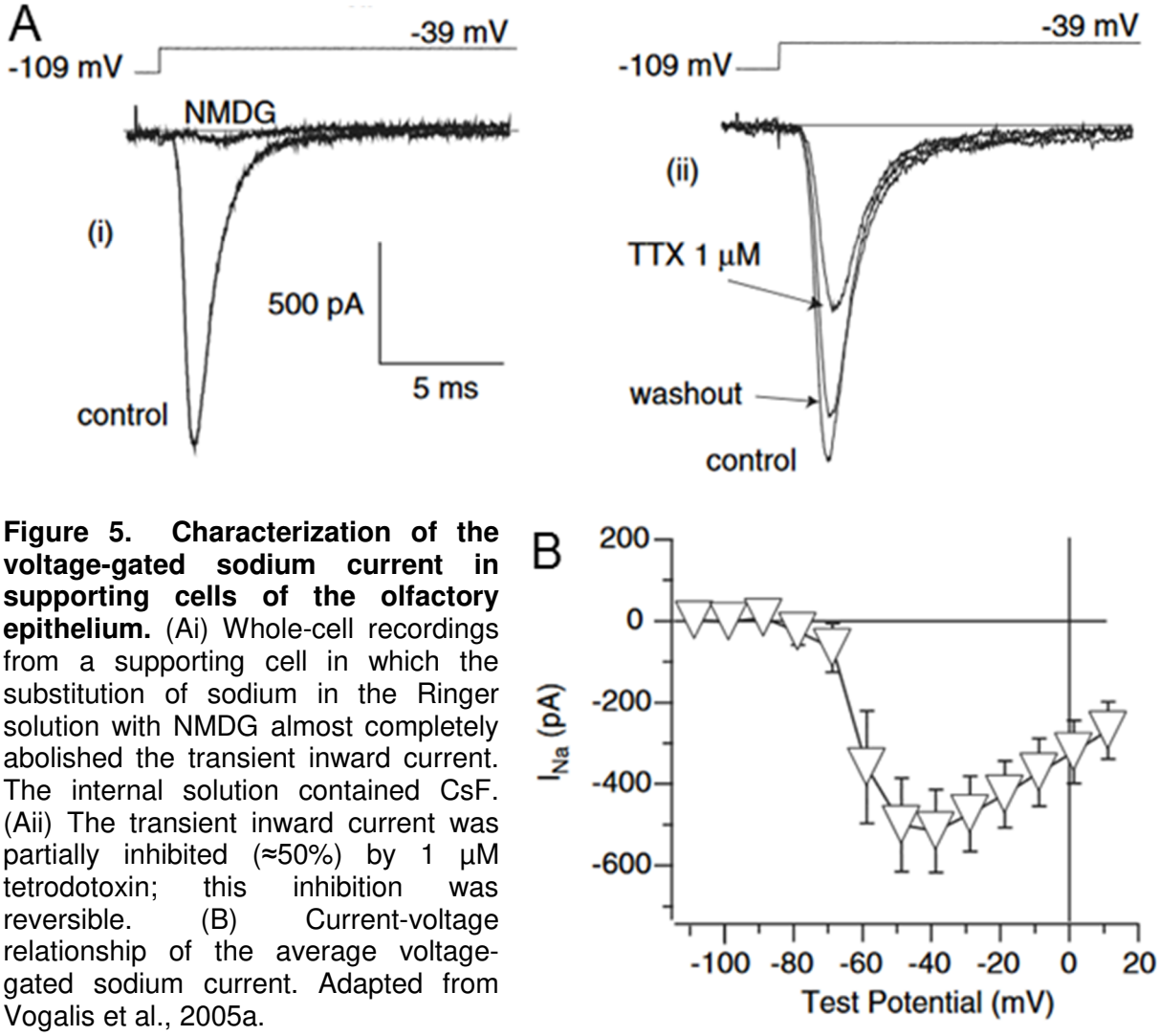

Figure 5. Characterization of the voltage-gated sodium current in supporting cells of the olfactory epithelium. (Ai) Whole-cell recordings from a supporting cell in which the substitution of sodium in the Ringer solution with NMDG almost completely abolished the transient inward current. The internal solution contained CsF. (Aii) The transient inward current was partially inhibited (≈50%) by 1 µM tetrodotoxin; this inhibition was reversible. (B) Current-voltage relationship of the average voltage-gated sodium current. Adapted from Vogalis et al., 2005a.

1.2.1.3. Voltage-gated potassium channels

Using the whole-cell patch clamp technique, it was determined that supporting cells are capable of generating a voltage-gated outward rectifying potassium current activated at voltages more positive than -40 mV. Large conductance potassium (BK) channels sensitive to tetraethylammonium (TEA) and charybdotoxin mediated more than 70% of this outward current (Figure 6A). From cell-attached recordings it was determined that these BK channels can be found in the apical surface of the supporting cells, but no further studies have been conducted on the identity or compartmentalization of these channels (Figure 6B; Vogalis et al., 2005a).

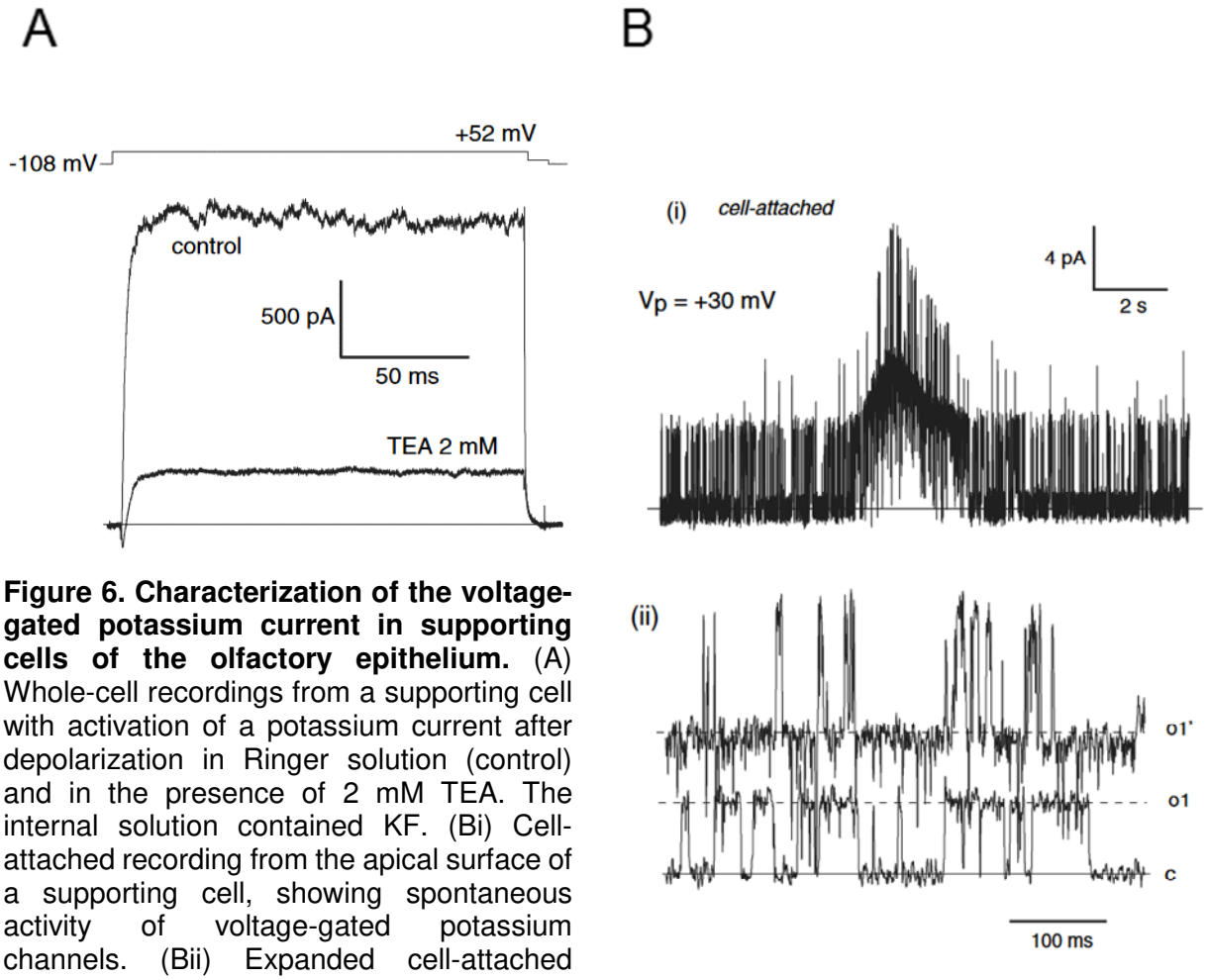

Figure 6. Characterization of the voltage-gated potassium current in supporting cells of the olfactory epithelium. (A) Whole-cell recordings from a supporting cell with activation of a potassium current after depolarization in Ringer solution (control) and in the presence of 2 mM TEA. The internal solution contained KF. (Bi) Cell-attached recording from the apical surface of a supporting cell, showing spontaneous activity of voltage-gated potassium channels. (Bii) Expanded cell-attached recordings showing superimposed unitary currents taken before (o1) and during the peak of the activity burst (o1'). Adapted from Vogalis et al., 2005a.

1.2.1.4. Action potentials

With the expression of voltage-gated sodium and potassium channels, supporting cells of the olfactory epithelium possess the molecular machinery for the generation of action potentials. By using the current clamp technique, it was shown that, at a holding potential of -98 mV, supporting cells are capable of forming a single action potential (Figure 7A). However, it was also shown that the resting membrane potential of supporting cells in Ringer's solution is of -30/-50 mV (Vogalis et al., 2005a), and that it was impossible to induce the action potentials from that holding voltage (Figure 7B).

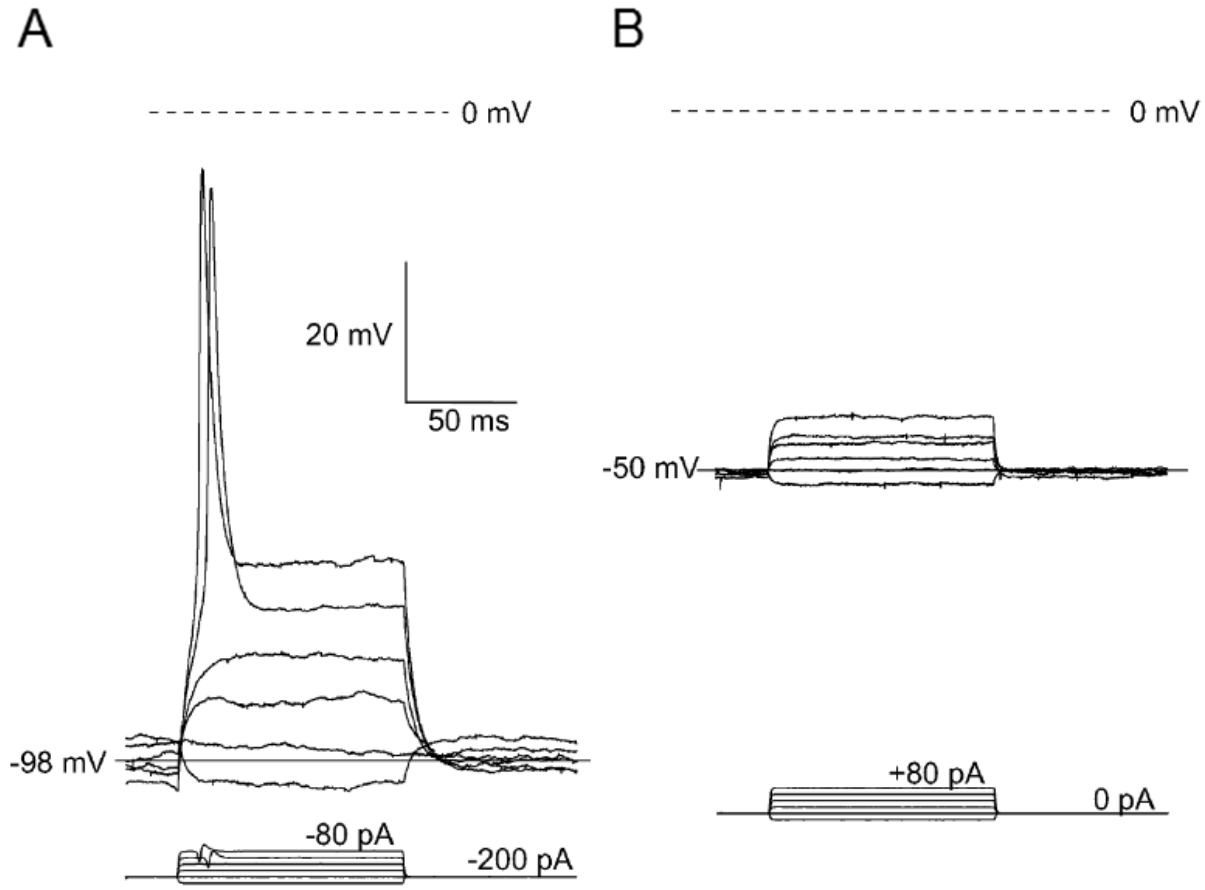

Figure 7. Current-clamp recordings in supporting cells of the olfactory epithelium. (A) Single action potential in a supporting cell in current clamp after depolarization to -60 mV, from a holding potential of about -98 mV. (B) In the absence of a holding current, the supporting cell depolarized to -50 mV and was not excitable. Adapted from Vogalis et al., 2005a.

This differences from the holding potential of -98 mV and the resting potential of -30/-50 mV can be explained by the properties of voltage-gated sodium channels. At a resting membrane potential of -50 mV, the majority of voltage-gated sodium channels are going to be in their inactivated state, a state in which the channels cannot be activated through depolarization. In

contrast, if a holding potential of -98 mV is induced using the current clamp technique, enough voltage-gated sodium channels are going to be in their resting state, in which the channels are also closed but a depolarization will be able to open the channels, allowing for an influx of sodium ions (Hille, 2001). This influx of sodium ions will further depolarize the membrane, which in return triggers the opening of the voltage-gated potassium channels, resulting in the action potentials shown in Figure 7.

Although there was no action potential generated from the resting potential of -50 mV, it is important to point out that this measurement was made in Ringer's solution, which is not necessarily an accurate representation of the ionic conditions that supporting cells are exposed to in physiological (or pathological) conditions. While the cell soma is immersed in cerebrospinal fluid (Nagra et al., 2006), which is similar in ionic composition to a Ringer's solution, the apical part of the cell is exposed to the olfactory mucus, with a very different ionic composition (Reuter et al., 1998). Table I summarizes the ionic conditions to which supporting cells of the olfactory epithelium are exposed to, and the equilibrium potentials for various ions calculated with the Nernst equation. It should be noted that the concentrations of chloride ions are rather similar in the olfactory mucus (55 mM) and inside the supporting cells (38 mM) producing an equilibrium potential for Cl^- of -14.5 mV. Taking into account that the resting membrane potential of the supporting cells has been estimated to be in the range between -50 mV and -30 mV (Vogalis et al., 2005a) the calculated electrochemical driving force for Cl^- ranges between -35.5 and -15.5 mV. Thus, the opening of a chloride conductance at the surface of the epithelium causes an efflux of chloride.

Ion	$[Ion]_{in}$ (mM)	[Ion] Olfactory mucus (mM)	[Ion] Cerebrospinal fluid (mM)	E_{Nernst} Surface of olfactory epithelium (mV)	E_{Nernst} Soma of supporting cells (mV)
Sodium	28	55	151	18	45
Potassium	147	69	3	-20.2	-104
Chloride	38	55	133	-14.5	-38

Table I Comparison of resting electrochemical gradients at the apical end and around the soma of supporting cells. The ionic concentrations in rat olfactory mucus and inside the supporting cells were measured by energy-dispersive X-ray microanalysis (Reuter et al., 1998). The data about the cerebrospinal fluid was obtained by Brown et al., 2004. The Nernst potential was calculated using the equation: $\boldsymbol{E_{Nernst} = \frac{RT}{zF} \ln \frac{[Ion]_{out}}{[Ion]_{in}}}$ where R is the gas constant, T is absolute temperature, z is the ion valence, and F is the Faraday constant.

1.2.2. Calcium signaling

Calcium signaling in glial cells mainly occurs in two forms: calcium waves, in which elevations in calcium concentration propagate between cells, and calcium oscillations, repetitive elevations in intracellular calcium confined to a single cell (Scemes and Giaume, 2006). Both spontaneous calcium waves and evoked calcium oscillations have been observed in the supporting cells of the olfactory epithelium (Hegg et al., 2009).

Supporting cells of the mouse olfactory epithelium express $P2Y_2$ receptors and the M_3 muscarinic acetylcholine receptors (M_3AchR) (Figure 8). The expression of M_1 muscarinic acetylcholine receptors (M_1AchR) is confined to the supporting cells located laterally in the olfactory epithelium (Figure 9; Ogura et al., 2011).

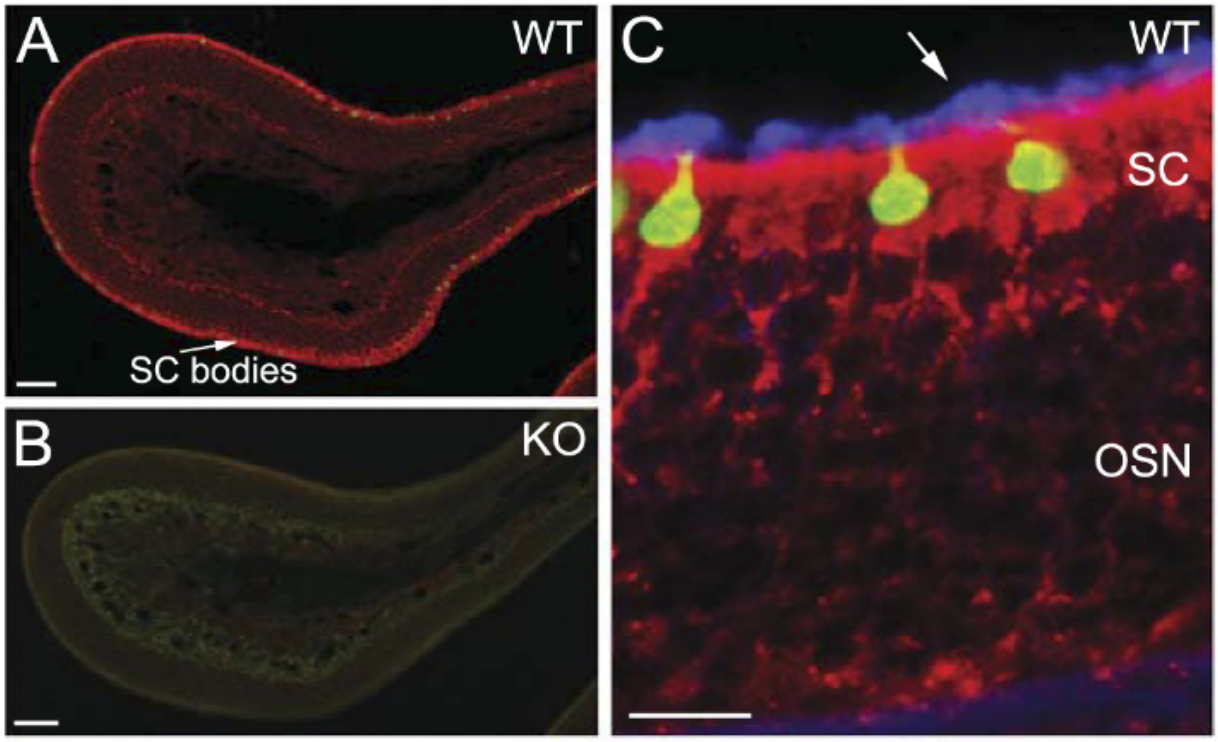

Figure 8. Strong immunoreactivity of muscarinic acetylcholine M_3 receptor in supporting cells of the olfactory epithelium. (A) Low-magnification confocal image from an olfactory epithelium section from a mouse expressing ChAT(BAC)-eGFP (green), a marker for cholinergic cells, showing strong immunoreactivity for M_3 receptor (red) in the cell bodies of supporting cells (SC). (B) Confocal image from an olfactory epithelium section of a M_3 receptor knockout mouse, showing absence of M_3 immunoreactivity. Sections in A and B were processed for immunoreaction and imaging under the same conditions. (C) High-magnification image showing strong immunoreactivity for M_3 receptor (red) in the supporting cells of the olfactory epithelium of a ChAT(BAC)-eGFP mouse. The cilia of olfactory sensory neurons are marked by anti-acetylated tubulin (blue, indicated with an arrow). Scale: A and B 100 µm, C 20 µm. Adapted from Ogura et al., 2011.

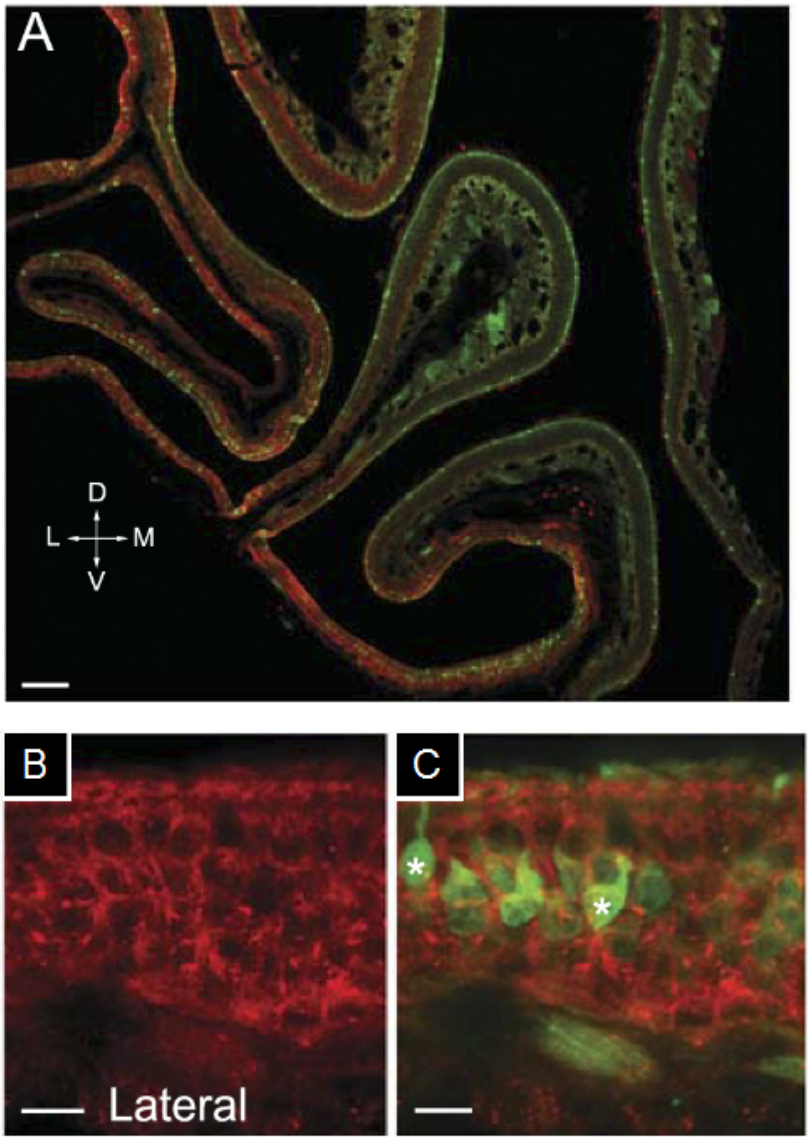

Figure 9. Immunoreactivity of muscarinic acetylcholine receptor type 1, M_1AchR, in the olfactory epithelium. (A) Low-magnification confocal image from a coronal section of the olfactory epithelium from a TRPM5-GFP mouse, a marker of microvillar cells and a subset of olfactory sensory neurons. M_1 receptor immunoreactivity (red) is primarily present in the lateral region. (B) Confocal image from a ventrolateral region showing strong M_1 immunoreactivity (red) in supporting cells. (C) A GFP image overlaid onto B shows that TRPM5-GFP signal and M_1 receptor immunoreactivity do not co-localize. Scale: A 200 µm, B and C 20 µm. Adapted from Ogura et al., 2011.

The receptors $P2Y_2$, M_3AchR and M_1AchR are coupled to the Gq protein, which activates phospholipase C, leading to the production of the second messengers inositol-3-phosphate (IP3) and diacyl glycerol (Hegg et al., 2009).

Acetylcholine is produced in the olfactory epithelium by the microvillar cells and the trigeminal nerve (Getchell et al., 1988; Ogura et al., 2011). The release of acetylcholine is thought to arise as a response to xenobiotic detection (Lucero, 2013).

ATP is an agonist of $P2Y_2$ receptors and it is released in several tissues under a variety of conditions including mechanical stimulation, hypoxia, acidosis, osmotic shock and fluid sheer stress (Bodin and Burnstock, 2001).

In the olfactory epithelium, there is also a constitutive ATP release that involves a combination of vesicular release, ABC transporters and pannexin hemichannels, although the

cells of origin are still unknown. The release of ATP in the olfactory epithelium is also inducible by purinergic signaling through the activation of P2X receptors (Hayoz et al., 2012), creating a positive feedback mechanism, since these receptors are also activated by the binding of ATP. The ATP released through the activation of P2X receptors most probably originates from olfactory sensory neurons, since only olfactory sensory neurons express P2X receptors in the olfactory epithelium, whereas both supporting cells and olfactory sensory neurons express P2Y receptors (Figure 10; Hegg et al., 2003).

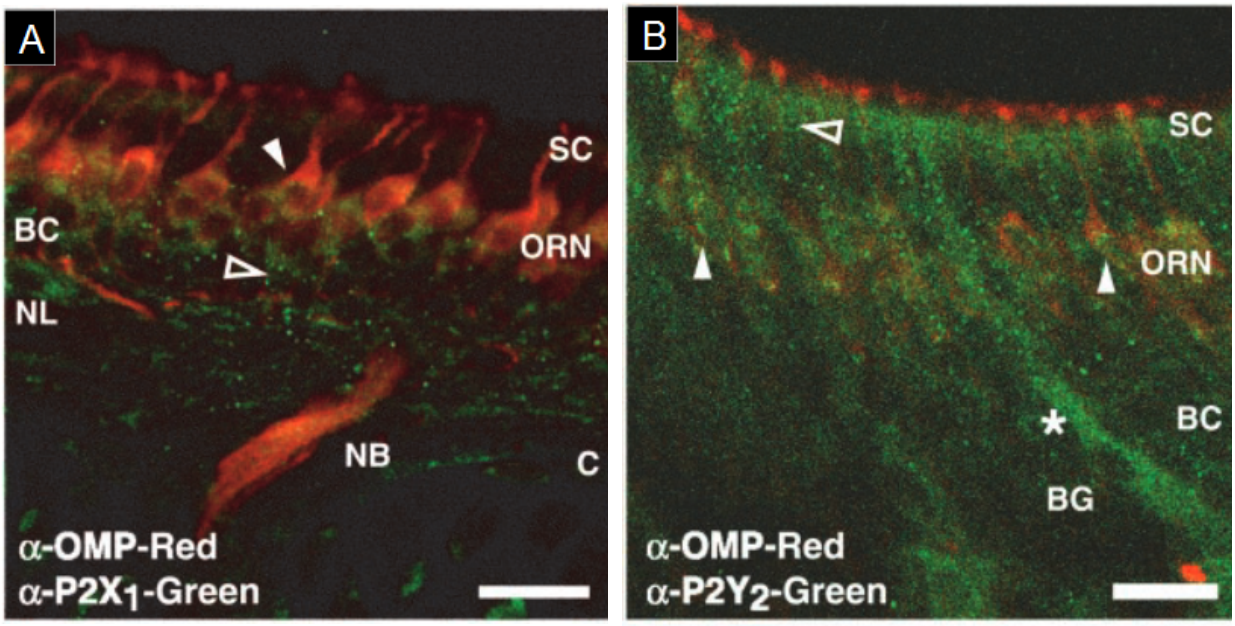

Figure 10. Expression of purinergic receptors in the olfactory epithelium. (A) Mouse olfactory epithelium showing punctuate $P2X_1$ labelling (green) in OMP labeled (red) olfactory sensory neurons. (B) Expression of $P2Y_2$ (green) in the olfactory epithelium, with expression in supporting cells (hollow arrows), olfactory sensory neurons (filled arrows) labelled with an antibody for OMP (red), and Bowman's gland (*). Scale bars 20 µm. Abbreviations: BC, basal cells; BG, Bowman's Gland; C, cribriform plate; NB, nerve bundle; NL, nerve layer; OMP, olfactory marker protein; ORN, olfactory sensory neurons; SC, supporting cells. Adapted from Hegg et al., 2003.

Hegg et al. (2009) showed that supporting cells of the olfactory epithelium of mice are responsive to UTP even in the absence of extracellular calcium, but not when intracellular stores of calcium are depleted, indicating that calcium transients are caused by release from intracellular stores. Furthermore, the inhibition of the phospholipase C attenuated the intracellular calcium increase induced by UTP, as did the inhibition of IP_3 receptors and ryanodine receptors (Hegg et al., 2009). These results indicated that the supporting cell calcium response to ATP is not only dependent on intracellular stores, but also that the release of calcium from those stores is mediated by IP_3 and ryanodine receptors through the activation of the phospholipase C pathway (Figure 11; Hegg et al., 2009).

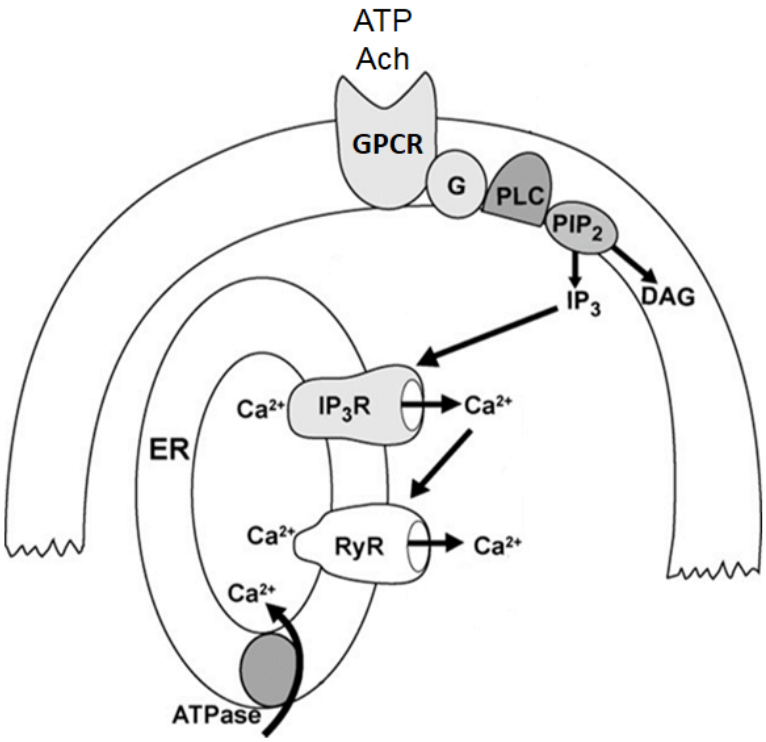

Figure 11. Schematic representation of the signaling pathways leading to calcium release from intracellular stores in supporting cells of the olfactory epithelium. Activation of G-coupled proteins (GPCR) leads to the activation of phospholipase C (PLC) and production of diacylglycerol (DAG) and inositol-3-phosphate (IP_3), which binds to IP_3 receptors with subsequent release of calcium from intracellular stores in the endoplasmic reticulum (ER). The increase in cytosolic calcium leads to the activation of ryanodine receptors (RyRs) that release more calcium from the ER. Abbreviations: Ach, acetylcholine; ATPase, calcium ATPase; G, G-protein; PIP_2, phosphoinositol 2-phosphate. Adapted from Hegg et al., 2009.

1.2.3. Expression of the calcium-activated chloride channel TMEM16A in supporting cells

Supporting cells of the olfactory epithelium express the calcium-activated chloride channel TMEM16A, whereas they do not express TMEM16B which is present in olfactory sensory neurons (Dauner et al., 2012; Maurya and Menini, 2014). TMEM16A and 16B belong to the TMEM16 protein family, which has 10 members in total, labeled with letters from A to K. In particular, TMEM16A and 16B are known to mediate voltage-regulated calcium activated anion currents (Pedemonte and Galietta, 2014). There are multiple isoforms of TMEM16A (Ferrera et al., 2009) and 16B (Ponissery Saidu et al., 2013) generated by alternative splicing.

TMEM16A is expressed in many tissues, including cells of salivary and pancreatic glands, airway epithelial cells, airway and vascular smooth muscle cells, interstitial cells of Cajal (Huang et al., 2009), sensory neurons in the dorsal root ganglia (Liu et al., 2010), supporting cells of the olfactory epithelium (Maurya and Menini, 2014), and vomeronasal sensory neurons (Dibattista et al., 2012).

This channel is known to play an important role in many physiological functions including epithelial secretion, neuronal excitability and smooth muscle contraction. TMEM16A has also been implicated in many diseases such as cancer (Wang et al., 2017), hypertension (Wang et al., 2015), gastrointestinal motility disorders (Mazzone et al., 2011), and cystic fibrosis (Benedetto et al., 2017; Sondo et al., 2014).

In the olfactory epithelium, supporting cells expressing TMEM16A are mainly located laterally, in the transition zone between the olfactory epithelium and the respiratory epithelium (Figure 12; Maurya and Menini, 2014).

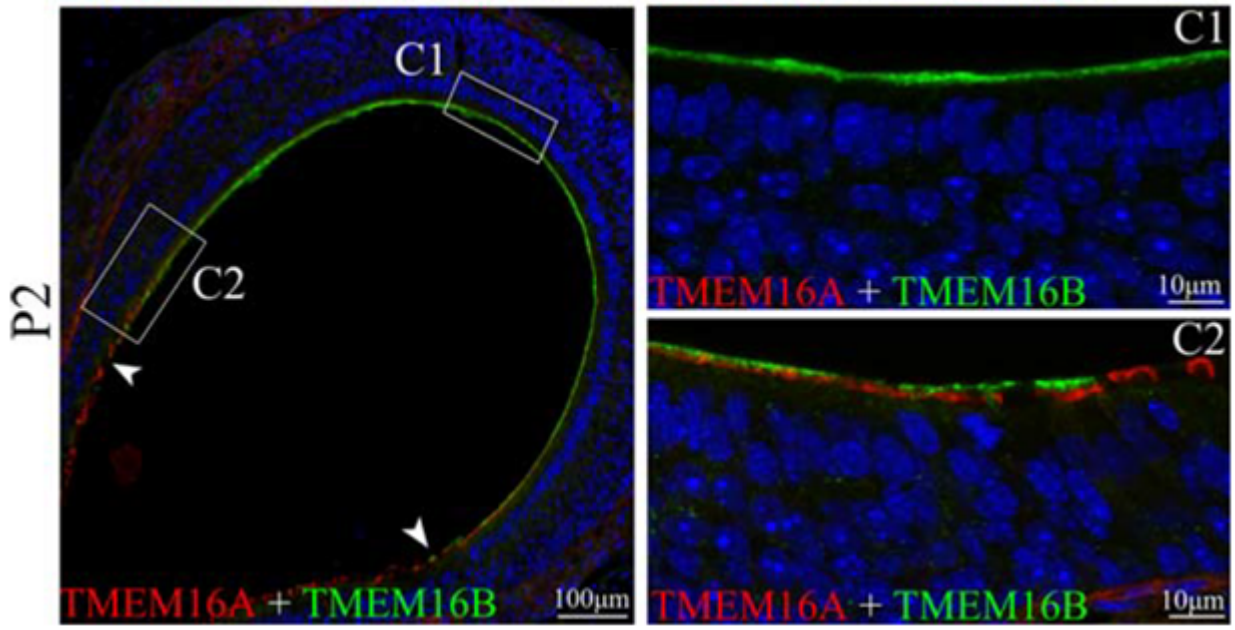

Figure 12. TMEM16A expression in supporting cells of the olfactory epithelium. (A) Confocal image of a coronal slice of the nasal cavity, immunoreactivity for TMEM16A (red) and TMEM16B (green) in the olfactory epithelium. TMEM16B is a protein expressed on the cilia of olfactory sensory neurons at the apical surface of the olfactory epithelium. (C1) Magnification of the dorsal region of the olfactory epithelium seen in (A), without TMEM16A immunoreactivity. (C2) Magnification of the lateral region of the olfactory epithelium with TMEM16A expression at the apical surface. Adapted from Maurya and Menini, 2014.

At embryonic day 12.5, the expression of TMEM16A can already be found along the whole apical surface of the developing olfactory epithelium, but at embryonic day 16.5 its expression in the olfactory epithelium becomes restricted mainly to the transition zone between the olfactory epithelium and the respiratory epithelium, similarly to what is observed postnatally (Maurya and Menini, 2014). The specific expression of TMEM16A in the microvilli of supporting cells of the olfactory epithelium becomes more evident analyzing the tissue during the early embryonic stages because the apical surface of the supporting cells is easily distinguishable from that of olfactory sensory neurons. Indeed, the number of mature olfactory sensory neurons and the length of their cilia, which will eventually cover the microvilli of the supporting cells, increase during development (Figure 13).

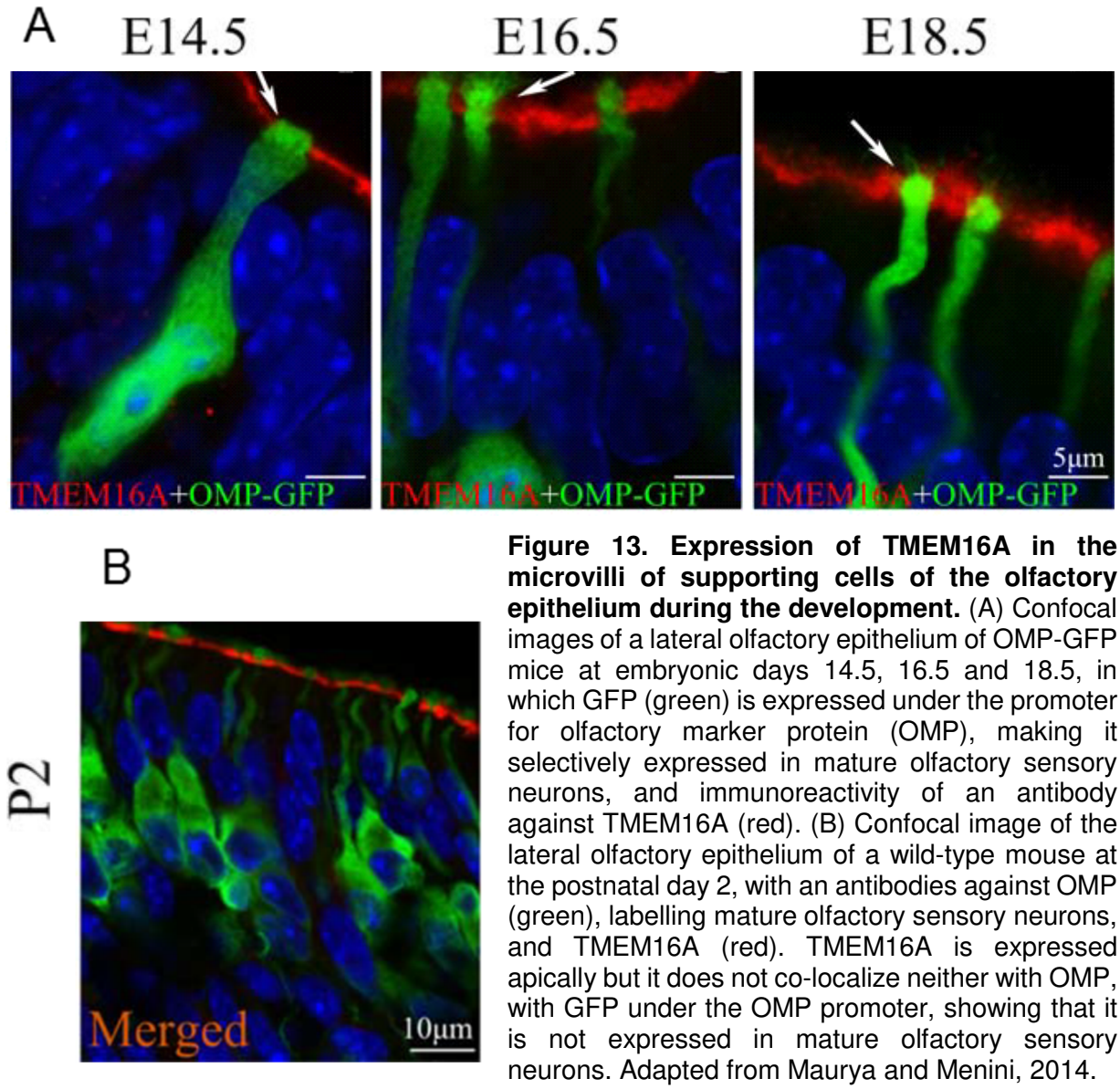

Figure 13. Expression of TMEM16A in the microvilli of supporting cells of the olfactory epithelium during the development. (A) Confocal images of a lateral olfactory epithelium of OMP-GFP mice at embryonic days 14.5, 16.5 and 18.5, in which GFP (green) is expressed under the promoter for olfactory marker protein (OMP), making it selectively expressed in mature olfactory sensory neurons, and immunoreactivity of an antibody against TMEM16A (red). (B) Confocal image of the lateral olfactory epithelium of a wild-type mouse at the postnatal day 2, with an antibodies against OMP (green), labelling mature olfactory sensory neurons, and TMEM16A (red). TMEM16A is expressed apically but it does not co-localize neither with OMP, with GFP under the OMP promoter, showing that it is not expressed in mature olfactory sensory neurons. Adapted from Maurya and Menini, 2014.

By immunostaining of both TMEM16A and ezrin, a marker of the microvilli of supporting cells, it was confirmed that TMEM16A is expressed in the apical surface of the supporting cells, but more specifically, it is expressed at the proximal base of the microvilli (Figure 14).

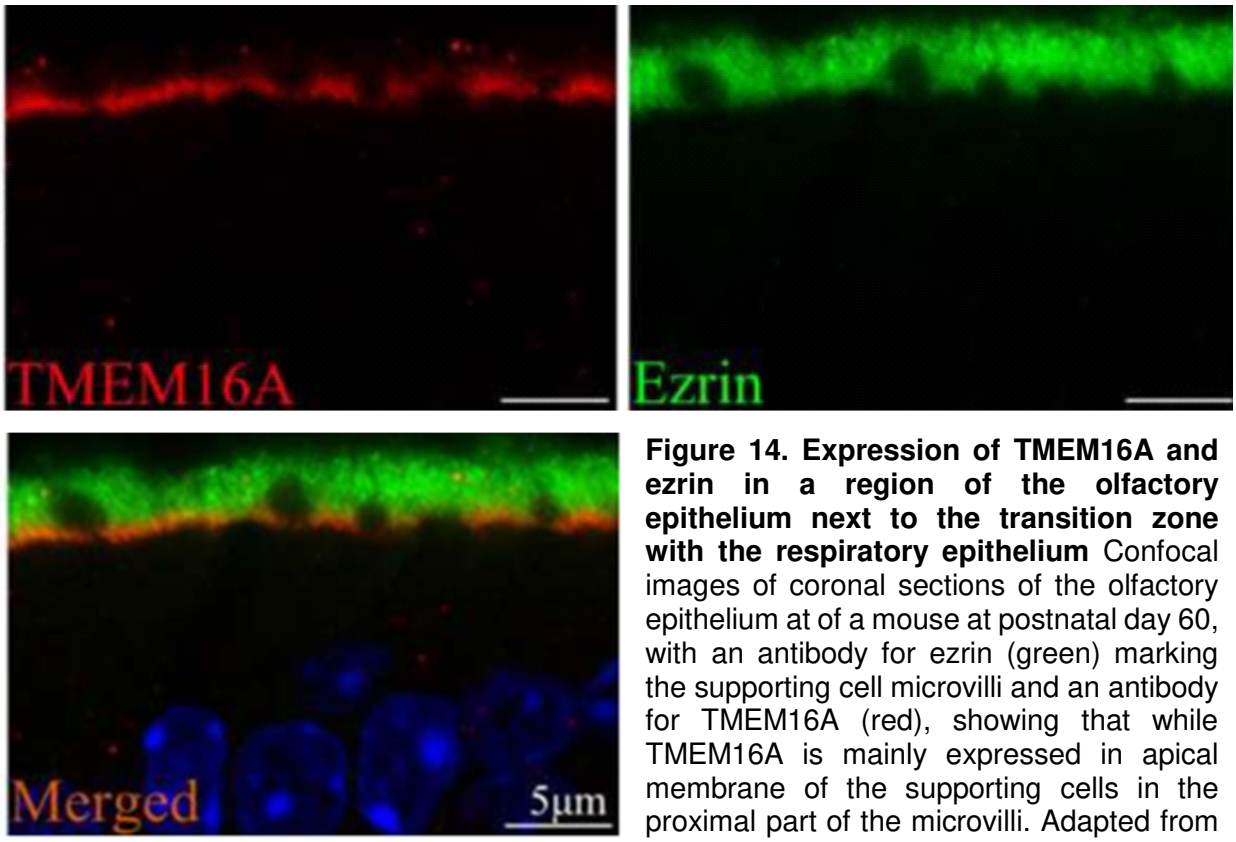

Figure 14. Expression of TMEM16A and ezrin in a region of the olfactory epithelium next to the transition zone with the respiratory epithelium Confocal images of coronal sections of the olfactory epithelium at of a mouse at postnatal day 60, with an antibody for ezrin (green) marking the supporting cell microvilli and an antibody for TMEM16A (red), showing that while TMEM16A is mainly expressed in apical membrane of the supporting cells in the proximal part of the microvilli. Adapted from Maurya and Menini, 2014.

1.2.4. Physiological functions

1.2.4.1. Xenobiotic metabolism

Supporting cells express several cytochrome P450 enzymes (CYPs), similarly to hepatic cells (Guengerich, 1999). Therefore, they are capable of metabolizing a variety of small and large molecules, both endogenous – such as hormones, lipids and vitamins - and exogenous - such as pharmaceutical drugs, odorants, toxicants and toxins, also called xenobiotics (Rendic and Di Carlo, 1997).

Depending on the properties of the molecules entering the nasal cavity, the activity of the CYPs expressed in the supporting cells can have both an adverse effect and a protective role. For example, the damage caused by the toxicity of acetaminophen was mitigated in mice knock-out mice for CYP2G1, a CYP specifically expressed in supporting cells. The absence of this protein lead to a reduced lesioning of the lateral nasal gland caused by acetaminophen, and, paradoxically, CYP2G1 is not even expressed in the lateral nasal gland. Although the precise reason for this acquired resistance to acetaminophen toxicity by CYP2G1 knock-out mice models

is unknown, it has been proposed that CYP2G1 is transforming steroid hormones or other molecules in the olfactory epithelium and the products of the reaction are diffusing to the lateral nasal gland, affecting gene expression locally (Zhuo et al., 2004).

1.2.4.2. Odorant transformation

Supporting cells seem to be involved also in odorant transformation. For example, the electro-olfactogram (EOG) response amplitude to quinoline and coumarin is increased by application of 1-Aminobenzotriazole (ABT) that inhibits the CYPs, which are mainly expressed in the supporting cells and in the duct cells of the Bowman's gland. This is the results of a bigger response of olfactory sensory neurons to quinolone and coumarin than to their derivatives resulting from CYP transformation (Thiebaud et al., 2013). Similar results were obtained investigating the response of the odorant receptor MOR161-2 to acetophenone. CYP1a2 was able to convert acetophenone in methyl salicylate, a more potent agonist of MOR161-2. Moreover blocking of CYPs with ABT or the removal of olfactory mucus decrease the number of MOR161-2-expressing OSNs that respond to acetophenone (Asakawa et al., 2017). It has not been tested yet if CYP proteins are able to modulate the olfactory response to other odorants, but, given the low selectivity of CYPs, it is probable that there are other odorant molecules that can be transformed by these proteins possibly generating odorants with different properties.

Odor transformation could be also mediated by other enzymatic activities. Indeed, Nagashima and Touhara (2010) found that mouse olfactory mucus a carboxyl esterase activity able to convert aliphatic and aromatic aldehyde and ester to alcohol. Pharmacological blockage of carboxyl esterase with bis(p-nitrophenyl)phosphate (BNNP) changes the pattern of glomeruli activation in olfactory bulb indicating upon stimulation with acetyl isoeugenol indicating that odor transformation occurs also in vivo (Nagashima and Touhara, 2010).

1.2.4.3. Phagocytosis of dead olfactory sensory neurons

Olfactory sensory neurons are continuously replaced in the olfactory epithelium by the differentiation of GBCs (Weiler and Farbman, 1997), and therefore old olfactory neurons and cellular debris need to be disposed of. Both macrophages and supporting cells have shown the ability to phagocyte dead olfactory sensory neurons after bulbectomy (Suzuki et al., 1996).

1.2.4.4. Potassium spatial buffering

Ever since it was shown that action potentials are coupled to an efflux of potassium, scientists have been trying to determine the mechanisms for removal of excess potassium between neighboring neurons (Coles and Orkand, 1983; Hertz, 1965; Hodgkin and Huxley, 1952; Orkand et al., 1966). An effective electrical insulation is needed in order to prevent interference in neuronal signaling. The buildup of extracellular potassium in the central nervous system has been linked with pathologies like epilepsy and with cortical spreading depression, which is associated with migraine (Bellot-Saez et al., 2017; David et al., 2009; Scholl et al., 2009; Somjen, 2002).

Mice knock-outs for aquaporin 4 have been shown to decrease potassium uptake in astrocytes of the central nervous system. The proposed mechanism is that potassium uptake is coupled to an increase in osmotic pressure, effectively requiring water uptake and cell volume increase in order for the cell to reach maximum buffering activity (Strohschein et al., 2011). It is possible that a similar mechanism occurs also in supporting cells, as the knockout for aquaporin 4 leads to a decrease in olfactory function (Lu et al., 2008).

It is still unknown if the BK channels identified in supporting cells are involved in this mechanism of potassium spatial buffering (Vogalis et al., 2005a).

1.2.4.5. Mucus ionic regulation

Supporting cells have been shown to express TMEM16A, a calcium-activated chloride channel (Maurya and Menini, 2014) and the epithelial sodium channel (ENaC) (Menco et al., 1998).

While studies about mucus ionic regulation by supporting cells are lacking, such studies have been conducted using airway epithelia which, like supporting cells, express both TMEM16A and ENaC. By using an Ussing chamber on the airway epithelium taken from wild-type and TMEM16A knock-out mice, it was possible to determine that the absence of TMEM16A leads to a reduction of the transepithelial current induced by UTP, which suggests that the opening of TMEM16A channels can be triggered by the activation of P2Y receptors in this tissue (Rock et al., 2009). Unfortunately, these experiments could only be performed in neonatal mice because the knock-out of TMEM16A is fatal in mice, as 90% of knock-out newborn mice die before day 9. The explanation proposed for this early death is a combination of tracheal collapse, due to malformed cartilage tracheal rings, and mucus-mediated adhesion of opposing tracheal walls, which eventually results in asphyxia (Rock et al., 2009).

TMEM16A also interacts with mucus production due to its modulatory effect on mucin release. Mucin is a main component of mucus and has the property of forming gels, in fact the concentration of mucin in the mucus determines its viscosity. TMEM16A modulates the release of mucin in normal human bronchial epithelial cells previously treated with interleukin-3. ATP stimulation of these cells is able to induce the release of mucin by these cells, but the use of TMEM16A blockers ablates this effect (Zhang et al., 2015). We can speculate that the expression of TMEM16A may have a similar role in other tissues, including the olfactory epithelium.

1.3. Supporting cells of the vomeronasal organ

1.3.1. Biophysical Properties

The biophysical properties of supporting cells of the mouse VNO have been extensively investigated by Ghiaroni et al. (2003). Isolated VNO supporting cells have a depolarized resting membrane potential of about -29 mV and a membrane resistance of 1.7 ± 0.2 GΩ (Ghiaroni et al., 2003). The cell capacitance was 9.2 ± 0.6 pF, lower than the capacitance value of 18.6 ± 0.5 pF of supporting cells of the olfactory epithelium (Vogalis et al., 2005a), but higher than the value 5.1 ± 0.4 pF in vomeronasal neurons (Ghiaroni et al., 2003). These cells express both voltage-gated sodium and potassium channels.

Voltage-gated potassium currents of the VNO supporting cells, in contrast to the voltage-gated potassium currents of the neighboring vomeronasal neurons, are almost completely abolished in the presence of TEA at a concentration of 10 mM. The IC_{50} for blockage by TEA of these currents is 0.35 mM in supporting cells and 3.39 mM in neurons. This current is also almost completely unaffected by the common voltage-gated potassium channel blocker 4-aminopyridine (4-AP) at a concentration of 2 mM (Figure 15; Ghiaroni et al., 2003).

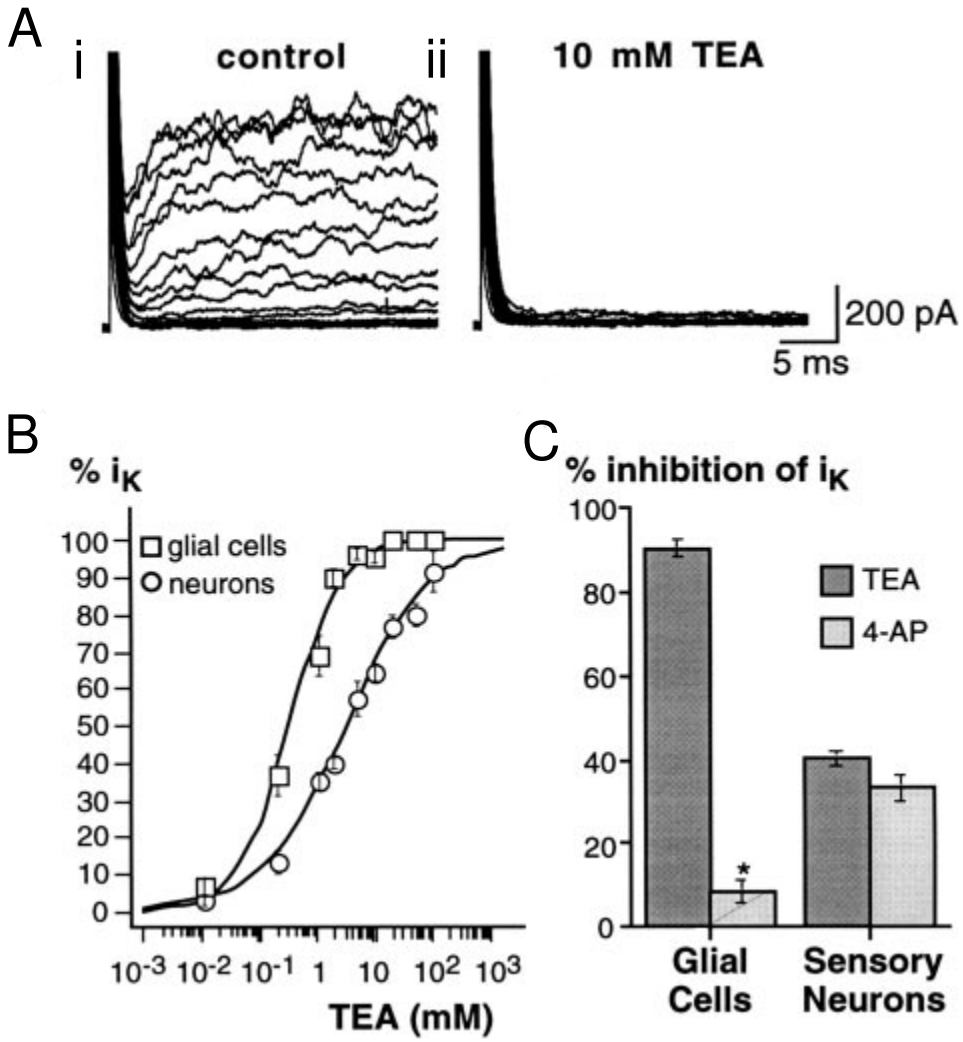

Figure 15. Characterization of voltage-gated potassium currents in supporting cells of the VNO. Whole-cell patch clamp recordings from isolated supporting cells were obtained with a series of depolarizing pulses between -74 mV and +106 mV, with 10 mV increments, from a holding potential of -84 mV. (Ai) Recording in Tyrode (control) external solution. (Aii) Same cell in the presence of TEA, which ablated the outward current. (B) Dose-response curves for the effect of TEA on supporting cells (□) and vomeronasal sensory neurons (○). (C) Comparison of the effect of 2 mM TEA and 2 mM 4-AP on the outward potassium current in supporting cells and in vomeronasal sensory neurons. Abbreviations: 4-AP, 4-aminopyridine; TEA, tetraethylammonium. Adapted from Ghiaroni et al., 2003.

The amplitude of the voltage-gated sodium currents depended on the holding potential preceding the step depolarization, with currents observable from holding potentials lower than - 85 mV (Figure 16). This suggests that a high proportion of sodium channels are inactivated at more positive holding potentials.

These voltage-gated sodium currents were almost completely abolished in the presence of 10 µM of TTX, with an IC_{50} for this drug of 0.48 µM.

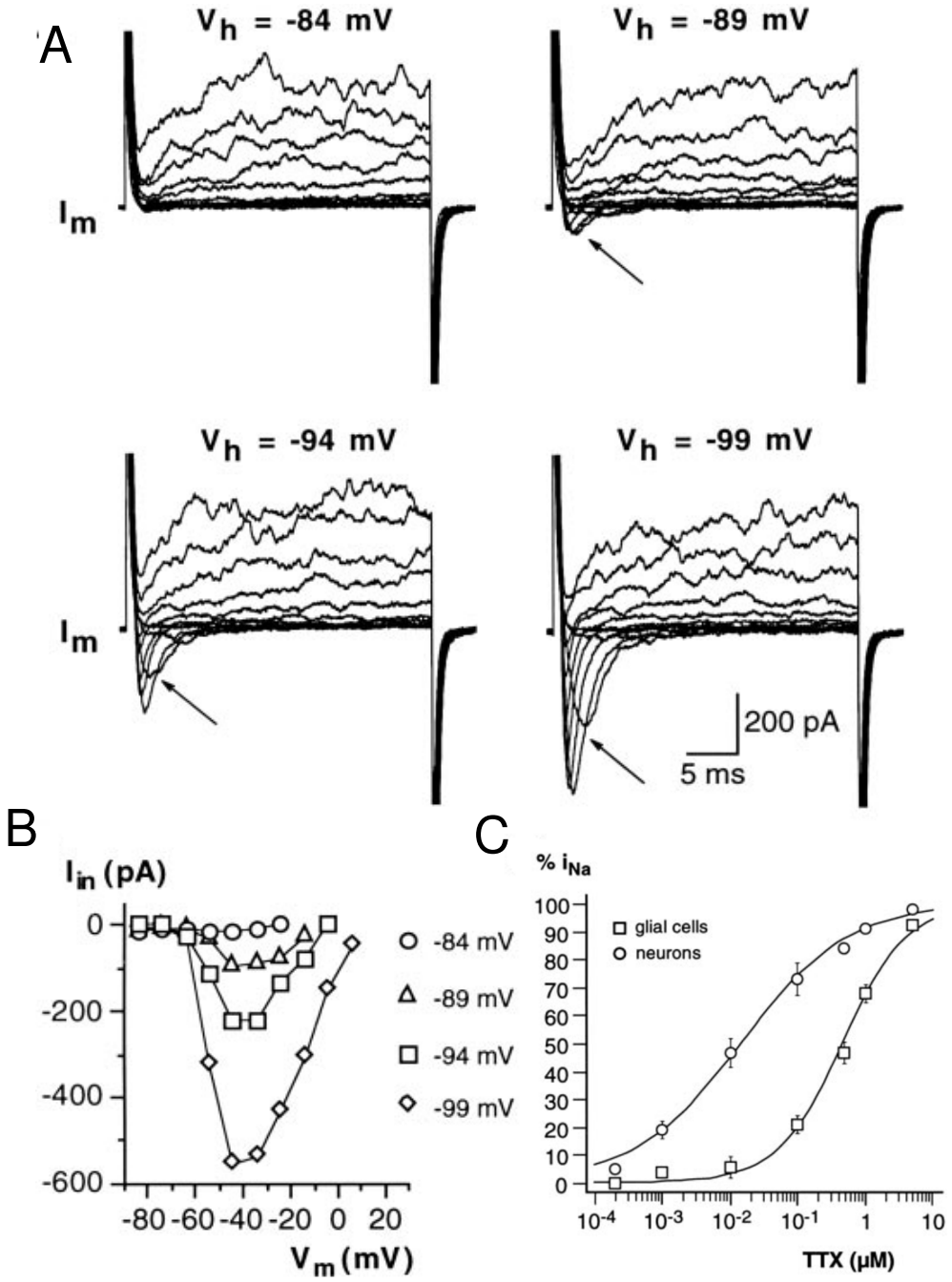

Figure 16. Voltage-gated sodium currents in supporting cells of the VNO. Whole-cell patch clamp recordings were obtained with a series of depolarizing voltage pulses in 10 mV increments from different holding potentials (V_h). When the holding potential was more negative than -84 mV, an inward current (arrows) was visible. (B) Current-voltage relationship of the inward current measured in A. (C) Dose-response curve of the percentage inhibition by TTX of the maximal inward current for supporting cells (□) and vomeronasal sensory neurons (○). Adapted from Ghiaroni et al., 2003.

1.3.2. Calcium Signaling

Up to now, intracellular calcium dynamics studies in supporting cells of the VNO have been conducted using the fluorescence calcium imaging technique only on VNOs from frogs *Xenopus laevis* (Dittrich et al., 2014).

It was determined that VNO supporting cells of frogs *Xenopus laevis* respond to the stimulation by ATP with an increase of intracellular calcium. These cells were responsive to UTP, an agonist of $P2Y_2$ and $P2Y_4$ receptors. VNO supporting cells were not responsive to other P_2Y or P_2X receptor agonist tested including ADP, adenosine, 2-MeSATP, 2-MeSADP, BzATP, UDP, α,β-MeATP and β,γ-MeATP, which represents a screening for most purinergic receptors. The response to UTP but not to other purinergic receptor agonists indicates that the response to ATP is mostly due to the activation of $P2Y_2$ and/or $P2Y_4$ receptors.

The involvement of ionotropic purinergic receptors, P_2X, was excluded due to the fact that ATP-induced calcium transients are dependent on intracellular stores. The depletion of intracellular stores by the calcium ATPase blocker cyclopiazonic acid (CPA), completely ablated the response of the supporting cells to ATP (Figure 17).

In mice, the release of ATP in VNO can be triggered through mechanical stimulation, but this mechanically induced ATP release in completely ablated in the presence of 5 mM carbonexolone, a blocker of pannexin channels and gap junctions (Vick and Delay, 2012). It unknown which vomeronasal cell is responsible for this mechanically induced ATP release.

In rats, the expression of purinergic receptors was studied using immunohistochemistry. The expression of the purinergic ionotropic receptor $P2X_3$ was found in vomeronasal neurons, but not supporting cells of the VNO. The expression of the metabotropic purinergic receptor $P2Y_1$ was particularly strong at the apical surface of the epithelium but still extended back through the rest of the epithelium, this expression pattern did not allow for the distinction between expression in vomeronasal neurons or supporting cells. Sparse cells within the VNO showed positive staining for the metabotropic purinergic receptor $P2Y_2$ (Gayle and Burnstock, 2005).

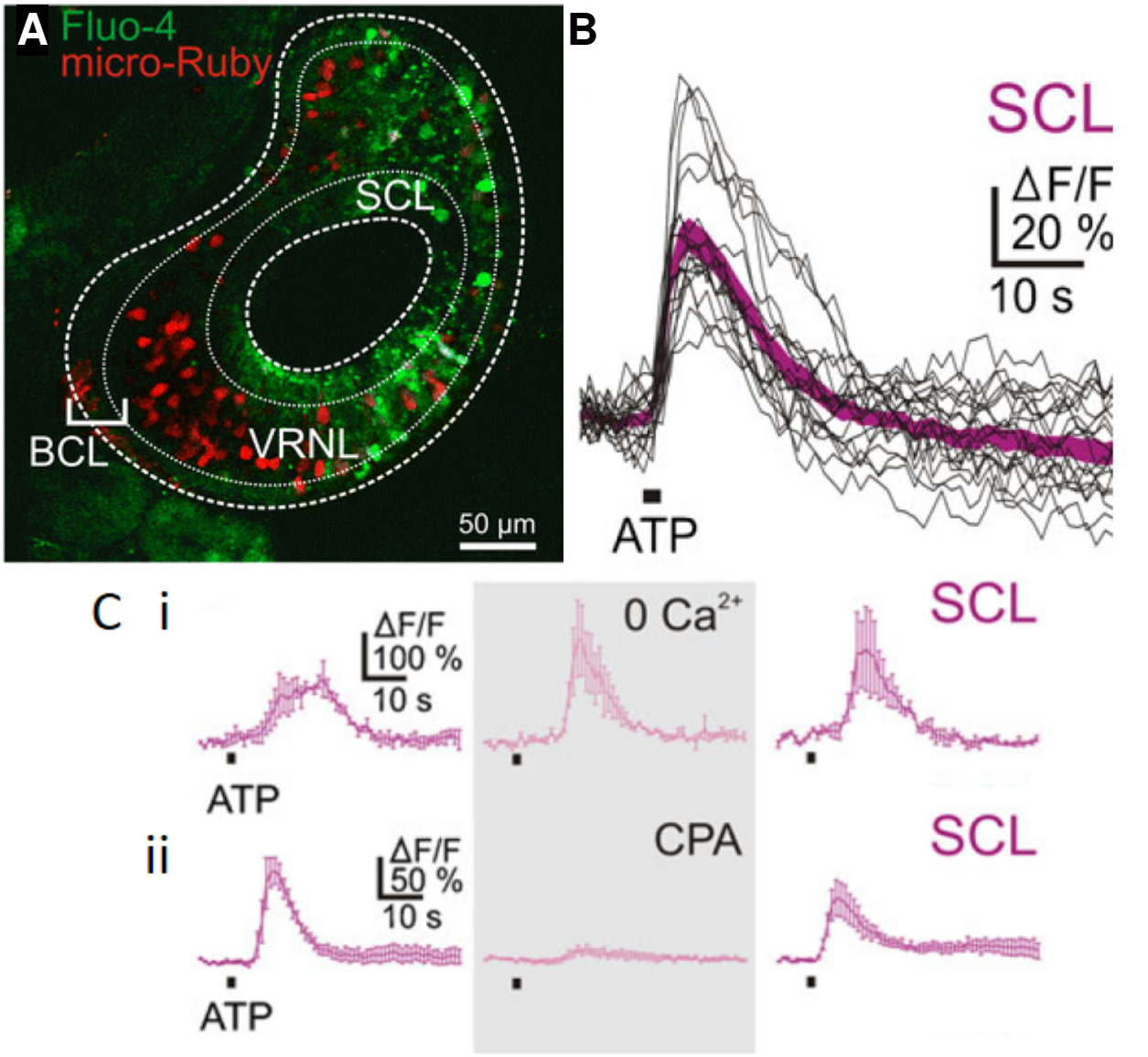

Figure 17. Supporting cells of the VNO of *Xenopus laevis* respond to ATP through the recruitment of intracellular stores of calcium. (A) Acute VNO slice with vomeronasal neurons stained with micro-Ruby (red, backfilled through the olfactory nerve) and Fluo-4 loaded cells (green). (B) Cells of the supporting cell layer (SCL) responding to the perfusion of ATP with a transient increase in intracellular calcium. ATP-induced calcium increases of supporting cells (Ci) in the absence of extracellular calcium, or (Cii) in the presence of CPA, a blocker of calcium ATPases, which depletes intracellular calcium stores. Abbreviations: BCL, basal cells layer; CPA, cyclopiazonic acid; SCL, supporting cell layer; VRNL, vomeronasal receptor neuron layer. Adapted from Dittrich et al., 2014.

1.3.3. Physiological Functions

Supporting cells of the VNO, unlike supporting cells of the olfactory epithelium, lack the expression of aquaporin 4 (Ablimit et al., 2006) and TMEM16A (Amjad et al., 2015), thought to be involved in potassium spatial buffering and mucus ionic regulation, respectively. They do express voltage-gated potassium channels, but potassium spatial buffering capacity is limited if not coupled to a water influx (Amiry-Moghaddam et al., 2003).

Supporting cells of the VNO express metabotropic purinergic receptors that lead to intracellular calcium increase, but it is currently unknown how they use this signaling cascade (Dittrich et al., 2014).

An interesting physiological role for supporting cells of the VNO has been proposed by Matsuoka et al. (2000). They conducted experiments in adult rats to investigate the VNO cell turnover by cutting the nerve fibers connecting the VNO to the bulb. Vomeronasal sensory neurons degenerated, while the number of supporting cells did not change. Moreover, supporting cells were shown to have a decisive role in mitigating degeneration of the VNO by expanding their cellular membrane exposed to the apical surface of the tissue. It was then proposed that a physiological role of VNO supporting cell is the maintenance of the luminal integrity of the tissue during regeneration of vomeronasal neurons (Matsuoka et al., 2000).

2. Aims

1) Determine the role of TMEM16A on the development of the olfactory epithelium;

2) Measure and characterize the calcium-activated chloride currents in supporting cells of the olfactory epithelium;

3) Determine the mechanisms of regulation of calcium signaling in supporting cells of the vomeronasal organ.

3. Results

3.1. Development of the olfactory epithelium and nasal glands in TMEM16A$^{-/-}$ and TMEM16B$^{+/+}$ mice

PLOS | ONE

RESEARCH ARTICLE

Development of the Olfactory Epithelium and Nasal Glands in TMEM16A$^{-/-}$ and TMEM16A$^{+/+}$ Mice

Devendra Kumar Maurya[1¤], Tiago Henriques[1], Monica Marini[2], Nicoletta Pedemonte[2], Luis J. V. Galietta[2], Jason R. Rock[3], Brian D. Harfe[4], Anna Menini[1]*

1 Laboratory of Olfactory Transduction, SISSA, International School for Advanced Studies, Trieste, Italy, **2** Istituto Giannina Gaslini, Genova, Italy, **3** Department of Anatomy, UCSF School of Medicine, San Francisco, CA, United States of America, **4** Department of Molecular Genetics and Microbiology Genetics Institute, University of Florida, College of Medicine, Gainesville, FL, United States of America

¤ Current address: Department of Molecular Biology, Umeå University, Umeå, Sweden
* menini@sissa.it

OPEN ACCESS

Citation: Maurya DK, Henriques T, Marini M, Pedemonte N, Galietta LJV, Rock JR, et al. (2015) Development of the Olfactory Epithelium and Nasal Glands in TMEM16A$^{-/-}$ and TMEM16A$^{+/+}$ Mice. PLoS ONE 10(6): e0129171. doi:10.1371/journal.pone.0129171

Academic Editor: Johannes Reisert, Monell Chemical Senses Center, UNITED STATES

Received: October 9, 2014

Accepted: May 5, 2015

Published: June 11, 2015

Data Availability Statement: All relevant data are within the paper.

Funding: This study was supported by a grant (to AM) from the Italian Ministry of Education, Universities, and Research (MIUR). The funders had no role in study design, data collection and analysis, decision to publish, or preparation of the manuscript.

Competing Interests: The authors have declared that no competing interests exist.

Abstract

TMEM16A/ANO1 is a calcium-activated chloride channel expressed in several types of epithelia and involved in various physiological processes, including proliferation and development. During mouse embryonic development, the expression of TMEM16A in the olfactory epithelium is dynamic. TMEM16A is expressed at the apical surface of the entire olfactory epithelium at embryonic day E12.5 while from E16.5 its expression is restricted to a region near the transition zone with the respiratory epithelium. To investigate whether TMEM16A plays a role in the development of the mouse olfactory epithelium, we obtained the first immunohistochemistry study comparing the morphological properties of the olfactory epithelium and nasal glands in TMEM16A$^{-/-}$ and TMEM16A$^{+/+}$ littermate mice. A comparison between the expression of the olfactory marker protein and adenylyl cyclase III shows that genetic ablation of TMEM16A did not seem to affect the maturation of olfactory sensory neurons and their ciliary layer. As TMEM16A is expressed at the apical part of supporting cells and in their microvilli, we used ezrin and cytokeratin 8 as markers of microvilli and cell body of supporting cells, respectively, and found that morphology and development of supporting cells were similar in TMEM16A$^{-/-}$ and TMEM16A$^{+/+}$ littermate mice. The average number of supporting cells, olfactory sensory neurons, horizontal and globose basal cells were not significantly different in the two types of mice. Moreover, we also observed that the morphology of Bowman's glands, nasal septal glands and lateral nasal glands did not change in the absence of TMEM16A. Our results indicate that the development of mouse olfactory epithelium and nasal glands does not seem to be affected by the genetic ablation of TMEM16A.

Introduction

TMEM16A/ANO1, a member of the family of transmembrane proteins with unknown function 16 [1,2], has been recently identified as a calcium-activated chloride channel [3–5]. TMEM16A is expressed in several types of cells of secretory epithelia, smooth muscle cells [6–8], as well as in cells of sensory systems: cochlea [9–10], retina [11–13], nociceptive neurons [14–15], vomeronasal sensory epithelium [11,16–17], and olfactory epithelium [11,16,18]. TMEM16A is involved in several types of physiological processes [6–7] including proliferation and development.

A role of TMEM16A in proliferation had been already suggested before its identification as a calcium-activated chloride channel. Indeed, TMEM16A was reported to be overexpressed in some malignant tumors and was known by different names, such as DOG1 (Discovered On Gastrointestinal stromal tumor protein 1 [19–20]), TAOS2 (Tumor Amplified and Overexpressed Sequence 2 [21]) overexpressed in oral squamous cell carcinomas, and ORAOV2 (Oral Cancer Overexpressed 2 [22]) overexpressed in oral and esophageal squamous cell carcinomas. In addition to a potential role for TMEM16A in proliferation, suggested by the overexpression of this channel in some tumors, TMEM16A has also been shown to be a regulator of cell proliferation in healthy cells. Indeed, Stanich et al [23] showed that TMEM16A regulates proliferation of interstitial cells of Cajal at the G_1/S transition of the cell cycle.

Some studies also indicated a possible role of TMEM16A in the development of the trachea [24] and the cochlea [10]. Rock et al [24] showed that TMEM16A is expressed in the epithelium of the developing trachea and in the embryonic tracheal muscle of mice. Furthermore, the same authors produced knockout mice for TMEM16A and showed that these mice have alterations in the formation of tracheal cartilage rings and die within one month, possibly because of tracheomalacia. In addition to providing a mouse model of tracheomalacia, these results point out to the possible role of TMEM16A in epithelial and smooth muscle cell organization in development [24]. Reduced transepithelial current and accumulation of mucus in the trachea of these mice indicate that TMEM16A also play a role in secretory processes [25,26]. Additional alterations caused by TMEM16A loss of function include block of gastrointestinal peristalsis and reduced nociception [15,27].

Another study [10], suggested that TMEM16A plays a developmental role in the mouse postnatal developing cochlea. Indeed, these authors showed that supporting cells in the greater epithelial ridge of the cochlea exhibited spontaneous calcium-dependent volume changes that were inhibited by anion channel blockers, indicating that volume changes may be related to the activity of calcium-activated chloride channels. Moreover, volume changes were correlated with the time course and location of TMEM16A expression in the cochlea, suggesting that TMEM16A may be the pacemaker of spontaneous activities in postnatal developing cochlea.

Based on previous studies showing that TMEM16A plays a role in cell proliferation and in development [7,10,24] and on our previous observation that at embryonic day E12.5 TMEM16A immunoreactivity was present at the apical surface of the entire olfactory epithelium, whereas from E16.5 TMEM16A immunoreactivity was restricted to a region near the transition zone with the respiratory epithelium [18], we investigated whether TMEM16A plays a role in the development of the olfactory epithelium. For this purpose, we used immunohistochemistry to identify morphological properties of the olfactory epithelium and nasal glands during mouse embryonic development and at postnatal age in $TMEM16A^{+/+}$ and $TMEM16A^{-/-}$ mice.

Materials and Methods

Ethics Statement

All animals were handled in accordance with the Italian Guidelines for the Use of Laboratory Animals (Decreto Legislativo 27/01/1992, no. 116) and European Union guidelines on animal research (No. 86/609/EEC). Experimental procedures were notified to and approved by the Italian Ministry of Health, Directorate General for Animal Health. The work has been performed on the explanted tissues from sacrificed mice and did not require ethical approval, as stated by the Italian law (decree 116/92). The entire procedure is in accordance with the regulations of the Italian Animal Welfare Act, with the relevant EU legislation and guidelines on the ethical use of animals and is approved by the local Authority Veterinary Service.

Experiments were performed on TMEM16A$^{-/-}$ and TMEM16A$^{+/+}$ littermate mice obtained by breeding TMEM16A$^{+/-}$ mice generated by Rock et al. [24]. Male and female mice were put together for mating in the evening and separated the next morning. If a vaginal plug was observed in the morning, that day was designated as embryonic day 0.5 (E0.5). Once the mouse was positive for vaginal plug, on the prerequisite embryonic day the mouse was anaesthetized by CO_2 inhalation, followed by cervical dislocation. Embryos were removed from the uterus and decapitated. The head region was further processed for immunohistochemistry. For postnatal mice, date of birth was defined as postnatal day 0 (P0). Postnatal mice were anaesthetized by CO_2 inhalation and decapitated. Nose was separated from the rest of head and further processed.

Genotyping protocol

To check the genotype of mouse for *Tmem16a* gene, genotyping for deletion of exon-12 of *Tmem16a* and insertion of PGK-neo cassette was done. Genomic DNA was isolated from the mouse tails by using 5'PRIME Kit (Eppendorf, Milano, Italy), according to manufacturer's protocol. PCR was carried out in a total volume of 25 μl under the following conditions for 40 cycles: 94°C for 5 min (for 1 cycle), 94°C for 30 sec, 60°C for 30 sec and 72°C for 30 sec. The final reaction mixture contained 100 ng of genomic DNA, using Taq Polymerase Master Mix (VWR, Milano, Italy). Two separate PCRs were required to identify homozygous knockout mouse: one for the mutant allele (PGK-neo instead of exon-12) and one for the wild type allele. Wild type allele size was 330 bp and mutant allele was 450 bp. DNA was separated by electrophoresis on 1.5% agarose gel with ethidium bromide.

Primers used:

WT (f): 5′ -CCTATGACTGCCAGGGACGCCC-3′

WT(rev): 5′ -TGTTCCTGTCCCTGCAATGCGG-3′

Mut (f): 5′ -GACGCCCTCCATTGACCC-3′

Mut (rev): 5′ -GCAGTAGAAGGTGGCGCGAAG-3′

Immunohistochemistry

For E12.5 and E14.5 whole head region and for E16.5, E18.5 and P4 dissected out nose was fixed in 4% paraformaldehyde prepared in 0.01 M phosphate-buffered saline (PBS) for overnight at 4°C. Tissues with olfactory epithelium were equilibrated at 4°C in 30% (wt/vol) sucrose until the tissue sank to base in solution for cryoprotection. Then the tissue was embedded in O. C.T. (Bio-optica, Milano, Italy) and stored at −80°C. Before sectioning on cryostat, O.C.T. blocks were kept at −20°C for at least 12 hours. With a cryostat, 12–14 μm coronal sections

were cut and stored (-80°C) for further use. For antigen retrieval, sections were usually treated with SDS 0.5% (wt/vol) in PBS for 15 min. However, for the following primary antibodies: cytokeratin 8, sox2, Ki67, and cytokeratin 5, heat-induced antigen retrieval was used. Sections in 0.01 M citrate buffer (pH 6.0) were heated in a microwave oven for 20 min. After cooling, sections were rinsed three times in PBS. Sections were incubated in a blocking solution [2% FBS (vol/vol) and 0.2% (vol/vol) Triton X-100 in PBS] for 90 min, and then with the primary antibody (diluted in the blocking solution) overnight at 4°C. Sections were then rinsed with 0.1% (vol/vol) Tween 20 in PBS (PBS-T) and incubated with the fluorophore-conjugated secondary antibody (diluted in PBS-T) for 2 h at room temperature. After washing with PBS-T, sections were treated with 0.1 μg/ml DAPI for 30 min, washed with PBS-T, and mounted with Vectashield (Vector Laboratories, Burlingame, CA). Postnatal mice tissues were fixed for 6 hours and processed as described for the embryonic tissues. As far as possible, different embryonic and postnatal tissues were processed in parallel at the same time to avoid any discrepancies in results.

For each age, sections were analyzed from at least three mice obtained from at least two litters.

All chemicals, unless otherwise stated, were purchased from Sigma, Milano, Italy.

The primary antibodies used in this study are listed in Table 1.

Secondary antibodies

The following secondary antibodies obtained from Invitrogen (Eugene, OR, USA), were used: donkey anti-rabbit Alexa Fluor 488 (1:500; catalog no. A21206), donkey anti-goat Alexa Fluor 594 (1:500; catalog no. A11058), goat anti-rabbit Alexa Fluor 594 (1:500; catalog no. A11037), goat anti-mouse Alexa Fluor 488 (1:500; catalog no. A11001)

Table 1. Primary antibodies used in this study.

Primary antibody	Immunogen	Dilution	Manufacturer/catalog number/lot number or clone
Rabbit polyclonal TMEM16A	Synthetic peptides corresponding to amino acid residues 424–519, 628–731 and 904–986 of human TMEM16A	1:50	Abcam/ab53212/GR71118-3
Goat polyclonal TMEM16A	Synthetic peptide corresponding to amino acid residues 825–875 of human TMEM16A	1:50	Santa Cruz Biotech/sc-69343/ H0713
Rabbit polyclonal adenylyl cyclase III (ACIII)	Synthetic peptide corresponding to amino acid residues 1125–1144 of human ACIII	1:100	Santa Cruz Biotech/sc-588/ K0608
Goat polyclonal olfactory marker protein (OMP)	Purified natural rat OMP	1:1000	Wako Chemicals/ 544-10001/ IUP1001
Mouse monoclonal ezrin	Synthetic peptide corresponding to amino acid residues 362–585 of human ezrin	1:100	Abcam/ab4069/3C12
Rabbit monoclonal cytokeratin 8	Synthetic peptide corresponding to amino acid residues 300–350 of human cytokeratin 8	1:150	Novus Biologicals/NB110-56919/ EP1628Y
Rabbit polyclonal aquaporin 5	Synthetic peptide corresponding to 17 amino acid sequence in the cytoplasmic region of rat aquaporin 5	1:150	Calbiochem/178615/D00140208
Goat polyclonal sox2	Synthetic peptide corresponding to amino acid residues 277–293 of human sox2	1:50	Santa Cruz Biotech/sc-17320/ A1314
Goat polyclonal Ki67	Synthetic peptide mapping near the C-terminus of Ki67 of mouse origin	1:150	Santa Cruz Biotech/ sc-7846/ C2012
Rabbit polyclonal cytokeratin 5	Synthetic peptide sequence derived from the C-terminus of the mouse keratin 5 protein	1:200	BioLegend/ 905501/ D14FF0122

doi:10.1371/journal.pone.0129171.t001

Imaging

Immunoreactivity was usually visualized with a confocal microscope (TCS SP2; Leica) using 40X/1.25NA or 63X/1.4NA oil immersion objectives. Images were acquired using Leica software (at 1,024 × 1,024 pixel resolution). All images were taken as average of z-stacks of 1–2 μm thickness. Images in Fig 7 were obtained with a Nikon Eclipse 90i microscope using a Plan Apo VC 60X/1.4NA oil immersion objective. Images were prepared and assembled in Inkscape version 0.48.2. Images were not modified other than to level illumination. Only DAPI signals were enhanced, to show the anatomy of the olfactory epithelium. In any case, data were not altered because of the above adjustments.

Cell counting

To determine cell density, the number of nuclei in a 150 x 150 μm^2 area of the olfactory epithelium was counted with imageJ 1.48v software. As nuclei of the olfactory epithelium have various shapes, we counted the cells manually using the cell counter tool of imageJ 1.48v. Eight coronal sections of 16 μm thickness were collected from each animal. For E14.5 every fourth section was collected, while for E16.5, E18.5 and P4 every seventh section was collected. Approximately 40–47 areas were selected from the septum and turbinates in each animal to count the cells. Areas were chosen randomly at different epithelial thicknesses. In each group at least three animals were used.

Number of cells are reported as average ± SEM. Statistical significance was determined using paired or unpaired Student's *t*-tests and p values <0.05 were considered significant.

Results

Fig 1A shows a schematic diagram of a nose coronal section illustrating the localization of the olfactory epithelium, respiratory epithelium, and various types of glands. The olfactory epithelium is mainly composed of olfactory sensory neurons, supporting cells, and basal cells, as schematized in Fig 1B.

In agreement with our previous observations [18], TMEM16A is expressed at E12.5 at the entire apical surface of the olfactory epithelium (Fig 1C), whereas at P4 it is expressed only in a region of the olfactory epithelium near the transition zone with the respiratory epithelium [Fig 1(D, D1, D2)]. Moreover, Gritli-Linde et al [28] showed a dynamic expression of *Tmem16a* during embryonic development, with the highest expression at E12.5, which greatly decreased after E18.5. TMEM16A has been shown to be involved in various physiological processes, including cell proliferation and development. In the developing olfactory epithelium, mitotic cells are abundant at the apical surface at E12.5 [29,30], and the majority of mitoses occur in the apical layer up to about E14, whereas later proliferative activity is transferred to the basal layer [31,32]. Based on these observations, we investigated the hypothesis that TMEM16A may play a role in cell proliferation and development of the mouse olfactory epithelium by comparing results obtained with TMEM16A$^{-/-}$ and TMEM16A$^{+/+}$ littermates.

Expression of ACIII and OMP in TMEM16A$^{-/-}$ and TMEM16A$^{+/+}$ mice

In a first set of experiments, we investigated the expression of TMEM16A and ACIII, a well-known ciliary marker protein in olfactory sensory neurons [33–35]. In the olfactory epithelium of TMEM16A$^{-/-}$ mice, TMEM16A immunoreactivity was absent, thus confirming the loss of TMEM16A and the specificity of the antibody for this protein, while ACIII was expressed at the apical surface of the olfactory epithelium (Fig 2).

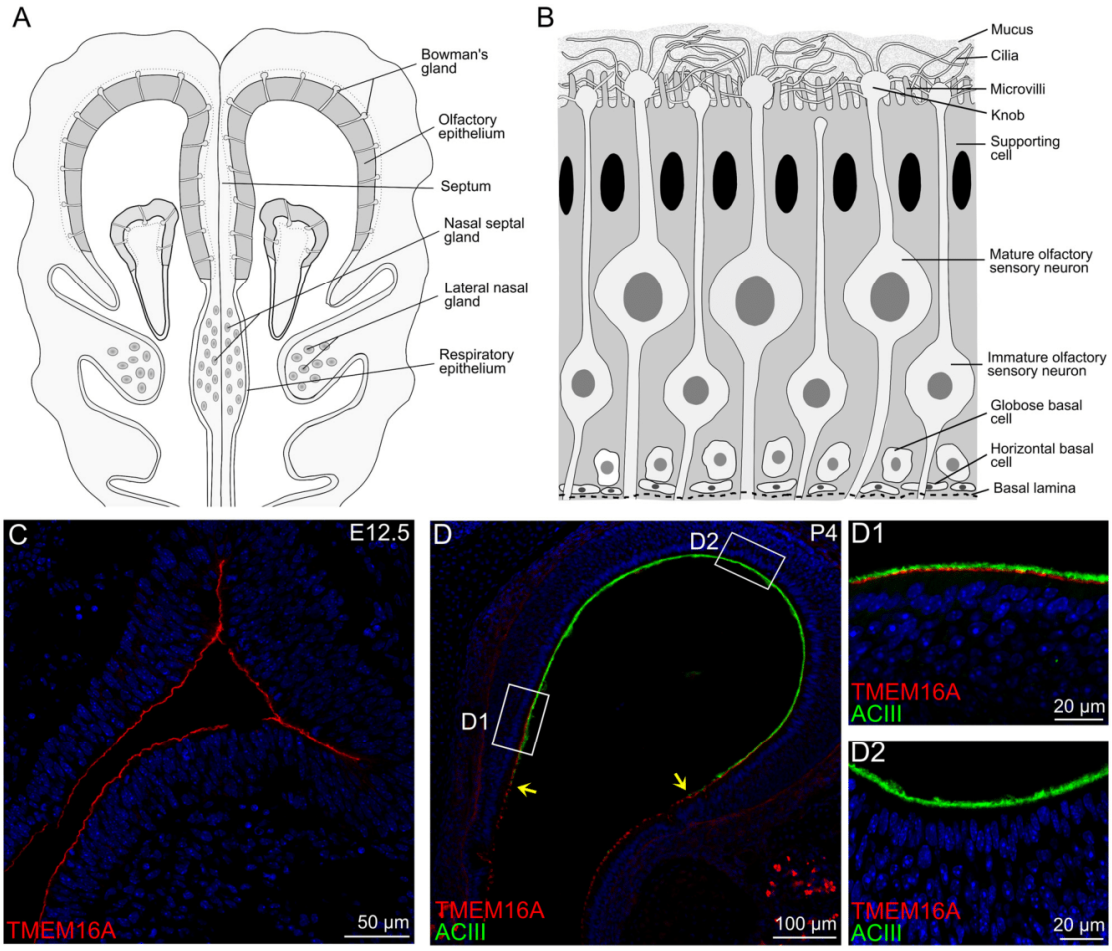

Fig 1. Schematic representations and confocal images of nose coronal sections. A: Schematic diagram of a nose coronal section showing the olfactory epithelium, respiratory epithelium, Bowman's glands, nasal septal glands, and lateral nasal glands. **B:** The pseudostratified olfactory epithelium is mainly composed of supporting cells, olfactory sensory neurons and basal cells. Supporting cells have columnar cell bodies, microvilli at the apical side, and reside in the most apical region of the epithelium. Mature and immature olfactory sensory neurons are bipolar neurons with a single dendritic process projecting toward the apical surface of the epithelium. In mature olfactory sensory neurons, several cilia protrude from the dendritic knob. Two types of basal cells reside near the basal lamina: horizontal basal cells (HBCs) that are attached to the basal lamina, and globose basal cells (GBCs) that are located above the HBC layer. **C-D:** confocal images of coronal sections of the olfactory epithelium at E12.5 and P4. **C:** At E12.5, TMEM16A was expressed at the surface of the entire olfactory epithelium. **D:** At P4, TMEM16A immunoreactivity was present only in the olfactory regions toward the respiratory epithelium. Arrows in (**D**) indicate the transition between olfactory and respiratory epithelium. The apical surface of the olfactory epithelium was well stained by adenylyl cyclase III (ACIII). Higher magnification images taken from the boxed areas are shown in D1 and D2. Cell nuclei were stained by DAPI. Scale bars: C = 50 µm; D = 100 µm; D1-D2 = 20 µm.

doi:10.1371/journal.pone.0129171.g001

In TMEM16A$^{+/+}$ mice, Fig 1C and 1D and Fig 2 confirm our previous results [18], showing that TMEM16A was expressed at E12.5 at the apical surface of the entire olfactory epithelium (Fig 1C), whereas from E16.5 to postnatal age it was expressed only in a region of the olfactory epithelium near the transition zone with the respiratory epithelium (Fig 1D and Fig 2). Fig 2B shows that at E14.5 both ACIII and TMEM16A were expressed at the apical surface of the olfactory epithelium, with ACIII present in small clusters and TMEM16A expressed in a layer just below the ACIII clusters (Fig 2B). At subsequent days of development ACIII

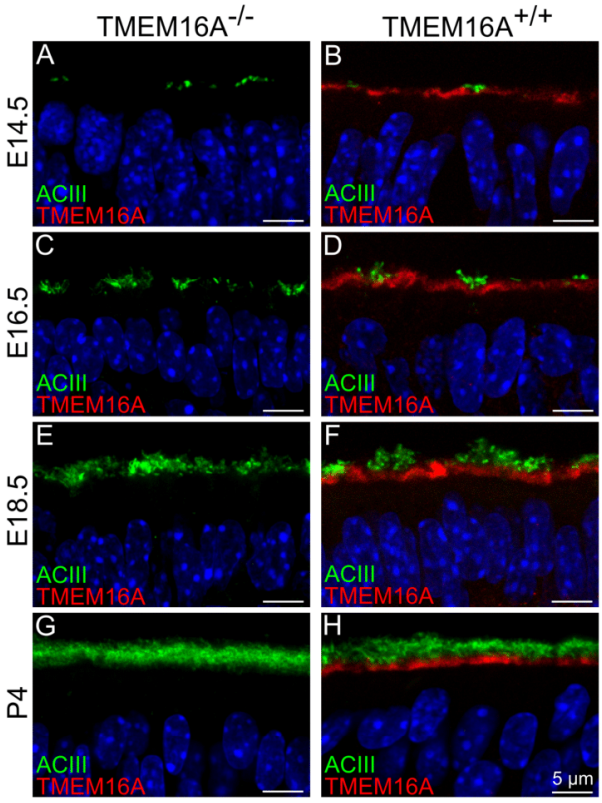

Fig 2. Expression of TMEM16A and ACIII in the olfactory epithelium of TMEM16A$^{-/-}$ and TMEM16A$^{+/+}$ littermate mice. Confocal images of coronal sections of the olfactory epithelium from a region near the transition zone with the respiratory epithelium at E14.5, E16.5, E18.5 and P4. **A, C, E, G:** No immunoreactivity to TMEM16A was detectable in TMEM16A$^{-/-}$ mice (goat anti-TMEM16A). **B, D, F, H:** TMEM16A expression in TMEM16A$^{+/+}$ mice was below adenylyl cyclase III (ACIII) expression and did not overlap with ACIII. TMEM16A immunostaining is discontinuous because of interruption by dendritic knobs of olfactory sensory neurons. Expression of ACIII was similar in both types of mice. Images are averages of z-stacks of ~1.0 µm thickness. Cell nuclei were stained by DAPI. Scale bars = 5 µm.

doi:10.1371/journal.pone.0129171.g002

immunoreactivity increased and at P4 the two antibodies stained distinct layers at the apical surface without any overlap (Fig 2H).

The expression of ACIII in TMEM16A$^{-/-}$ and TMEM16A$^{+/+}$ littermates between E14.5 and P4 appears to be largely similar (Fig 2A–2H). As ACIII is expressed in the cilia of olfactory sensory neurons, genetic ablation of TMEM16A does not seem to cause any large change in the development of the ciliary layer in the olfactory epithelium.

To further evaluate whether TMEM16A has an influence on the maturation of olfactory sensory neurons during development, we used the olfactory marker protein (OMP) as the typical marker for mature olfactory sensory neurons [36]. A small number of OMP immunopositive neurons were present at E14.5 both in TMEM16A$^{-/-}$ and TMEM16A$^{+/+}$ embryos (Fig 3A and 3B). With development, the density of mature neurons increased and firmly packed OMP positive neurons were present at postnatal stage in both types of mice (Fig 3A–3H).

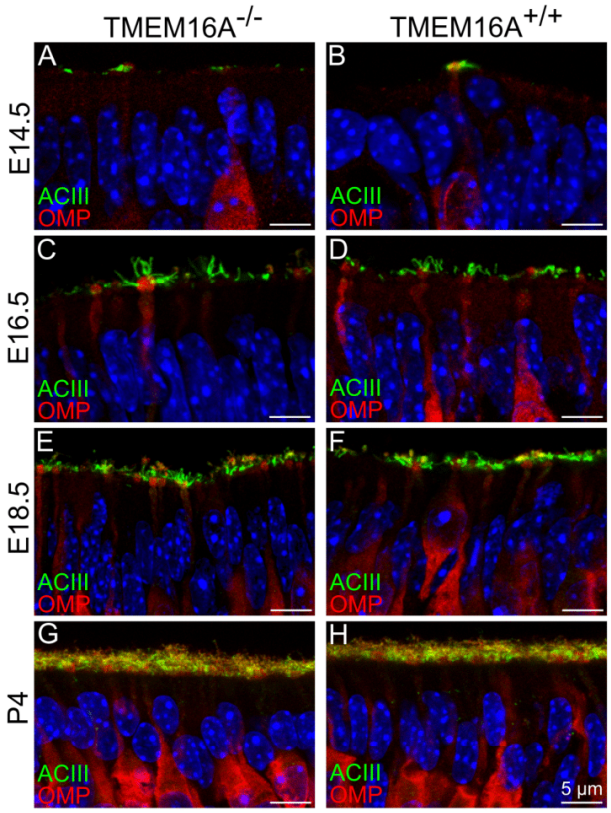

Fig 3. Olfactory sensory neurons in the developing olfactory epithelium of TMEM16A$^{-/-}$ and TMEM16A$^{+/+}$ mice. Mature olfactory sensory neurons express the olfactory marker protein (OMP). Confocal images of coronal sections of the olfactory epithelium at E14.5, E16.5, E18.5 and P4 from TMEM16A$^{-/-}$ (**A, C, E, G**) or TMEM16A$^{+/+}$ (**B, D, F, H**) mice. In both mice, at E14.5 a limited number of mature neurons was present (**A, B**), but the number progressively increased from E16.5 to P4 (**C-H**). ACIII signals were seen in the cilia protruding from the dendritic knob of mature olfactory sensory neurons (**A-H**). Mature neurons expressing OMP and cilia marked by ACIII were similar in TMEM16A$^{-/-}$ and TMEM16A$^{+/+}$ littermates. Images are averages of z-stacks of ~1.5 µm thickness. Cell nuclei were stained by DAPI. Scale bars = 5 µm.

doi:10.1371/journal.pone.0129171.g003

These results indicate that genetic ablation of TMEM16A does not seem to affect the maturation of neurons and cilia in the olfactory epithelium (Figs 2 and 3).

Supporting cells in TMEM16A$^{-/-}$ and TMEM16A$^{+/+}$ mice

We have previously reported that TMEM16A is localized at the apical part of supporting cells and in their microvilli [18]. Here, we investigated whether TMEM16A has an influence on the development of supporting cells. We used cytokeratin 8, ezrin and sox2 as markers for supporting cells. Fig 4A shows that cytokeratin 8, a cytoskeleton protein, stained cells with the typical morphology of supporting cells, characterized by large cell bodies with the shape of an inverted flask located in the apical region of the epithelium and processes reaching the basal part of the epithelium, although microvilli at the apical surface were not marked by cytokeratin 8. Furthermore, we performed a double-labeling experiment using OMP (Fig 4B) and found that cytokeratin 8 and OMP immunoreactivity did not overlap (Fig 4A–4C), indicating that cytokeratin 8

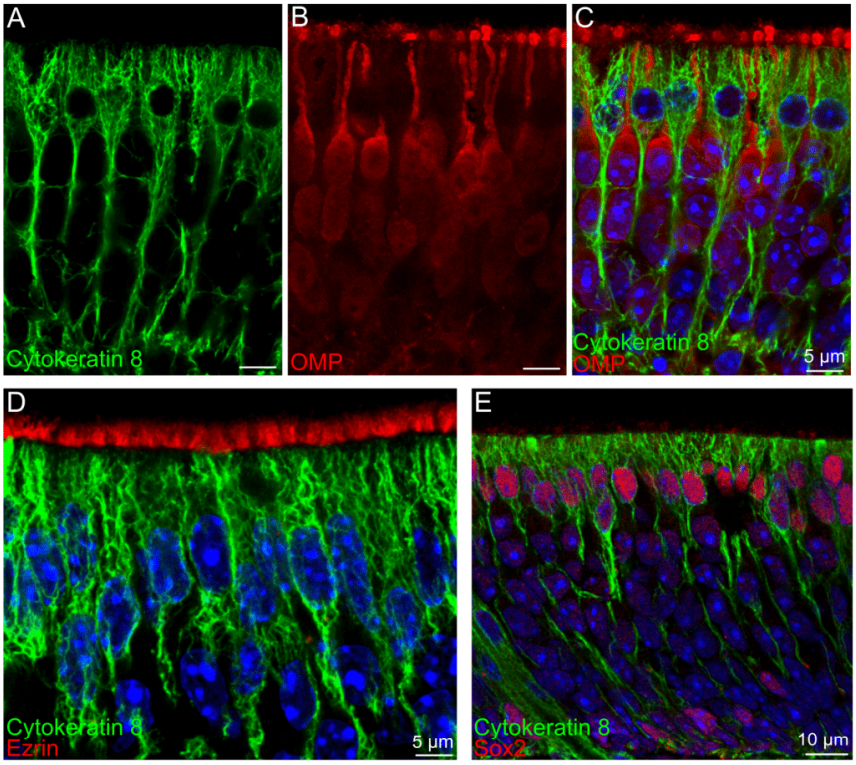

Fig 4. Markers for supporting cells. A-C: Cytokeratin 8 marked cells with the typical morphology of supporting cells. Double staining of cytokeratin 8 with OMP showed no co-localization. **D:** Microvilli of supporting cells stained by ezrin were not stained by cytokeratin 8. **E:** Double staining of cytokeratin 8 with sox2 shows that sox2 is a nuclear marker for supporting cells whose nuclei are located in the apical region of the epithelium. Sox2 also stains nuclei of basal cells. Coronal sections of the olfactory epithelium of wild type mice at P60 (**A-C**), or P4 (**D, E**). Images are averages of z-stacks of ~1.5 µm thickness. Cell nuclei were stained by DAPI. Scale bars: A-C, D = 5 µm; E = 10 µm.

doi:10.1371/journal.pone.0129171.g004

does not label olfactory neurons and is a good marker for supporting cells. Fig 4D further confirms that cytokeratin 8 immunoreactivity was absent in microvilli, as illustrated by the absence of overlap with ezrin immunoreactivity. Fig 4E shows that sox2 is a good marker for the nuclei of supporting cells, although it also stains nuclei of basal cells located near the basal lamina of the olfactory epithelium, in agreement with previous reports [37–39].

To examine the anatomical organization of supporting cells in TMEM16A$^{-/-}$ and TMEM16A$^{+/+}$ littermates, we first stained the olfactory epithelium with cytokeratin 8. Fig 5A–5D shows large similarities in the organization of supporting cells. Furthermore, a comparison among microvilli of supporting cells marked by ezrin (Fig 5E–5H) also shows a similarity in TMEM16A$^{-/-}$ and TMEM16A$^{+/+}$ littermates. Moreover, Fig 5F and 5H confirms our previous observation that TMEM16A was mainly localized to the proximal part of microvilli of supporting cells and to the apical part of supporting cells [18].

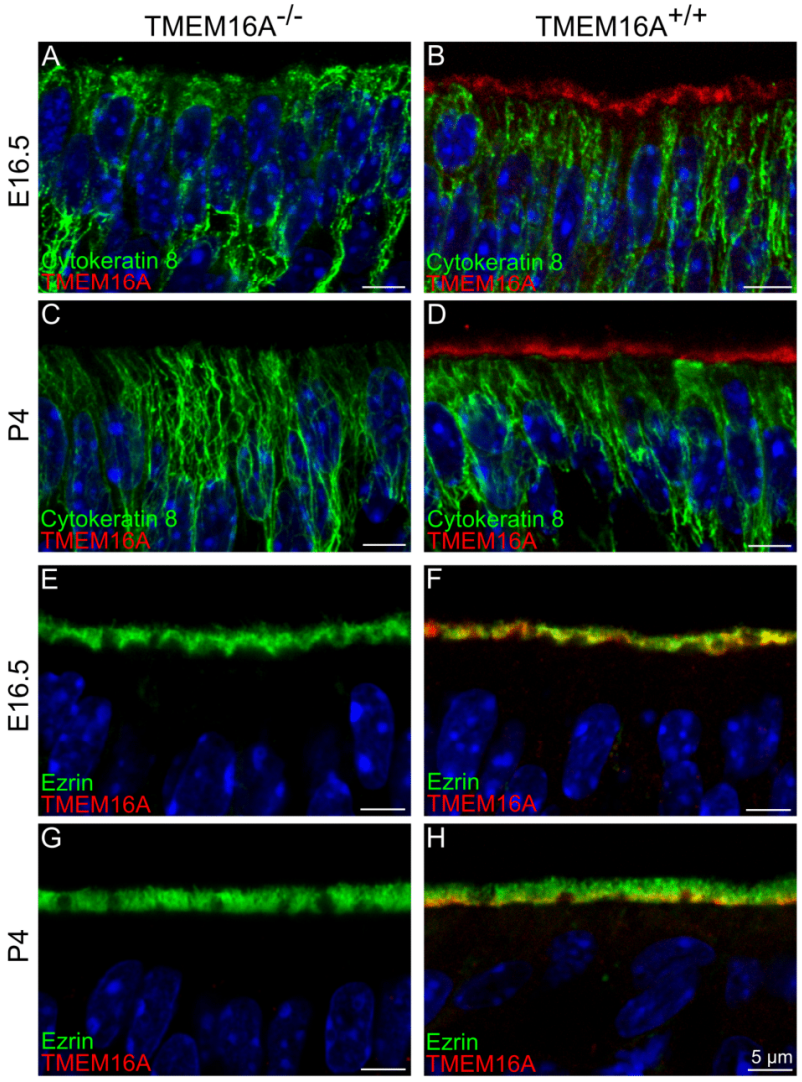

Fig 5. Expression of TMEM16A, cytokeratin 8 and ezrin in the olfactory epithelium of TMEM16A$^{-/-}$ and TMEM16A$^{+/+}$ littermate mice. Confocal images of coronal sections of the olfactory epithelium from a region near the transition zone with the respiratory epithelium at E16.5 and P4 from TMEM16A$^{-/-}$ (**A, C, E, G**) or TMEM16A$^{+/+}$ (**B, D, F, H**). No immunoreactivity to TMEM16A was detectable in TMEM16A$^{-/-}$ mice. **A-D:** Supporting cells marked by cytokeratin 8 were similar in both types of mice. In TMEM16A$^{+/+}$ mice, TMEM16A (goat anti-TMEM16A) and cytokeratin 8 immunoreactivity did not overlap (**B, D**), whereas TMEM16A expression (rabbit anti-TMEM16A) partially overlapped with ezrin immunopositive signals (**F, H**). Supporting cells marked by cytokeratin 8 and microvilli marked by ezrin were similar in both types of mice. Images are averages of z-stacks of ~1.5 µm thickness. Cell nuclei were stained by DAPI. Scale bars = 5 µm.

doi:10.1371/journal.pone.0129171.g005

Quantitative comparison among cell types in TMEM16A$^{-/-}$ and TMEM16A$^{+/+}$ mice

To obtain a quantitative comparison among various cell types in the olfactory epithelium we counted supporting cells, neuronal cells, and basal cells in TMEM16A$^{-/-}$ and TMEM16A$^{+/+}$ mice. Moreover, since from E16.5 to postnatal age TMEM16A expression in the olfactory epithelium of TMEM16A$^{+/+}$ mice is restricted to a region near the transition zone with the respiratory epithelium, we evaluated whether cell numbers change in different regions by comparing cell count analysis obtained in regions with and without TMEM16A expression. Corresponding regions were selected for cell counting in TMEM16A$^{-/-}$ mice.

It is well known that sox2 stains both nuclei of supporting and basal cells and that these cells can be distinguished on the basis of their shape and position in the olfactory epithelium [37–39], as schematically shown in Fig 1B. To count supporting cells we considered oval-shaped nuclei stained by sox2 at the apical part of the olfactory epithelium (Fig 4E).

The average number of supporting cells at E14.5 was 45 ± 2 in TMEM16A$^{+/+}$ mice, not significantly different from the value of 48 ± 2 in TMEM16A$^{-/-}$ mice (p-value > 0.05, Fig 6A). It may be of interest to note that the average number of supporting cells decreased as the age increased, reaching the value of 32 ± 2 at E18.5 for both TMEM16A$^{+/+}$ and TMEM16A$^{-/-}$ mice

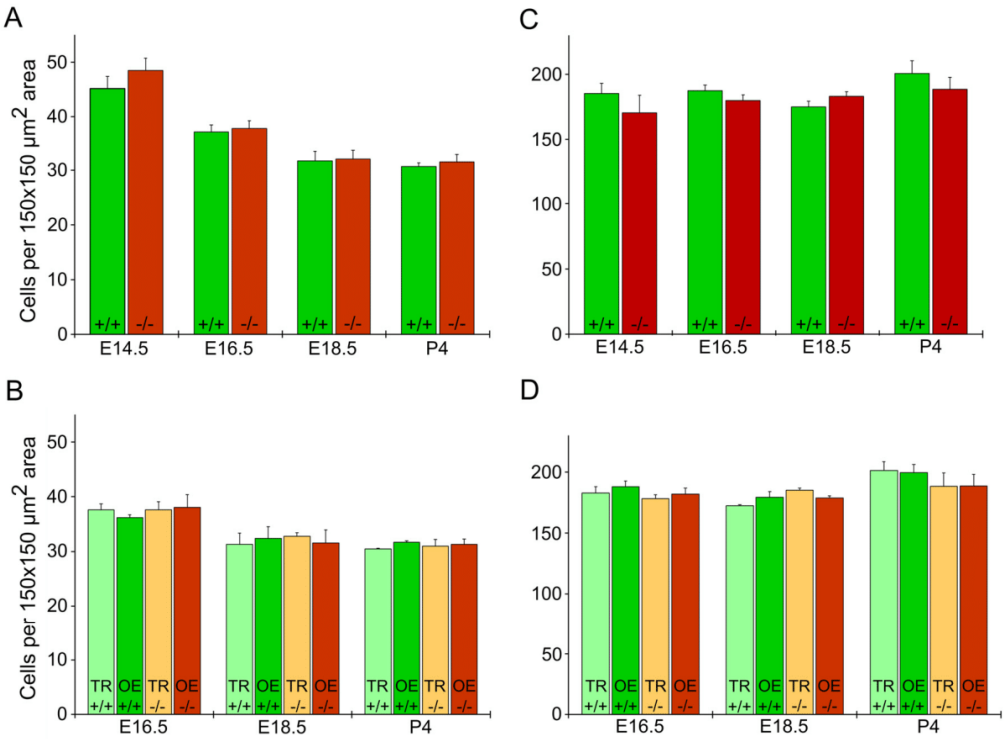

Fig 6. Cell densities in the olfactory epithelium of TMEM16A$^{-/-}$ and TMEM16A$^{+/+}$ littermate mice. Comparison among the average number of supporting cells and olfactory sensory neurons in the olfactory epithelium of TMEM16A$^{-/-}$ and TMEM16A$^{+/+}$ littermate mice. Average number of supporting cells (**A, B**) or neuronal cells (**C, D**) was calculated by counting nuclei in 150 x 150 µm^2 areas from several regions of the olfactory epithelium. **B, D:** Average number of cells calculated near the transition zone with the respiratory epithelium (TR), corresponding to TMEM16A expression in TMEM16A$^{+/+}$ mice, or far from the transition zone (OE). Counting was done in three different animals for each group and presented as average ± SEM.

doi:10.1371/journal.pone.0129171.g006

(p-value < 0.05, Fig 6A). At every age, the average number of supporting cells was not significantly different between TMEM16A$^{+/+}$ and TMEM16A$^{-/-}$ mice (Fig 6A). For ages between E16.5 and P4, we also compared the average number of supporting cells in regions of the olfactory epithelium near and far from the transition zone with the respiratory epithelium and did not find a significant difference, as shown in Fig 6B.

To obtain a quantitative estimate of olfactory sensory neurons (both mature and immature), we counted nuclei that were not stained by sox2 and were located in the middle layer, between the basal and the apical region of the olfactory epithelium. The average number of olfactory sensory neurons at E14.5 was 185 ± 8 in TMEM16A$^{+/+}$ mice, not significantly different from the value of 170 ± 14 in TMEM16A$^{-/-}$ mice (Fig 6C). At every age, the average number of neurons was not significantly different between TMEM16A$^{+/+}$ and TMEM16A$^{-/-}$ mice (Fig 6C). As observed for supporting cells for ages between E16.5 and P4, also the average number of olfactory sensory neurons in regions of the olfactory epithelium near and far from the transition zone with the respiratory epithelium was not significant different, as shown in Fig 6D.

Furthermore, we estimated the number of horizontal and globose basal cells at P4. Horizontal basal cells lie near the basal lamina, while globose basal cells are located above the layer of horizontal basal cells (Fig 1B). We used cytokeratin 5 to identify horizontal basal cells [40–41], and Ki67 to stain globose basal cells (Fig 7A–7F). Ki67 is a marker of proliferating cells in all phases of the proliferating cycle, except for G0, that is often used as a marker for globose basal cells [42–45].

At P4, the average number of horizontal basal cells was 7 ± 1 in TMEM16A$^{+/+}$ mice, not significantly different from the value of 8 ± 1 in TMEM16A$^{-/-}$ mice (Fig 7G). The average number of globose basal cells was 15 ± 1 in TMEM16A$^{+/+}$ mice, not significantly different from the value of 15 ± 2 in TMEM16A$^{-/-}$ mice (Fig 7G). Furthermore, we also compared the average numbers in regions near and far from the transition zone with the respiratory epithelium and did not find a significant difference, as shown in Fig 7H.

In addition, in agreement with previous studies, we found that very few horizontal basal cells are immunopositive for proliferating markers in the normal olfactory epithelium [40]. Indeed, out of 2787 cells stained by cytokeratin 5 in TMEM16A$^{+/+}$ and TMEM16A$^{-/-}$ mice we found only 16 cells (0.006%) co-stained by Ki67.

Taken together, these results indicate that genetic ablation of TMEM16A does not significantly affect the average number of olfactory sensory neurons and supporting cells during mouse embryonic development and at postnatal age. Moreover, the average number of horizontal basal cells and globose basal cells at P4 also remained similar in the presence and in the absence of TMEM16A.

Bowman and nasal glands in TMEM16A$^{-/-}$ and TMEM16A$^{+/+}$ mice

We investigated the expression of TMEM16A in Bowman's glands, nasal septal glands, and lateral nasal glands, whose localization is schematically represented in Fig 1A, and used aquaporin 5 as a marker for these glands [46].

Fig 8A and 8D shows that aquaporin 5 stained the internal wall of the duct of a Bowman's gland as well as microvilli of supporting cells. Previous reports showed expression of TMEM16A in the duct of Bowman's glands and in the luminal surface of nasal septal glands and lateral nasal glands [16]. However, in TMEM16A$^{+/+}$ mice, we did not find expression of TMEM16A in Bowman's glands, whereas the luminal surface of nasal septal glands and lateral nasal glands expressed both TMEM16A and aquaporin 5 (Fig 8B and 8C). A comparison with results from TMEM16A$^{-/-}$ mice shows that immunostaining of aquaporin 5 remains unchanged, whereas TMEM16A immunoreactivity was absent (Fig 8D–8F). The morphology of

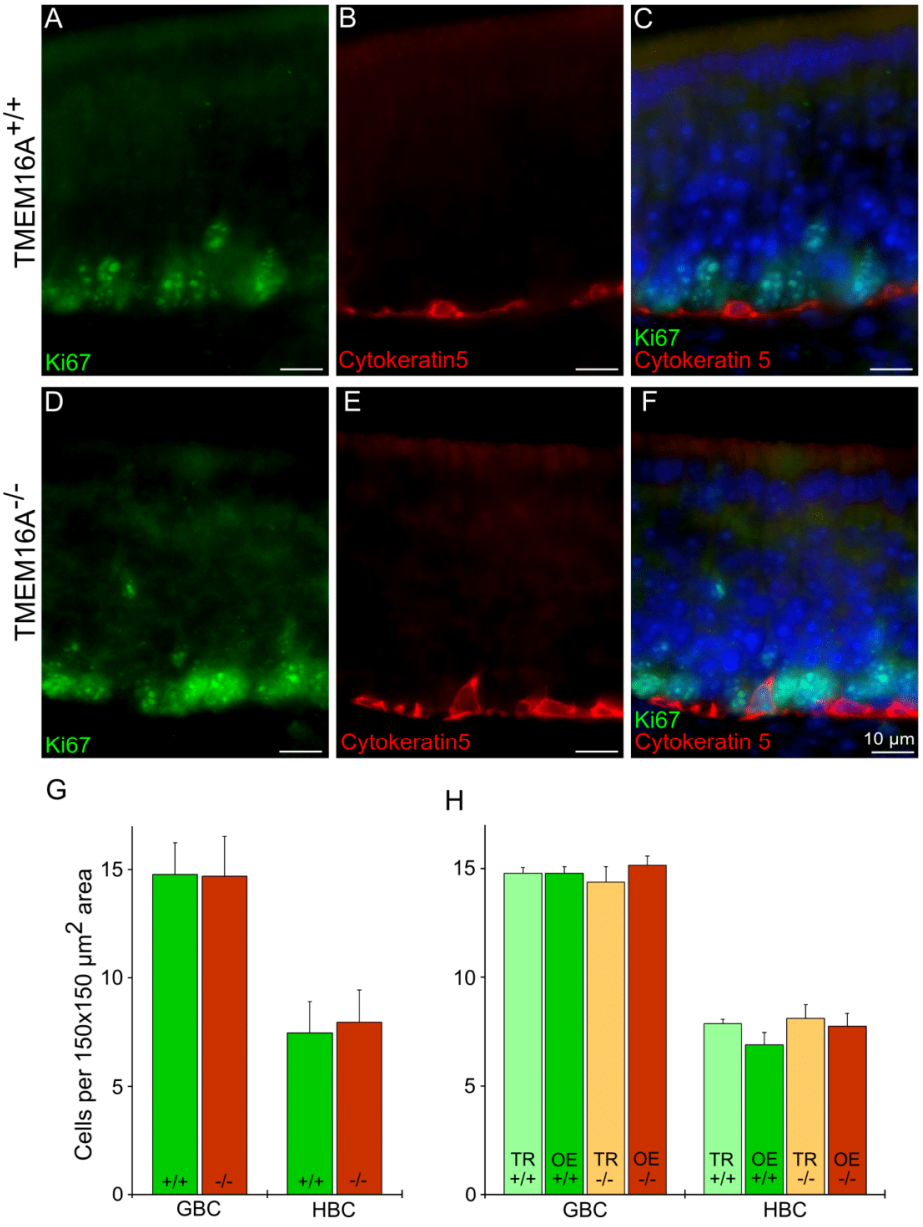

Fig 7. Expression of cytokeratin 5 and Ki67 in the olfactory epithelium of TMEM16A$^{-/-}$ and TMEM16A$^{+/+}$ littermate mice. Confocal images of coronal sections of the olfactory epithelium from a region near the transition zone with the respiratory epithelium at P4 from TMEM16A$^{+/+}$ (**A-C**) and TMEM16A$^{-/-}$ (**D-F**) mice. Cell nuclei were stained by DAPI. Scale bars = 10 µm. **G:** Comparison among the average number of horizontal (HBC) and globose (GBC) basal cells in the olfactory epithelium of TMEM16A$^{+/+}$ and TMEM16A$^{-/-}$ littermate mice. Average numbers of HBCs or GBCs were calculated by counting nuclei in 150 x 150 µm^2 areas from several regions of the olfactory epithelium. **H:** Average number of cells calculated near the transition zone with the respiratory epithelium (TR), corresponding to TMEM16A expression in TMEM16A$^{+/+}$ mice, or far from the transition zone (OE). Counting was done in three different animals for each group and presented as average ± SEM.

doi:10.1371/journal.pone.0129171.g007

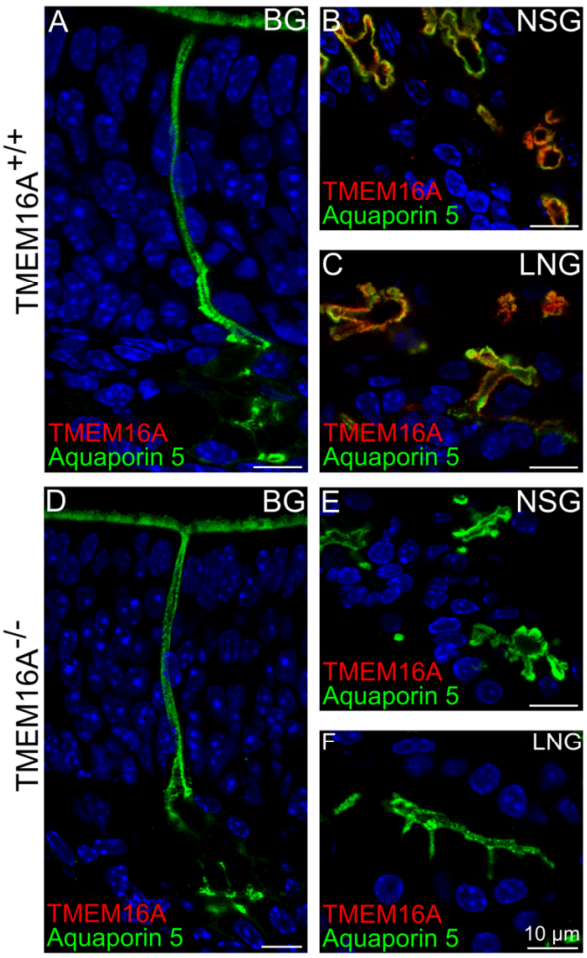

Fig 8. Expression of TMEM16A in various nasal glands of TMEM16A$^{-/-}$ and TMEM16A$^{+/+}$ littermate mice. Expression of TMEM16A and aquaporin 5 in the Bowman's gland (BG), nasal septal gland (NSG) and lateral nasal gland (LNG) of TMEM16A$^{-/-}$ and TMEM16A$^{+/+}$ littermate mice. **A, D:** aquaporin 5 immunopositive signals were seen in Bowman's glands in P4 mice. Aquaporin 5 expression in glands and ducts is clearly visible. TMEM16A immunoreactivity (goat anti-TMEM16A) was not present in Bowman's glands of TMEM16A$^{-/-}$ nor of TMEM16A$^{+/+}$ littermate mice (**A, D**). However, aquaporin 5 and TMEM16A were co-expressed in nasal septal glands (**B**) and lateral nasal glands (**C**) of TMEM16A$^{+/+}$ mice. No immunoreactivity to TMEM16A was detectable in TMEM16A$^{-/-}$ mice (**E, F**). Glands marked by aquaporin 5 were similar in both types of mice. Images are averages of z-stacks of thickness of ~2.0 µm for **A, D**, or ~1 µm for **B, C, E, F**. Cell nuclei were stained by DAPI. Scale bars = 10 µm.

doi:10.1371/journal.pone.0129171.g008

Bowman's gland, nasal septal glands and lateral nasal glands remained the same in both types of mice.

Thus, the absence of TMEM16A does not seem to influence the development of Bowman's glands, nasal septal glands and lateral nasal glands.

Discussion

In this study, we have obtained for the first time immunohistochemistry data comparing morphological and anatomical properties of the olfactory epithelium and of Bowman's and nasal glands during mouse embryonic development and at postnatal ages in TMEM16A$^{+/+}$ and TMEM16A$^{-/-}$ mice.

Olfactory sensory neurons and supporting cells

As TMEM16A$^{-/-}$ mice die before reaching P30 and 90% of them die before P9, we restricted our study up to the age of P4. In the first part of this study, we showed that the development and the morphology of olfactory sensory neurons were similar between TMEM16A$^{+/+}$ and TMEM16A$^{-/-}$ mice. Interestingly, an *in vitro* study suggested that TMEM16A is involved in the early phase of ciliogenesis [47]. In the olfactory epithelium, we did not find expression of TMEM16A in the cilia of olfactory sensory neurons [18]. Furthermore, the similar morphology of cilia and knobs in TMEM16A$^{+/+}$ and TMEM16A$^{-/-}$ mice indicates that TMEM16A does not mediate ciliogenesis in olfactory sensory neurons.

To investigate whether TMEM16A has an influence on the development of supporting cells we first used cytokeratin 8 as a marker for supporting cells. Cytokeratin 8 or keratin 8 is a subtype of keratin intermediate filaments. It is type II (basic) keratin and is found associated with type I (acidic) cytokeratin 18 and cytokeratin 19 in various epithelial cells [48–50]. We found that cytokeratin 8 is a selective marker for supporting cells of the olfactory epithelium, indeed cytokeratin 8 immunostaining revealed cells with the typical morphology of supporting cells and, in addition, did not overlap with the immunopositive signals of OMP that stains mature olfactory sensory neurons. As cytokeratin 8 stains the cytoskeleton, its use allows the investigation of changes in supporting cell cytoskeleton during development. Both cytokeratin 8 and cytokeratin 18 are the abundant intermediate filament subtypes during mouse embryonic development [51]. Using cytokeratin 8 as a marker for supporting cell cytoskeleton, we found that at E14.5 the cytoskeleton was loosely organized and individual filaments of the cytoskeleton could be observed (data not shown). In postnatal mice, cytokeratin 8 immunopositive cytoskeletons became densely packed and supporting cells' nuclei aligned in the top layer of the olfactory epithelium. In TMEM16A$^{+/+}$ mice, TMEM16A expression was observed just above the cytokeratin 8 immunopositive signals, but we did not found any overlap in their expression (Fig 5). TMEM16A$^{-/-}$ mice were devoid of TMEM16A expression, but cytokeratin 8 expression pattern remained very similar to that observed in TMEM16A$^{+/+}$ littermate mice, indicating that organization and morphology of supporting cells were not largely affected by the absence of TMEM16A.

TMEM16A has been shown to interact with ezrin in salivary gland epithelial cells [52]. We confirmed our previous observation that TMEM16A was expressed in the apical part of supporting cells and in their apical microvilli marked by ezrin [18]. Double staining of TMEM16A with ezrin showed that at E16.5 TMEM16A and ezrin immunoreactivity largely overlapped, whereas at later ages TMEM16A was only expressed in the proximal part of microvilli. A very similar pattern of expression was observed in TMEM16A$^{-/-}$ mice. A comparison between ezrin expression in microvilli in TMEM16A$^{+/+}$ and TMEM16A$^{-/-}$ littermate mice indicates that microvilli development did not seem to be largely altered by the absence of TMEM16A.

It is of interest to note that TMEM16A, ezrin and cytokeratin 8 expressed in supporting cells, but cytokeratin 8 immunoreactivity did not even partially overlap with TMEM16A or ezrin immunoreactivity (Fig 4D, and Fig 5A–5D). An explanation for the absence of overlap between cytokeratin 8 and TMEM16A may arise from the ultrastructural study of the morphology of supporting cells by Frisch [53]. Indeed, Frisch [53] reported that, at the apical part

of supporting cells, the cytoplasm seems to be strongly gelated and devoid of cellular organelles. Indeed, we observed a space between ezrin and cytokeratin 8 immunoreactivity (Fig 4D), which resembles the apical organelle free area described by Frisch [53]. TMEM16A was expressed in the free apical region of supporting cells and in the proximal part of microvilli (Fig 5). A similar free space without cellular organelles just below microvilli has also been reported in intestinal brush border cells [54].

TMEM16A plays a role in cell proliferation in several systems. For example, proliferation of interstitial cells of Cajal in TMEM16A$^{-/-}$ mice has been shown to be severely affected by the absence of TMEM16A [23]. In addition, TMEM16A is widely known for its role in carcinogenic tumor proliferation [19–22,55,56]. Several studies from cancerous cell lines showed that cell proliferation was severely affected by reducing TMEM16A expression with siRNA or inhibiting its activity by using TMEM16A blockers [23,57,58], although other studies showed that TMEM16A overexpression did not affect proliferation [55,58–60].

In the olfactory epithelium, Gritli-Linde et al [28] showed that *Tmem16a* expression was high at E12.5, but greatly decreased after E18.5. We observed TMEM16A expression in supporting cells all over the olfactory epithelium during early stages of development (E12.5 and E14.5), whereas from E16.5 onward TMEM16A expression became restricted toward the transition zone between the olfactory and the respiratory epithelium [18]. In the early stages of development dividing cells are abundant in the apical part of the olfactory epithelium [31,32] and TMEM16A may play a role in cell division. Based on these observations, we counted the number of supporting cells and of olfactory sensory neurons and found that at E14.5 the average number of supporting cells was significantly higher than average values at later stages of development. However, similar values were estimated in TMEM16A$^{+/+}$ and TMEM16A$^{-/-}$ littermate mice, indicating that TMEM16A did not play a role in this process.

The average number of olfactory sensory neurons was not significantly different from E14.5 to P4 and between TMEM16A$^{+/+}$ and TMEM16A$^{-/-}$ mice. In addition, the average number of globose basal cells and of horizontal basal cells at P4 remained similar in the two types of mice indicating that TMEM16A expression does not affect proliferation in the olfactory epithelium.

Bowman's and nasal glands

TMEM16A is expressed in various secretory epithelia and glands and regulates anion secretion [25–27,61–62]. The nasal cavity contains several types of secretory glands, such as Bowman's glands, nasal septal glands and lateral nasal glands. The olfactory epithelium is directly exposed to changes in environment and prone to getting in contact with hazardous chemicals and stimuli. The apical part of the olfactory epithelium is always covered with mucus, which continuously eliminates the unwanted molecules from the surface. Mucus is primarily secreted by Bowman's gland and supporting cells are involved in mucus secretion and ionic composition maintenance [53,63].

Aquaporin 5, a water channel, is expressed in Bowman's gland and supporting cells' microvilli [46,64]. We observed aquaporin 5 expression in the duct cells and secretory acinar cells of Bowman's gland both in TMEM16A$^{+/+}$ and TMEM16A$^{-/-}$ littermate mice (Fig 8). We could distinguish only a limited number of completely formed Bowman's glands at E16.5 (data not shown), while at E18.5 and in postnatal mice, numerous Bowman's glands were present. We did not find TMEM16A expression in Bowman's glands between E16.5 and P4. However, one study showed expression of TMEM16A in Bowman's glands in adult mice and rats [16]. As the majority of TMEM16A$^{-/-}$ mice die by P9, our study was limited to P4, and we cannot exclude the possibility that TMEM16A is expressed in Bowman's glands in adult mice. We found that at P4 nasal septal glands and lateral nasal glands showed a strong TMEM16A immunopositive

signal. In both types of glands TMEM16A was expressed in the apical region of secretory acinar cells and in the luminal surface of the glands, where it coexpressed with aquaporin 5 (Fig 8).

In TMEM16A$^{-/-}$ mice, aquaporin 5 immunopositive signals were similar to those observed in TMEM16A$^{+/+}$ mice showing that the morphology of Bowman's glands, nasal septal glands and lateral nasal glands was not largely modified by the absence of TMEM16A.

Conclusions

In conclusion, our data provide the first immunohistochemistry study comparing the development of the olfactory epithelium in TMEM16A$^{+/+}$ and TMEM16A$^{-/-}$ littermate mice during embryonic development. We did not find any significant difference in the olfactory epithelium up to P4 between the two types of mice, indicating that TMEM16A does not seem to be involved in proliferation and development of the olfactory epithelium. As TMEM16A$^{-/-}$ mice die soon after birth, preventing functional and behavioral studies in adult mice, the development and use of conditional knockout mice for TMEM16A will allow planning of additional experiments to improve our present knowledge of the function of TMEM16A in the olfactory system.

Acknowledgments

We thank Prof. Staffan Bohm (Department of Molecular Biology, Umeå University, Sweden) for his kind generosity allowing DKM to perform experiments on basal cells in his laboratory. We thank Prof. Sidney Simon (Duke University, Durham, USA) and all members of the laboratory at SISSA for constructive discussions. We would also like to acknowledge the help of Elettra Grdina, Angela Morriello and Angel Pascual Camerota for their support in mice breeding at the SISSA animal house facility.

Author Contributions

Conceived and designed the experiments: DKM, AM. Performed the experiments: DKM, TH. Analyzed the data: DKM, TH, AM. Contributed reagents/materials/analysis tools: MM, NP, LJVG, JRR, BDH. Wrote the paper: DKM, LJVG, JRR, BDH, AM.

References

1. Tsutsumi S, Kamata N, Vokes TJ, Maruoka Y, Nakakuki K, Enomoto S, et al. The novel gene encoding a putative transmembrane protein is mutated in gnathodiaphyseal dysplasia (GDD). Am J Hum Genet. 2004; 74 (6):1255–1261. doi: 10.1086/421527 PMID: 15124103
2. Galindo BE, Vacquier VD. Phylogeny of the TMEM16 protein family: some members are overexpressed in cancer. Int J Mol Med. 2005; 16 (5):919–924. doi: 10.3892/ijmm.16.5.919 PMID: 16211264
3. Caputo A, Caci E, Ferrera L, Pedemonte N, Barsanti C, Sondo E, et al. TMEM16A, a membrane protein associated with calcium-dependent chloride channel activity. Science. 2008; 322 (5901):590–594. doi: 10.1126/science.1163518 PMID: 18772398
4. Schroeder BC, Cheng T, Jan YN, Jan LY. Expression cloning of TMEM16A as a calcium-activated chloride channel subunit. Cell. 2008; 134 (6):1019–1029. doi: 10.1016/j.cell.2008.09.003 PMID: 18805094
5. Yang YD, Cho H, Koo JY, Tak MH, Cho Y, Shim WS, et al. TMEM16A confers receptor-activated calcium-dependent chloride conductance. Nature. 2008; 455 (7217):1210–1215. doi: 10.1038/nature07313 PMID: 18724360
6. Huang F, Wong X, Jan LY. International Union of Basic and Clinical Pharmacology. LXXXV: calcium-activated chloride channels. Pharmacol Rev. 2012; 64 (1):1–15. doi: 10.1124/pr.111.005009 PMID: 22090471
7. Pedemonte N, Galietta LJV. Structure and function of TMEM16 proteins (anoctamins). Physiol Rev. 2014; 94 (2):419–459. doi: 10.1152/physrev.00039.2011 PMID: 24692353
8. Jang Y, Oh U. Anoctamin 1 in secretory epithelia. Cell Calcium. 2014; 55 (6):355–361. doi: 10.1016/j.ceca.2014.02.006 PMID: 24636668

9. Jeon JH, Park JW, Lee JW, Jeong SW, Yeo SW, Kim IB. Expression and immunohistochemical localization of TMEM16A/anoctamin 1, a calcium-activated chloride channel in the mouse cochlea. Cell Tissue Res. 2011; 345 (2):223–230. doi: 10.1007/s00441-011-1206-6 PMID: 21779783

10. Yi E, Lee J, Lee CJ. Developmental Role of Anoctamin-1/TMEM16A in Ca(2+)-Dependent Volume Change in Supporting Cells of the Mouse Cochlea. Exp Neurobiol. 2013; 22 (4):322–329. doi: 10.5607/en.2013.22.4.322 PMID: 24465148

11. Billig GM, Pál B, Fidzinski P, Jentsch TJ. Ca2+-activated Cl– currents are dispensable for olfaction. Nat Neurosci. 2011; 14 (6):763–769. doi: 10.1038/nn.2821 PMID: 21516098

12. Mercer AJ, Rabl K, Riccardi GE, Brecha NC, Stella SL Jr, Thoreson WB. Location of release sites and calcium-activated chloride channels relative to calcium channels at the photoreceptor ribbon synapse. J Neurophysiol. 2011; 105 (1):321–335. doi: 10.1152/jn.00332.2010 PMID: 21084687

13. Jeon JH, Paik SS, Chun MH, Oh U, Kim IB. Presynaptic Localization and Possible Function of Calcium-Activated Chloride Channel Anoctamin 1 in the Mammalian Retina. PLoS ONE. 2013; 8 (6):e67989. doi: 10.1371/journal.pone.006798 PMID: 23840801

14. Liu B, Linley JE, Du X, Zhang X, Ooi L, Zhang H, et al. The acute nociceptive signals induced by bradykinin in rat sensory neurons are mediated by inhibition of M-type K+ channels and activation of Ca2+-activated Cl- channels. J Clin Invest. 2010; 120 (4):1240–1252. doi: 10.1172/JCI41084 PMID: 20335661

15. Cho H, Yang YD, Lee J, Lee B, Kim T, Jang Y, et al. The calcium-activated chloride channel anoctamin 1 acts as a heat sensor in nociceptive neurons. Nat Neurosci. 2012; 15 (7):1015–1021. doi: 10.1038/nn.3111 PMID: 22634729

16. Dauner K, Lissmann J, Jeridi S, Frings S, Möhrlen F. Expression patterns of anoctamin 1 and anoctamin 2 chloride channels in the mammalian nose. Cell Tissue Res. 2012; 347 (2):327–341. doi: 10.1007/s00441-012-1324-9 PMID: 22314846

17. Dibattista M, Amjad A, Maurya DK, Sagheddu C, Montani G, Tirindelli R, et al. Calcium-activated chloride channels in the apical region of mouse vomeronasal sensory neurons. J Gen Physiol. 2012; 140 (1):3–15. doi: 10.1085/jgp.201210780 PMID: 22732308

18. Maurya DK, Menini A. Developmental expression of the calcium-activated chloride channels TMEM16A and TMEM16B in the mouse olfactory epithelium. Dev Neurobiol. 2014; 74 (7):657–675. doi: 10.1002/dneu.22159 PMID: 24318978

19. West RB, Corless CL, Chen X, Rubin BP, Subramanian S, Montgomery K, et al. The novel marker, DOG1, is expressed ubiquitously in gastrointestinal stromal tumors irrespective of KIT or PDGFRA mutation status. Am J Pathol 2004; 165 (1):107–113. doi: 10.1016/S0002-9440(10)63279-8 PMID: 15215166

20. Espinosa I, Lee C-H, Kim MK, Rouse BT, Subramanian S, Montgomery K, et al. A novel monoclonal antibody against DOG1 is a sensitive and specific marker for gastrointestinal stromal tumors. Am J Surg Pathol. 2008; 32 (2):210–218. doi: 10.1097/PAS.0b013e3181238cec PMID: 18223323

21. Huang X, Godfrey TE, Gooding WE, McCarty KS Jr, Gollin S. Comprehensive genome and transcriptome analysis of the 11q13 amplicon in human oral cancer and synteny to the 7F5 amplicon in murine oral carcinoma. Genes Chromosomes Cancer. 2006; 45 (11):1058–1069. doi: 10.1002/gcc.20371 PMID: 16906560

22. Kashyap MK, Marimuthu A, Kishore CJH, Peri S, Keerthikumar S, Prasad TS, et al. Genome wide mRNA profiling of esophageal squamous cell carcinoma for identification of cancer biomarkers. Cancer Biol Ther. 2009; 8 (1):36–46. doi: 10.4161/cbt.8.1.7090 PMID: 18981721

23. Stanich JE, Gibbons SJ, Eisenman ST, Bardsley MR, Rock JR, Harfe BD, et al. Ano1 as a regulator of proliferation. Am J Physiol Gastrointest Liver Physiol. 2011; 301 (6):G1044–1051. doi: 10.1152/ajpgi.00196.2011 PMID: 21940901

24. Rock JR, Futtner CR, Harfe BD.The transmembrane protein TMEM16A is required for normal development of the murine trachea. Dev Biol. 2008; 321 (1):141–149. doi: 10.1016/j.ydbio.2008.06.009 PMID: 18585372

25. Rock JR, ONeal WK, Gabriel SE, Randell SH, Harfe BD, Boucher RC, et al. Transmembrane protein 16A (TMEM16A) is a Ca2+-regulated Cl- secretory channel in mouse airways. J Biol Chem. 2009; 284 (22):14875–14880. doi: 10.1074/jbc.C109.000869 PMID: 19363029

26. Ousingsawat J, Martins JR, Schreiber R, Rock JR, Harfe BD, Kunzelmann K. Loss of TMEM16A causes a defect in epithelial Ca2+-dependent chloride transport. J Biol Chem. 2009; 284 (42):28698–28703. doi: 10.1074/jbc.M109.012120 PMID: 19679661

27. Huang F, Rock JR, Harfe BD, Cheng T, Huang X, Jan YN, et al. Studies on expression and function of the TMEM16A calcium-activated chloride channel. Proc Natl Acad Sci U S A. 2009; 106 (50):21413–21418. doi: 10.1073/pnas.0911935106 PMID: 19965375

28. Gritli-Linde A, Vaziri Sani F, Rock JR, Hallberg K, Iribarne D, Harfe BD, et al. Expression patterns of the Tmem16 gene family during cephalic development in the mouse. Gene Expr Patterns. 2009; 9 (3):178–191. doi: 10.1016/j.gep.2008.11.002 PMID: 19059364

29. Cuschieri A, Bannister LH. The development of the olfactory mucosa in the mouse: light microscopy. J Anat. 1975; 119 (Pt 2):277–286. PMID: 1133096.

30. Taniguchi K, Taniguchi K. Embryonic and postnatal differentiation of olfactory epithelium and vomeronasal organ in the Syrian hamster. J Vet Med Sci Jpn Soc Vet Sci. 2008; 70 (1):57–64. doi: 10.1292/jvms.70.57 PMID: 18250573

31. Smart IH. Location and orientation of mitotic figures in the developing mouse olfactory epithelium. J Anat. 1971; 109 (Pt 2):243–251. PMID: 5558232.

32. Farbman AI. Developmental biology of olfactory sensory neurons. Semin Cell Biol. 1994; 5 (1):3–10. PMID: 8186394.

33. Wong ST, Trinh K, Hacker B, Chan GC, Lowe G, Gaggar A, et al. Disruption of the type III adenylyl cyclase gene leads to peripheral and behavioral anosmia in transgenic mice. Neuron. 2000; 27 (3):487–497. doi: 10.1016/S0896-6273(00)00060-X PMID: 11055432

34. Col JAD, Matsuo T, Storm DR, Rodriguez I. Adenylyl cyclase-dependent axonal targeting in the olfactory system. Development. 2007; 134 (13):2481–2489. doi: 10.1242/dev.006346 PMID: 17537788

35. Zou D-J, Chesler AT, Pichon CEL, Kuznetsov A, Pei X, Hwang EL, et al. Absence of Adenylyl Cyclase 3 Perturbs Peripheral Olfactory Projections in Mice. J Neurosci. 2007; 27 (25):6675–6683. doi: 10.1523/JNEUROSCI.0699-07.2007 PMID: 17581954

36. Keller A, Margolis FL. Immunological studies of the rat olfactory marker protein. J Neurochem. 1975; 24 (6):1101–1106. PMID: 805214.

37. Guo Z, Packard A, Krolewski RC, Harris MT, Manglapus GL, Schwob JE. Expression of pax6 and sox2 in adult olfactory epithelium. J Comp Neurol. 2010; 518 (21):4395–4418. doi: 10.1002/cne.22463 PMID: 20852734

38. Gokoffski KK, Wu H-H, Beites CL, Kim J, Kim EJ, Matzuk MM, et al. Activin and GDF11 collaborate in feedback control of neuroepithelial stem cell proliferation and fate. Development. 2011; 138 (19):4131–4142. doi: 10.1242/dev.065870 PMID: 21852401

39. Krolewski RC, Packard A, Jang W, Wildner H, Schwob JE. Ascl1 (Mash1) Knockout Perturbs Differentiation of Nonneuronal Cells in Olfactory Epithelium. PLoS ONE. 2012; 7 (12):e51737. doi: 10.1371/journal.pone.0051737 PMID: 23284756

40. Holbrook EH, Szumowski KE, Schwob JE. An immunochemical, ultrastructural, and developmental characterization of the horizontal basal cells of rat olfactory epithelium. J Comp Neurol. 1995; 363 (1):129–46. doi: 10.1002/cne.903630111 PMID: 8682932

41. Leung CT, Coulombe PA, Reed RR. Contribution of olfactory neural stem cells to tissue maintenance and regeneration. Nat Neurosci. 2007; 10 (6):720–726. doi: 10.1038/nn1882 PMID: 17468753

42. Ohta Y, Ichimura K. Proliferation markers, proliferating cell nuclear antigen, Ki67, 5-bromo-2'-deoxyuridine, and cyclin D1 in mouse olfactory epithelium. Ann Otol Rhinol Laryngol. 2000; 109 (11):1046–1048. PMID: 11089996.

43. Fletcher RB, Prasol MS, Estrada J, Baudhuin A, Vranizan K, Choi YG, et al. p63 regulates olfactory stem cell self-renewal and differentiation. Neuron. 2011; 72 (5):748–759. doi: 10.1016/j.neuron.2011.09.009 PMID: 22153372

44. Jang W, Chen X, Flis D, Harris M, Schwob JE. Label-retaining, quiescent globose basal cells are found in the olfactory epithelium. J Comp Neurol. 2014; 522 (4):731–749. doi: 10.1002/cne.23470 PMID: 24122672

45. Chen M, Tian S, Yang X, Lane AP, Reed RR, Liu H. Wnt-responsive Lgr5+ globose basal cells function as multipotent olfactory epithelium progenitor cells. J Neurosci. 2014; 34 (24):8268–8276. doi: 10.1523/JNEUROSCI.0240-14.2014 PMID: 24920630

46. Solbu TT, Holen T. Aquaporin pathways and mucin secretion of Bowman's glands might protect the olfactory mucosa. Chem Senses. 2012; 37 (1):35–46. doi: 10.1093/chemse/bjr063 PMID: 21745799

47. Ruppersburg CC, Hartzell HC. The Ca2+-activated Cl- channel ANO1/TMEM16A regulates primary ciliogenesis. Mol Biol Cell. 2014; 25 (11):1793–1807. doi: 10.1091/mbc.E13-10-0599 PMID: 24694595

48. Moll R, Franke WW, Schiller DL, Geiger B, Krepler R. The catalog of human cytokeratins: patterns of expression in normal epithelia, tumors and cultured cells. Cell. 1982; 31 (1):11–24. doi: 10.1016/0092-8674(82)90400-7 PMID: 6186379

49. Coulombe PA. The cellular and molecular biology of keratins: beginning a new era. Curr Opin Cell Biol. 1993; 5 (1):17–29. doi: 10.1016/S0955-0674(05)80004-3 PMID: 7680567

50. Casanova L, Bravo A, Were F, Ramírez A, Jorcano JJ, Vidal M. Tissue-specific and efficient expression of the human simple epithelial keratin 8 gene in transgenic mice. J Cell Sci. 1995; 108 (Pt 2):811–820. PMID: 7539440.

51. Franke WW, Grund C, Kuhn C, Jackson BW, Illmensee K. Formation of cytoskeletal elements during mouse embryogenesis. III. Primary mesenchymal cells and the first appearance of vimentin filaments. Differentiation. 1982; 23 (1):43–59. doi: 10.1111/j.1432-0436.1982.tb01266.x PMID: 6759279

52. Perez-Cornejo P, Gokhale A, Duran C, Cui Y, Xiao Q, Hartzell HC, et al. Anoctamin 1 (Tmem16A) Ca2+-activated chloride channel stoichiometrically interacts with an ezrin-radixin-moesin network. Proc Natl Acad Sci U S A. 2012; 109 (26):10376–10381. doi: 10.1073/pnas.1200174109 PMID: 22685202

53. Frisch D. Ultrastructure of mouse olfactory mucosa. Am J Anat. 1967; 121 (1):87–120. PMID: 6052394.

54. Drenckhahn D, Dermietzel R. Organization of the actin filament cytoskeleton in the intestinal brush border: a quantitative and qualitative immunoelectron microscope study. J Cell Biol. 1988; 107 (3):1037–1048. doi: 10.1083/jcb.107.3.1037 PMID: 3417773

55. Wanitchakool P, Wolf L, Koehl GE, Sirianant L, Schreiber R, Kulkarni S, et al. Role of anoctamins in cancer and apoptosis. Philos Trans R Soc Lond B Biol Sci. 2014; 369 (1638):20130096. doi: 10.1098/rstb.2013.0096 PMID: 24493744

56. Qu Z, Yao W, Yao R, Liu X, Yu K, Hartzell C. The Ca(2+)-activated Cl(-) channel, ANO1 (TMEM16A), is a double-edged sword in cell proliferation and tumorigenesis. Cancer Med. 2014; 3 (3):453–461. doi: 10.1002/cam4.232 PMID: 24639373

57. Mazzone A, Bernard CE, Strege PR, Beyder A, Galietta LJ, Pasricha PJ, et al. Altered expression of Ano1 variants in human diabetic gastroparesis. J Biol Chem. 2011; 286 (15):13393–13403. doi: 10.1074/jbc.M110.196089 PMID: 21349842

58. Britschgi A, Bill A, Brinkhaus H, Rothwell C, Clay I, Duss S, et al. Calcium-activated chloride channel ANO1 promotes breast cancer progression by activating EGFR and CAMK signaling. Proc Natl Acad Sci U S A. 2013; 110 (11):E1026–1034. doi: 10.1073/pnas.1217072110 PMID: 23431153

59. Ayoub C, Wasylyk C, Li Y, Thomas E, Marisa L, Robé A, et al. ANO1 amplification and expression in HNSCC with a high propensity for future distant metastasis and its functions in HNSCC cell lines. Br J Cancer. 2010; 103 (5):715–726. doi: 10.1038/sj.bjc.6605823 PMID: 20664600

60. Ruiz C, Martins JR, Rudin F, Schneider S, Dietsche T, Fischer CA, et al. Enhanced expression of ANO1 in head and neck squamous cell carcinoma causes cell migration and correlates with poor prognosis. PloS ONE. 2012; 7 (8):e43265. doi: 10.1371/journal.pone.0043265 PMID: 22912841

61. Romanenko VG, Catalán MA, Brown DA, Putzier I, Hartzell HC, Marmorstein AD, et al. Tmem16A encodes the Ca2+-activated Cl- channel in mouse submandibular salivary gland acinar cells. J Biol Chem. 2010; 285 (17):12990–13001. doi: 10.1074/jbc.M109.068544 PMID: 20177062

62. Duran C, Hartzell HC. Physiological roles and diseases of Tmem16/Anoctamin proteins: are they all chloride channels? Acta Pharmacol Sin. 2011; 32:685–692. doi: 10.1038/aps.2011.48 PMID: 21642943

63. Getchell TV, Margolis FL, Getchell ML. Perireceptor and receptor events in vertebrate olfaction. Prog Neurobiol. 1984; 23 (4):317–345. doi: 10.1016/0301-0082(84)90008-X PMID: 6398455

64. Ablimit A, Matsuzaki T, Tajika Y, Aoki T, Hagiwara H, Takata K. Immunolocalization of water channel aquaporins in the nasal olfactory mucosa. Arch Histol Cytol. 2006; 69 (1):1–12. doi: 10.1679/aohc.69.1 PMID: 16609265

3.2. Currents induced by the TMEM16A calcium-activated chloride channel in supporting cells of the mouse olfactory epithelium

Currents induced by the TMEM16A calcium-activated chloride channel in supporting cells of the mouse olfactory epithelium

Tiago Henriques[1*], Emilio Agostinelli[1*], Andres Hernandez-Clavijo[1], Devendra Kumar Maurya[1+], Jason R. Rock[2], Brian D. Harfe[3], Anna Menini[1#], Simone Pifferi[1#]

[1] Neurobiology Group, SISSA, International School for Advanced Studies, Trieste, Italy

2 Department of Anatomy, UCSF School of Medicine, San Francisco, CA, United States of America,

3 Department of Molecular Genetics and Microbiology Genetics Institute, University of Florida, College of Medicine, Gainesville, FL, United States of America

* These authors equally contributed to this work

[#] Corresponding authors

[+] Current address: Department of Molecular Biology, Umeå University, Umeå, Sweden

ABSTRACT

Here, we used whole-cell patch-clamp recordings to provide a functional characterization of currents activated by Ca^{2+} in supporting cells of neonatal mouse olfactory epithelium slices in the absence of intracellular K^+. We decreased the large leak conductance typical of supporting cells by adding the gap junction blocker 18β-glycyrrhetinic acid. The average current in 1.5 μM Ca^{2+} and symmetrical Cl^- was about 2 nA at +80 mV significantly larger than the value of about 0.5 nA measured in the absence of Ca^{2+}. Ion substitution experiments indicated that, in the presence of intracellular Cs^+ instead of K^+, Ca^{2+} activates mainly anionic currents in these cells. Intracellular Ca^{2+} was also increased by ATP stimulation and outwardly rectifying currents were measured. To determine the contribution of TMEM16A to the Ca^{2+}-activated currents we repeated the same experiments using TMEM16A knockout mice. We found that Ca^{2+}-activated currents were abolished in supporting cells of TMEM16A knockout mice, demonstrating that TMEM16A is an essential component of Ca^{2+}-activated Cl^- currents in supporting cells of the olfactory epithelium.

INTRODUCTION

The detection of odorant molecules occurs in olfactory sensory neurons located in the olfactory epithelium. The olfactory epithelium is a pseudostratified epithelium composed of olfactory sensory neurons, glial-like supporting (or sustentacular) cells, basal cells, and microvillous cells.

Olfactory sensory neurons are bipolar neurons with a single dendrite and several cilia that protrude at the apical surface into the external environment. A single axon arising from the basal part of the neuron projects to the olfactory bulb. Cilia are immersed in a protective mucus layer composed of water, ions, and proteins secreted by Bowman's glands and supporting cells (Menco and Farbman, 1992; Menco et al., 1998). Odorant molecules bind to odorant receptors in the cilia and give rise to a transduction cascade that includes the activation of cyclic-nucleotide gated channels and Ca^{2+}-activated Cl^- channels. Recent studies indicated that TMEM16B (also named anoctamin2 or ANO2) is the cilial Ca^{2+}-activated Cl^- channel, although the physiological role of this channel is still object of debate (Dibattista et al., 2017).

Supporting cells have columnar cell bodies that form a monolayer at the apical surface of the olfactory epithelium and basal processes extending to the basal lamina. Several microvilli are present on the apical side of supporting cells and are immersed in the mucus layer where they intermingle with cilia of olfactory sensory neurons. Supporting cells perform a large number of functions, some of which similar to those of glial and others typical of epithelial cells. For example, supporting cells surround and provide structural support to olfactory sensory neurons, act as phagocytes of dead cells, and are involved in the metabolism of foreign compounds mediated by cytochrome P450 and other enzymes (Breipohl et al., 1974; Chen et al., 1992; Gu et al., 1998; Ling et al., 2004; Suzuki et al., 1996; Whitby-Logan et al., 2004). Supporting cells may also be involved in the regulation of the ionic composition of the mucus layer at the apical surface of the olfactory epithelium, contributing to the maintenance of a balance between salts and water through ion and water channels. The amiloride-sensitive Na^+ channel (ENaCs) is highly expressed on microvilli of supporting cells (Menco et al., 1998). In addition, it has been suggested that the cystic fibrosis transmembrane conductance regulator, CFTR Cl^- channel and members of the aquaporin (AQP) water channel family, that are expressed in olfactory non-neuronal cells, are possibly located in supporting cells, although their localization has not been conclusively demonstrated (Ablimit et al., 2006; Grubb et al., 2007; Lu et al., 2008; Merigo et al., 2011; Pfister et al., 2015; Rochelle et al., 2000).

We and others have recently shown that the Ca^{2+}-activated Cl^- channel TMEM16A (also named anoctamin1 or ANO1) is expressed at the apical part and in microvilli of olfactory supporting cells from rats and mice (Dauner et al., 2012; Maurya and Menini, 2014; Maurya et al., 2015). However, to the best

of our knowledge, measurements of Ca^{2+}-activated Cl^- currents in olfactory supporting cells have not been reported yet. The aim of this study was to investigate the presence of functional Ca^{2+}-activated Cl^- channels in mouse olfactory supporting cells and to identify the molecular identity of the channels. We performed recordings in whole-cell from mouse supporting cells after blocking gap junctions with 18β-glycyrrhetinic acid (18β-GA) substituting intracellular K^+ with Cs^+ to avoid the contribution of Ca^{2+}-activated K^+ currents. Our results demonstrate the presence of Ca^{2+}-activated Cl^- currents and show that TMEM16A is a necessary component for the activation of this current in mouse olfactory supporting cells.

MATERIALS AND METHODS

Animals

Mice were handled in accordance with the guidelines of the Italian Animal Welfare Act and European Union guidelines on animal research, under a protocol approved by the ethic committee of SISSA. Postnatal mice P0-P4 were decapitated before nose removal. Experiments were performed on tissues from C57BL/6 mice, or from TMEM16A WT and TMEM16A KO littermate mice obtained by breeding heterozygous mice generated by Rock et al. (2008).

Immunohistochemistry

Coronal sections of the olfactory epithelium and immunohistochemistry were obtained as described previously (Maurya and Menini, 2014; Maurya et al., 2015). Briefly whole head region was fixed in 4% paraformaldehyde phosphate-buffered saline (PBS) four hours at 4℃. Tissues were equilibrated overnight at 4°C in 30% (wt/vol) sucrose and then embedded in OCT (Bio-optica, Milano, Italy) and stored at −80°C. Coronal sections 12–14 μm thick were cut with a cryostat. Before employing primary antibody, sections were incubated in blocking solution [2% FBS (vol/vol) and 0.2% (vol/vol) Triton X-100 in PBS] for 90 min. Then incubated with the primary antibody (diluted in the blocking solution) overnight at 4°C. The following primary antibodies (company, catalog number, dilution) were used: polyclonal goat anti OMP (Wako Chemicals, 544-10001, 1:1000), Mouse monoclonal acetylated tubulin (Sigma, T7451, 1:100), Rabbit polyclonal anti TMEM16A (Abcam, ab53212, 1:50). Sections were then rinsed with 0.1% (vol/vol) Tween 20 in PBS (PBS-T) and incubated with the fluorophore-

conjugated secondary antibody (diluted in PBS-T) for two hours at room temperature. Secondary antibodies used were donkey anti-rabbit Alexa 488 (A-21206, Life Technologies), donkey anti-goat Alexa 594 (A-11058, Life Technologies), and donkey anti-mouse Alexa 594 (A-21203, Life Technologies). After washing with PBS-T, sections were treated with 0.1 µg/ml DAPI for 30 min, washed with PBS-T, and mounted with Vectashield (Vector Laboratories, Burlingame, CA).

Immunoreactivity was visualized with a confocal microscope (TCS SP2; Leica). Images were acquired using Leica software (at 1,024 X 1,024–pixel resolution) and were not modified other than to balance brightness and contrast, unless otherwise specified. Images of TMEM16A immunoreactvity in dorsal epithelium was adjusted using level channels tool in Inkscape. Nuclei were stained by DAPI. Control experiments without the primary antibodies gave no signal.

Preparation of acute slices of the olfactory epithelium

Acute coronal slices of the olfactory epithelium were prepared with slight modifications of the methods previously described to obtain slices of the vomeronasal organ (Dibattista et al., 2008; Pietra et al., 2016; Shimazaki et al., 2006; Wong et al., 2018). The nose of a P0-P4 mouse was dissected en bloc and embedded in 3% Type I-A agarose prepared in artificial cerebrospinal fluid (ACSF) once the solution cooled to 38℃. ACSF contained (in mM) 120 NaCl, 25 $NaHCO_3$, 5 KCl, 1 $MgSO_4$, 1 $CaCl_2$, 10 HEPES, 10 Glucose, pH 7.4 with NaOH. Coronal slices of 300 µm thickness were cut with a vibratome (Vibratome 1000 Plus Sectioning System) and kept in cold oxygenated ACSF until use.

Whole-cell recordings from supporting cells of the olfactory epithelium

Slices were transferred to a recording chamber continuously perfused with oxygenated ACSF. Slices were viewed with an upright microscope (BX51WI; Olympus) equipped with infrared differential contrast optics, a camera (DFK 72BUC02; Imaging Source) and a 40 X water-immersion objective with an additional 2 X auxiliary lens. Extracellular solutions were exchanged or stimuli were delivered through an 8-into-1 multi-barrel perfusion pencil connected to a ValveLink8.2 pinch valve perfusion system (Automate Scientific, Berkeley, CA, USA).

Supporting cells were identified by their morphology and whole-cell experiments were obtained by patching the apical part of supporting cells. Fluorescein (10 µg/ml) dissolved in the pipette solution diffused into the cell and allowed visualization under blue light of the fluorescence image of the cell (Fig. 2 A). Patch pipettes were pulled from borosilicate capillaries (WPI) with a Narishige PC-10 puller and had resistances of 3-5 MΩ when filled with intracellular solution. Electrophysiological recordings were obtained using a MultiClamp 700B amplifier controlled by Clampex 10.6 via a Digidata 1550A

(Molecular Devices). Data were low-pass filtered at 2 kHz and sampled at 10 kHz. Experiments were performed at room temperature (20–25 °C).

The extracellular Ringer's solution contained (in mM): 140 NaCl, 5 KCl, 2 $CaCl_2$, 1 $MgCl_2$, 10 HEPES, 10 glucose, pH 7.4. For ionic selectivity experiments, NaCl in the extracellular Ringer's solution was omitted and 250 mM sucrose was added to maintain the osmolarity. We used various intracellular solutions filling the patch pipette according to the type of experiment. For recordings of voltage-gated currents, the pipette solution contained (in mM): 145 KCl, 4 $MgCl_2$, 11 EGTA, and 10 HEPES, adjusted to pH 7.2 with KOH. For recordings of Ca^{2+}-activated currents, the intracellular solutions contained (in mM): 140 CsCl, 10 HEDTA, and 10 HEPES, adjusted to pH 7.2 with CsOH, and no added Ca^{2+} for the nominally 0 Ca^{2+} solution, or 3.209 mM to obtain 1.5 μM free Ca^{2+} as described previously (Patton et al., 2004; Pifferi et al., 2006, 2009; Amjad et al. 2015). For recordings of ATP-activated currents, the pipette solution contained (in mM): 140 CsCl, 2 HEDTA, and 10 HEPES, adjusted to pH 7.2 with CsOH.

For experiment with ATP the current-voltage relation was measured using a ramp protocol from -80 mV to +80 mV at 0.16 mV/ms.

The bath was grounded via a 3 M KCl agar bridge connected to an Ag/AgCl reference electrode. Liquid junction potentials calculated using pClamp 10.6 (based on Barry, 1994)) were less than 4 mV and applied voltages were not corrected.

The following chemicals were prepared as stock solutions as indicated and diluted to the final concentration in the bathing solution on the day of the experiment: 100 mM 18β-glycyrrhetinic acid (18β-GA) in ethanol, 30 mM ATP in Ringer's solution, stored at -20 °C; 1 mM Ani9 in dimethyl sulfoxide (DMSO), stored at +4 °C.

All chemicals were purchased from Sigma, unless otherwise specified.

Analysis of electrophysiological data

IGOR Pro software (WaveMetrics) was used for data analysis and to produce the figures. Data are presented as mean ± SEM and the number of cells (n). In the box plots the lines represent the median, the upper and lower box boundaries represent the 25^{th} and 75^{th} percentile, and upper and lower whiskers represent the 10^{th} and 90^{th} percentiles. Statistical analyses of normally distributed data (Jarque-Bera test), were performed using t-test, one sample t-test, or one-way ANOVA with Tukey test. For not normally distributed data, the Wilcoxon-Mann-Whitney's test (U-test) was used. P-values of <0.05 were considered statistically significant.

RESULTS

TMEM16A expression in olfactory supporting cells

We and others have previously reported that the Ca^{2+}-activated Cl^- channel TMEM16A is expressed in the olfactory epithelium, where it localizes at the apical part of supporting cells and in their microvilli (Dauner et al., 2012; Maurya and Menini, 2014; Maurya et al., 2015). Figure 1A shows a schematic diagram of a nose coronal section illustrating the localization of the olfactory and respiratory epithelia, and Figure 1B illustrates the organization of the olfactory epithelium mainly composed by supporting cells, olfactory sensory neurons, and basal cells. Figures 1C shows that, in agreement with our previous results, a strong immunoreactivity for TMEM16A was present at the apical surface of a ventral region of the olfactory epithelium near the transition zone with the respiratory epithelium of neonatal mice (Fig. 1C). To visualize olfactory neurons, we used the olfactory marker protein (OMP), a typical marker for mature olfactory sensory neurons (Keller and Margolis, 1975), while cilia of olfactory neurons were identified with acetylated tubulin, a canonical marker for cilia. TMEM16A was strongly expressed at the apical surface of the olfactory epithelium, and did not overlap with acetylated tubulin, which stained cilia in a layer directly above the layer stained by TMEM16A. Maurya and Menini (2014; Fig. 4C) have shown that in neonatal mice the apical immunoreactivity for TMEM16A is not uniform and decreases until it is not visible anymore toward the dorsal zone. Fig. 1D shows the absence of immunoreactivity for TMEM16A in the dorsal zone. However, when the intensity of the signal was digitally enhanced, a weak staining for TMEM16A was revealed, as shown in Fig. 1D. These results confirm and extend previous data showing that TMEM16A is highly expressed in the region near the transition zone with the respiratory epithelium (Fig.1C), while it is poorly expressed in the dorsal zone (Fig. 1D). As previously reported, TMEM16A localized in the apical portion of the supporting cells in the proximal portion of the microvilli (Fig 1 B-D, Maurya and Menini, 2014; Maurya et al., 2015).

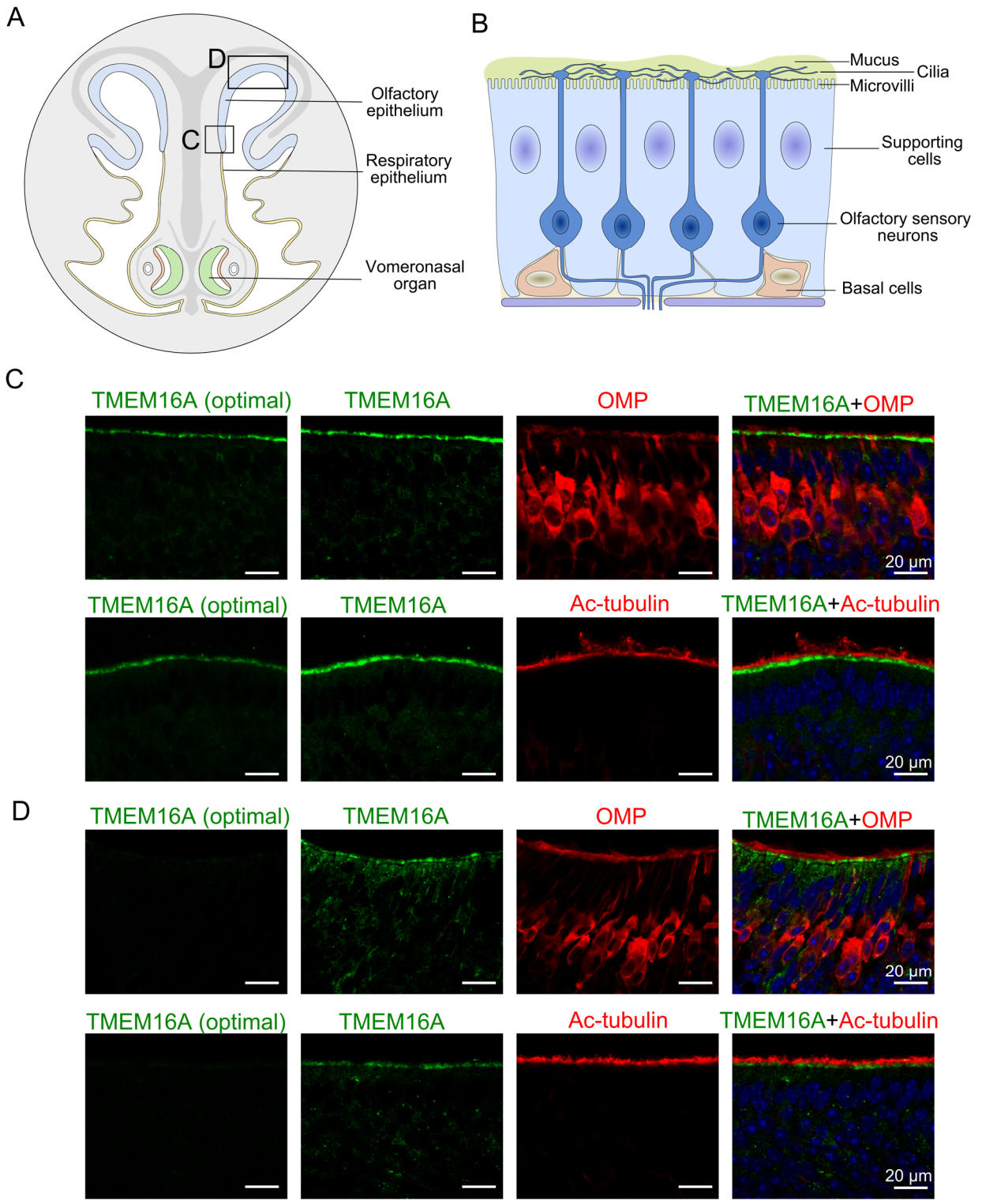

Figure 1. TMEM16A expression in the olfactory epithelium. (A) Schematic drawing of a nose coronal section showing the olfactory epithelium, respiratory epithelium and vomeronasal organ. (B) The olfactory epithelium is composed of supporting cells, olfactory sensory neurons and basal cells. Confocal micrographs of coronal sections of the olfactory epithelium from an area near the transition zone with the respiratory epithelium (C) or from the dorsal zone (D). Cell nuclei were stained by DAPI.

Whole-cell recordings from supporting cells

Whole-cell recordings were obtained from supporting cells at the apical surface of neonatal mouse olfactory epithelium slices. Fluorescein was included in the intracellular solution filling the patch pipette and diffused inside the cell after rupturing the membrane to obtain the whole-cell configuration. The fluorescence image in Fig. 2A reveals the typical morphology of a supporting cell, with the cell body located in the apical region and processes extending towards the basal part of the epithelium. In this study we only analyzed recordings from supporting cells clearly identified by their morphology.

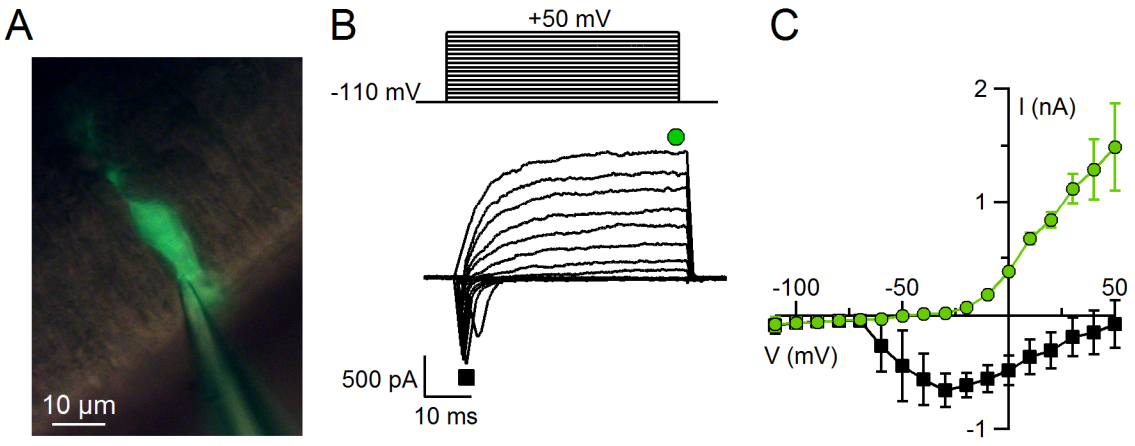

Figure 2. Voltage-gated currents in olfactory supporting cells. (A) Fluorescence micrograph of a supporting cell filled with fluorescein through the patch pipette. (B) Representative whole-cell currents recorded using the voltage protocol indicated at the top of the panel. The holding potential was -110 mV and voltage steps in 10 mV increments were applied up to +50 mV. Leak currents were subtracted using the P/4 protocol. (C) Plot of average ± SEM amplitudes of inward and outward currents versus the test potential (n=3).

We first analyzed some basic electrophysiological properties. Passive membrane properties of supporting cells in the presence of KCl in the pipette had the following values: mean resting potential -41 ± 1 mV (n =18), input resistance 261 ± 88 MΩ (n = 11), and capacitance 17 ±1 pF (n = 17).

Next, we investigated the presence of voltage-gated currents. As supporting cells have very large leak currents, as we will describe in Figure 3, voltage-gated currents could only be revealed after

subtraction of the leak currents. Figure 2B shows representative voltage-gated currents from a supporting cell obtained after subtraction of leak currents using the P/4 protocol. The intracellular solution filling the patch pipette contained KCl and currents were activated by depolarizing voltage steps up to +50 mV from a holding potential of –110 mV. Voltage steps more positive than about -60 mV elicited transient inward currents followed by outward currents. Average current–voltage relations measured at the peak of the inward currents or at the end of the sustained outward currents are shown in Figure 2C. These results are largely similar to those previously reported by Vogalis et al. (2005) who showed that inward and outward currents were mainly due to voltage-gated Na^+ and K^+ channels, respectively.

The same authors also reported that supporting cells have a large leak conductance that is decreased by the addition of the gap junction blocker 18β-GA (Vogalis et al., 2005). Figure 3 A shows large leak currents activated by voltage steps between -80 and +80 mV from a holding potential of 0 mV with an intracellular solution containing CsCl. In extracellular Ringer's solution, the average current was -687 ± 206 pA at -80 mV and 3678 ± 1065 pA at +80 mV (n = 4). When slices were pretreated for about 1 h with 20 µM 18β-GA, currents were significantly reduced to -174 ± 18 pA at -80 mV and 459 ± 54 pA at +80 mV (n =17, $p<0.001$ unpaired U-test) showing that 18β-GA partially blocks the leak currents (Fig. 3B). Thus, all the subsequent experiments were performed after pretreatment with 18β-GA.

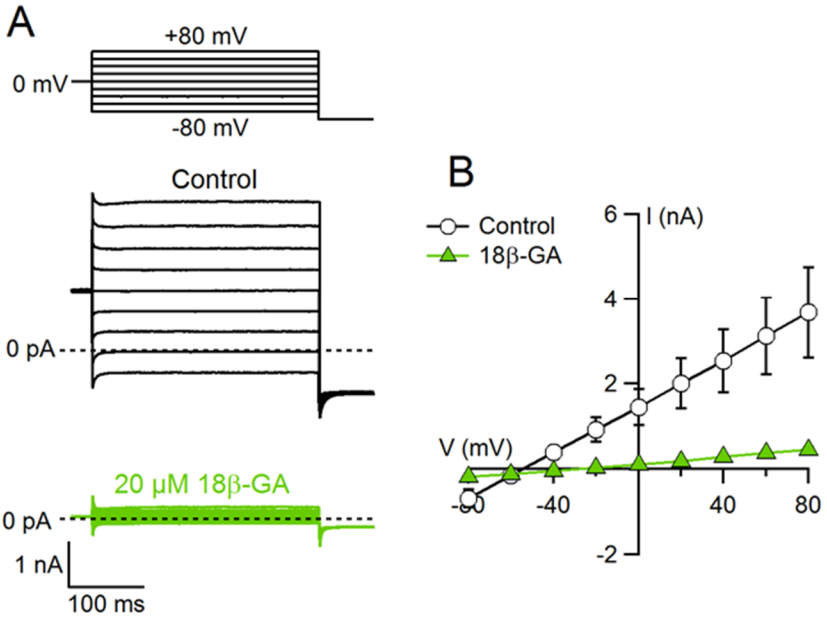

Figure 3. **Leak current block by the gap junction inhibitor 18β-GA.** (A) Representative whole-cell currents recorded from two different supporting cells in control condition (black traces) and after pre-incubation with 20 µM 18β-GA (green traces). The holding potential was 0 mV and voltage steps from -80 mV to +80 mV with 20 mV increments were applied as indicated at the top of the panel. (C) Plot of average ± SEM current amplitudes measured at the end of voltage pulses versus the test potential from cells in control condition (white circles) and after pre-incubation with 20 µM 18β-GA (green triangles; n=4-17).

Ca^{2+}-activated Cl^- currents in supporting cells of the mouse olfactory epithelium

To investigate whether a Cl^- current could be activated by Ca^{2+} in supporting cells, we compared currents measured with intracellular solutions containing nominally 0 Ca^{2+} or 1.5 µM Ca^{2+}. To avoid contributions from Ca^{2+}-activated K^+ currents, the intracellular monovalent cation was Cs^+ and to reduce leak currents slices were pre-incubated with 20 µM 18β-GA.

We first recorded from supporting cells located in a region of the olfactory epithelium near the transition zone with the respiratory epithelium, as we have previously shown that supporting cells in this area display a strong immunoreactivity for the Ca^{2+}-activated Cl^- channel TMEM16A (Fig. 1C).

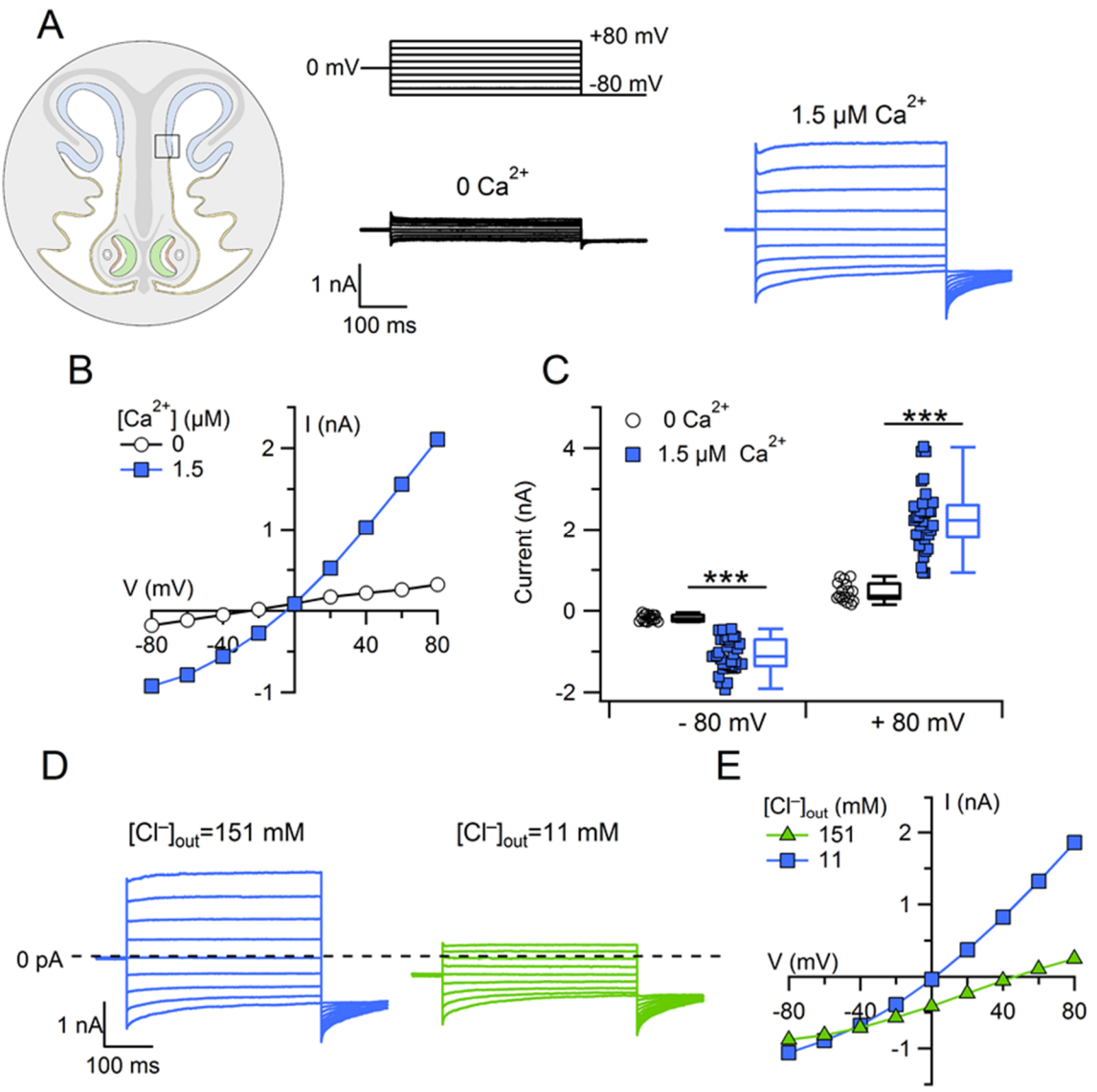

Figure 4. Ca^{2+}-activated Cl^- currents in supporting cells from a region of the olfactory epithelium near the transition zone with the respiratory epithelium. (A) Representative whole-cell currents recorded from two different supporting cells with pipette solutions containing 0 or 1.5 µM Ca^{2+}, as indicated. The holding potential was 0 mV and voltage steps from -80 mV to +80 mV with 20 mV increments, followed by a step to -80 mV, were applied as indicated at the top of the panel. (B) Current amplitudes measured at the end of voltage pulses versus the test potential from the cells shown in (A). (C) Box plot and scatter dot plot showing current amplitudes measured at -80 or +80 mV with intracellular solutions containing 0 (black) or 1.5 µM Ca^{2+} (blue; n=17-35, *** $p<0.001$ unpaired t-test). (D) Representative whole-cell currents recorded from a supporting cell with pipette solution containing 1.5 µM Ca^{2+} exposed to extracellular Ringer's solution with (blue) or without (green) NaCl. The total

concentration of extracellular Cl^- was 151 mM (blue) or 11 mM (green). (E) Current amplitudes measured at the end of voltage pulses versus the test potential from the cell shown in (D).

Figure 4 shows that voltage steps between -80 and +80 mV from a holding voltage of 0 mV elicited large currents in the presence of 1.5 μM Ca^{2+} (2268 ± 137 pA at +80 mV, n = 33) and comparatively smaller currents in the presence of nominally 0 Ca^{2+} (459 ± 54 pA at +80 mV, n = 17). The activation of the current by voltage steps in the presence of 1.5 μM Ca^{2+} was time-dependent, with an instantaneous component followed by relaxation (Fig. 4 A, blue traces). For example, at +80 mV the instantaneous outward current was followed by a small additional outward relaxation, while at -80 mV the instantaneous inward current was followed by a more pronounced relaxation toward less negative values. The I-V relation measured at the end of the voltage pulses in the presence of 1.5 μM Ca^{2+} were outwardly rectifying (Fig. 4 B-C) with an average current amplitude of 2268 ± 137 pA at +80 mV and -1083 ± 69 pA at -80 mV (n = 33). Both the time-dependence of current activation by voltage and the outward rectification of the I-V relation at Ca^{2+} concentrations below values producing the maximal current amplitude, are typical hallmarks of Ca^{2+}-activated Cl^- channels, suggesting that this type of channels is responsible for the measured currents.

To further investigate the identity of these channels, we examined their ionic selectivity by replacing NaCl in the extracellular Ringer's solution with sucrose, thus reducing the concentration of Na^+ from 140 to 0 mM, and Cl^- from 151 to 11 mM (Fig. 4D, E). In the presence of low extracellular Cl^-, the reversal potential of the calcium-activated current shifted toward positive values, as expected for Cl^- selective channels in our ionic conditions, with an average shift of reversal potential of +26 ± 4 mV (n = 7). Thus, the electrophysiological characteristics of Ca^{2+}-activated currents measured in supporting cells are consistent with the expression of Ca^{2+}-activated Cl^- channels.

As Figure 1D revealed that a weak immunoreactivity for TMEM16A was present also in supporting cells from the dorsal zone of the olfactory epithelium, we performed some additional recordings in supporting cells located in portion of the tissue. The average current in 0 Ca^{2+} at +80 mV was +459 ± 53 pA (n=8). As shown in Fig. 5A, recordings from some cells in the presence of 1.5 μM Ca^{2+} did not display the typical features of Ca^{2+}-activated Cl^- currents. We classified a current as Ca^{2+}-activated when both a clear time-dependent component at +80 mV and a tail current after repolarization at -80 mV were present. Based on this classification, we identified two populations of supporting cells in the dorsal zone of the olfactory epithelium. One population of cells (n=8) did not display a significant Ca^{2+}-activated current, whereas the other population had an average value of +1316 ± 148 pA (n=16) at

+80 mV for the Ca^{2+}-activated current. For these cells, the average shift of reversal potential upon reduction of extracellular Cl^- by replacement of NaCl with sucrose was +29 ± 4 mV (n = 6), indicating a higher permeability for Cl^- than for Na^+. Thus, about 65% of the supporting cells (16 out of 24) had a Ca^{2+}-activated Cl^- current. However, the current amplitude of Ca^{2+}-activated current in the supporting cells from the dorsal olfactory epithelium was significantly smaller than that measured in cells from the transition zone with the respiratory epithelium (Fig. 5C, Tukey test after one way ANOVA), confirming the lower expression of TMEM16A observed in immunohistochemistry.

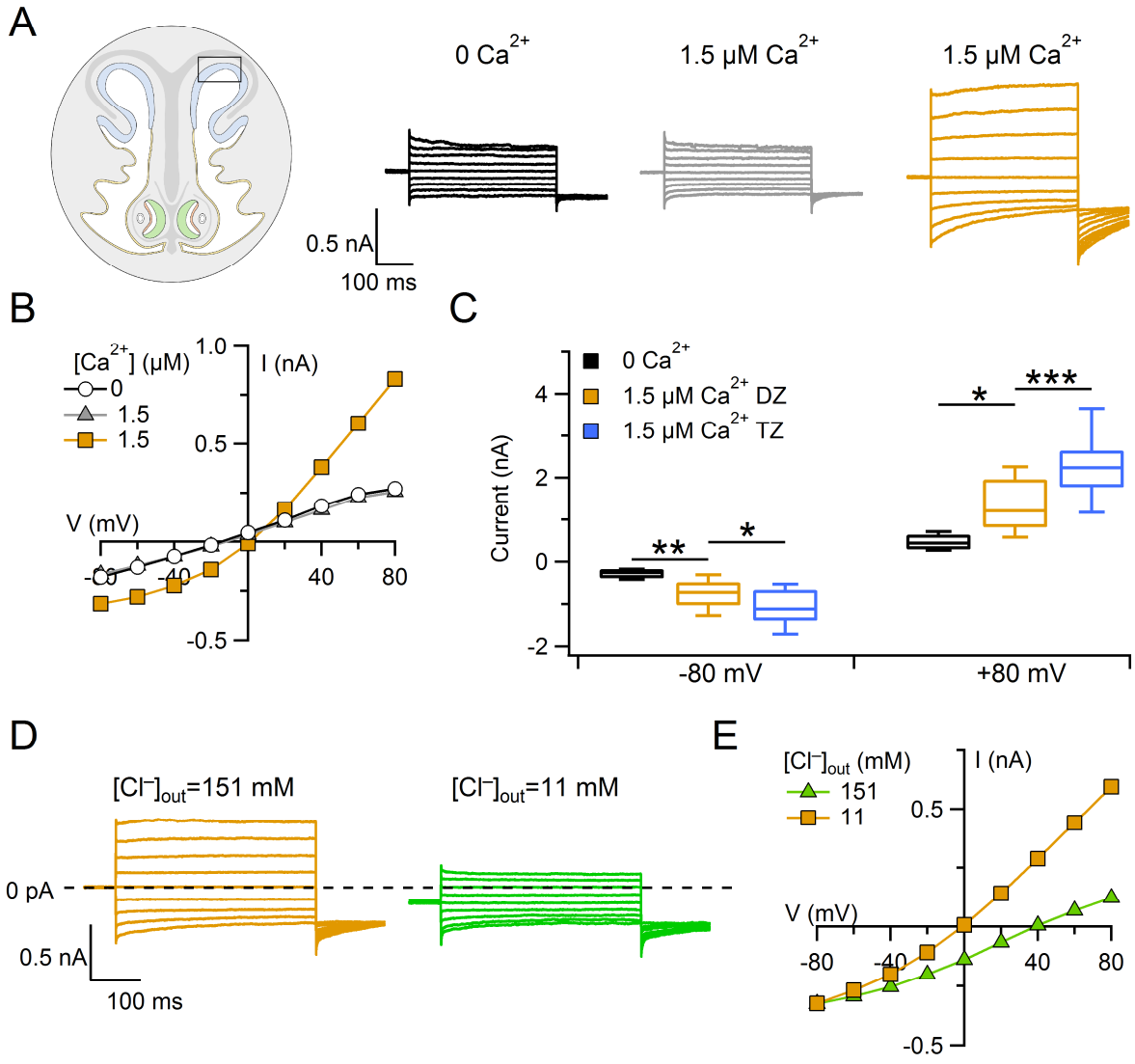

Figure 5. **Ca^{2+}-activated chloride current in SC from dorsal olfactory epithelium.**

(A) Representative whole-cell currents recorded from different supporting cells with pipette solution containing the indicated [Ca^{2+}]. The holding potential was 0 mV and voltage steps from -80 mV to +80 mV with 20 mV increments, followed by a step to -80 mV, were applied. (B) Amplitudes of the currents

measured at the end of voltage pulses versus the test potential from the cells shown in (A). (C) Box plot showing the amplitude current measured at -80 and +80 mV with the indicated $[Ca^{2+}]_i$ in the dorsal or transition zones. (n=8-35*p<0.05, **p<0.01,***p<0.001 Tukey test after one way ANOVA). (D) Representative whole-cell currents recorded from a supporting cell with pipette solution containing 1.5 µM Ca^{2+} exposed to extracellular Ringer's solution with (orange) or without (green) NaCl. The total concentration of extracellular Cl^- was 151 mM (orange) or 11 mM (green). (E) Current amplitudes measured at the end of voltage pulses versus the test potential from the cell shown in (D)

Recently, Seo et al.(2016) identified Ani9 as a potent selective blocker for TMEM16A. We therefore measured the extracellular blockage properties of 1 µM Ani9 over the Ca^{2+}-activated Cl^- currents in supporting cells. Figure 6A-C show that Ani9 reduced current amplitudes activated by 1.5 µM Ca^{2+} of 62 ± 3 % at +80 mV and 61 ± 3 % at -80 mV (n = 10, p<0.001 One sample t-test), inducing a significant block of the current. The blockage by Ani9 supports the hypothesis that the measured Ca^{2+}-activated Cl^- currents are mediated by TMEM16A.

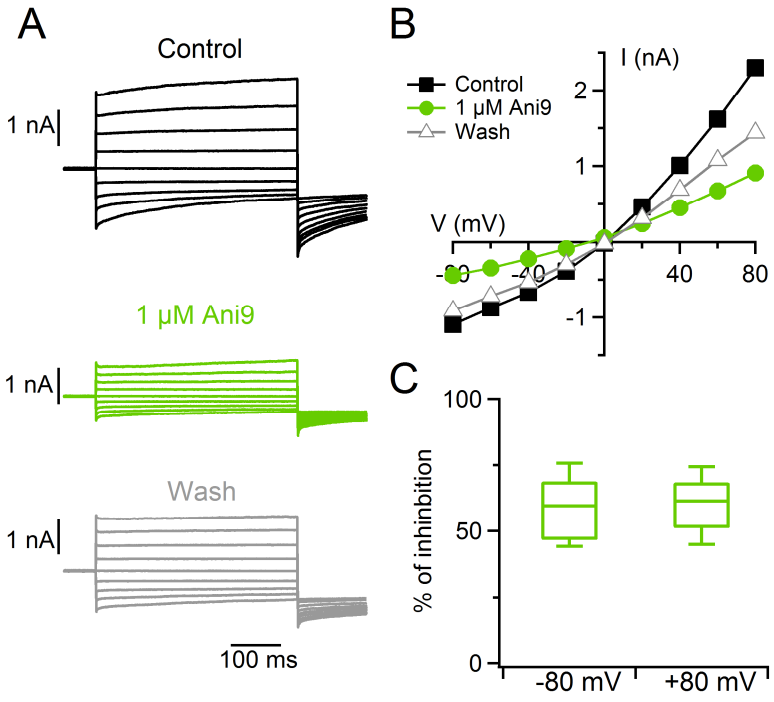

Figure 6. Ca^{2+}-activated currents in supporting cells are blocked by the TMEM16A inhibitor Ani9. (A) Representative whole-cell recordings obtained with an intracellular solution containing 1.5 µM Ca^{2+}. Voltage protocol as in Fig. 4A. The cell was exposed to a Ringer's solution (black), to 1 µM Ani9 (green), and washed in Ringer's solution (grey). (B) I-V relationships measured at the end of the voltage steps

from the recordings shown in (A). (C) Box plot of the percentage of current inhibition measured at -80 and +80 mV (n=11).

To determine the contribution of TMEM16A to Ca^{2+}-activated Cl^- currents in supporting cells, we compared currents from TMEM16A WT and KO mice (Rock et al., 2008). Figure 7A shows the comparison between representative recordings from supporting cells near the transition zone with the respiratory epithelium from TMEM16A WT (black and blue traces) or KO (orange and red traces) mice. Figure 7B shows that current amplitudes at -80 and +80 mV in the presence of 1.5 µM Ca^{2+} from TMEM16A KO mice (red) were not significantly different from currents measured in the absence of Ca^{2+} (orange; $p>0.05$ Tukey test after one-way ANOVA), showing the absence of Ca^{2+}-activated currents in TMEM16A KO mice. Similar experiments were performed also in supporting cells in the dorsal zone and yielded similar results. These data demonstrate that TMEM16A is a necessary component of the Ca^{2+}-activated Cl^- currents in supporting cells of the olfactory epithelium.

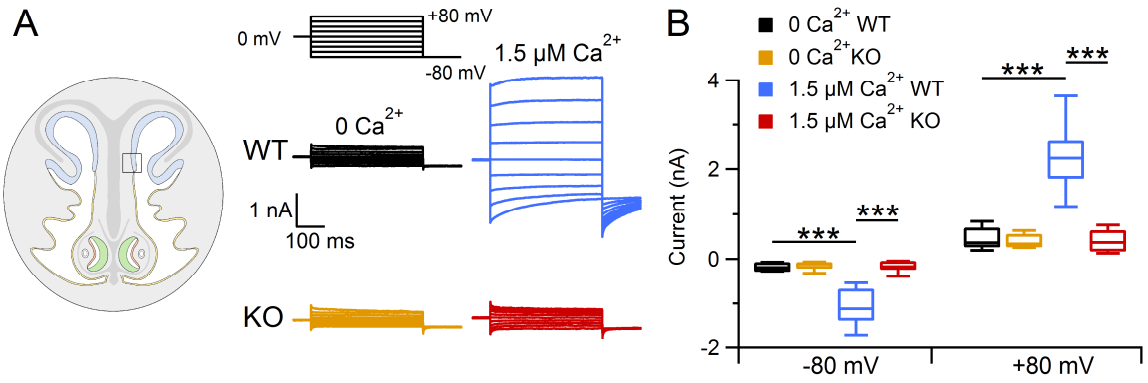

Figure 7. Lack of Ca^{2+}-activated currents is supporting cells from TMEM16A KO mice. (A) Representative whole-cell recordings obtained with pipette solutions containing 0 or 1.5 µM Ca^{2+}, as indicated. The voltage protocol is reported at the top of the panel. (B) Box plot showing current amplitudes measured at -80 and +80 mV with intracellular solutions containing 0 or 1.5 µM Ca^{2+} from WT or TMEM16A KO mice (n=8-33, ***$p<0.001$ Tukey test after one way ANOVA). Recordings were obtained from supporting cells located close to the transition zone with the respiratory epithelium.

ATP activates TMEM16A-dependent currents in supporting cells

In physiological conditions, Ca^{2+}-activated Cl^- channels are activated by an increase in intracellular Ca^{2+} due either to Ca^{2+} influx through ion channels or to Ca^{2+} release from intracellular stores. Ca^{2+} imaging experiments in olfactory supporting cells have previously shown that a transient increase in intracellular Ca^{2+} was elicited by extracellular ATP through activation of G protein coupled P2Y receptors and Ca^{2+} release from intracellular stores (Czesnik et al., 2006; Hassenklöver et al., 2008; Hegg et al., 2009, 2009). Thus, instead of increasing the Ca^{2+} concentration inside a supporting cell through constant diffusion of Ca^{2+} from the patch pipette, we sought to investigate whether a physiological transient Ca^{2+} increase induced by ATP stimulation could activate the Ca^{2+}-activated Cl^- channel TMEM16A. As in most of our previous recordings, also in this set of experiments the intracellular monovalent cation was Cs^+ instead of K^+ to avoid activation of K^+ channels and slices were pre-incubated with 20 µM 18β-GA to partially block the leak current. In addition, we lowered the intracellular concentration of HEDTA from 10 to 2 mM to reduce Ca^{2+} buffering that could decrease the ATP-induced intracellular Ca^{2+} increase.

Figure 8A shows that the application of 30 µM ATP at the holding potential of -80 mV induced a large inward current that slowly recovered to baseline (black trace). Current-voltage relations were obtained with voltage ramps from −80 to +80 mV before, during, and after the response to 30 µM ATP (Fig. 8B). The current-voltage relation measured close to the peak of the response to ATP (indicated as b in Fig. 8B) showed an outward rectification, resembling the outward rectification of the Ca^{2+}-activated Cl^- current measured with 1.5 µM Ca^{2+} in the pipette (Fig. 4B).

To determine the contribution of TMEM16A to the ATP-induced current, we recorded responses to ATP in supporting cells from TMEM16A KO mice (Fig. 8A, orange trace). Our experiments show that the average peak inward current induced by ATP in WT mice at -80 mV (-438 ± 94 pA; n = 28) was significantly reduced to -6 ± 10 pA, (n = 16, U-test) in TMEM16A KO mice (Fig. 8C).

These results indicate that the transient Ca^{2+} increase elicited by 30 µM ATP activates a TMEM16A-dependent current in supporting cells of the olfactory epithelium.

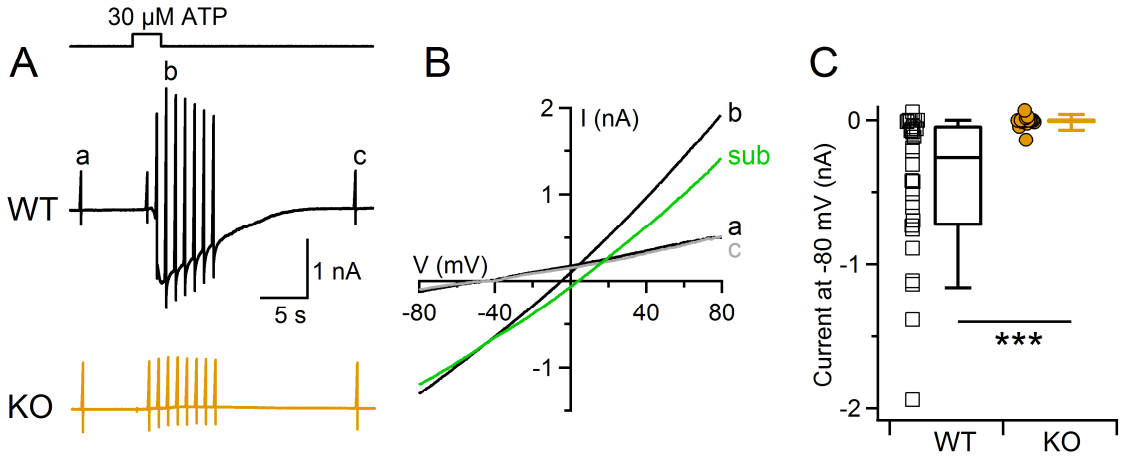

Figure 8. ATP activates a TMEM16A-dependent current in supporting cells. (A) Whole-cell currents activated by 30 µM ATP from supporting cells located close to the transition zone with the respiratory epithelium from WT (black trace) or TMEM16A KO (orange trace) mice. ATP was applied for the time indicated in the upper trace. The holding potential was -80 mV and voltage ramps from -80 to +80 mV before (a), during (b), and after (c) the ATP response were used to measure the I-V relations. (B) I-V relations from the WT cell shown in A. The green trace (sub) was obtained by subtracting the average between traces (a) and (c) from the trace in the presence of ATP (b). (C) Box plot showing the peak amplitude of ATP-activated currents measured at -80 mV (n=16-28, ***p<0.001 U-test).

REFERENCES

Ablimit, A., Matsuzaki, T., Tajika, Y., Aoki, T., Hagiwara, H., and Takata, K. (2006). Immunolocalization of water channel aquaporins in the nasal olfactory mucosa. Arch. Histol. Cytol. *69*, 1–12.

Barry, P.H. (1994). JPCalc, a software package for calculating liquid junction potential corrections in patch-clamp, intracellular, epithelial and bilayer measurements and for correcting junction potential measurements. J. Neurosci. Methods *51*, 107–116.

Breipohl, W., Laugwitz, H.J., and Bornfeld, N. (1974). Topological relations between the dendrites of olfactory sensory cells and sustentacular cells in different vertebrates. An ultrastructural study. J. Anat. *117*, 89–94.

Chen, Y., Getchell, M.L., Ding, X., and Getchell, T.V. (1992). Immunolocalization of two cytochrome P450 isozymes in rat nasal chemosensory tissue. Neuroreport *3*, 749–752.

Czesnik, D., Kuduz, J., Schild, D., and Manzini, I. (2006). ATP activates both receptor and sustentacular supporting cells in the olfactory epithelium of Xenopus laevis tadpoles. Eur. J. Neurosci. *23*, 119–128.

Dauner, K., Lissmann, J., Jeridi, S., Frings, S., and Möhrlen, F. (2012). Expression patterns of anoctamin 1 and anoctamin 2 chloride channels in the mammalian nose. Cell Tissue Res. *347*, 327–341.

Dibattista, M., Mazzatenta, A., Grassi, F., Tirindelli, R., and Menini, A. (2008). Hyperpolarization-activated cyclic nucleotide-gated channels in mouse vomeronasal sensory neurons. J. Neurophysiol. *100*, 576–586.

Dibattista, M., Pifferi, S., Boccaccio, A., Menini, A., and Reisert, J. (2017). The long tale of the calcium activated Cl- channels in olfactory transduction. Channels Austin Tex *11*, 399–414.

Grubb, B.R., Rogers, T.D., Kulaga, H.M., Burns, K.A., Wonsetler, R.L., Reed, R.R., and Ostrowski, L.E. (2007). Olfactory epithelia exhibit progressive functional and morphological defects in CF mice. Am. J. Physiol. Cell Physiol. *293*, C574-583.

Gu, J., Zhang, Q.Y., Genter, M.B., Lipinskas, T.W., Negishi, M., Nebert, D.W., and Ding, X. (1998). Purification and characterization of heterologously expressed mouse CYP2A5 and CYP2G1: role in metabolic activation of acetaminophen and 2,6-dichlorobenzonitrile in mouse olfactory mucosal microsomes. J. Pharmacol. Exp. Ther. *285*, 1287–1295.

Hassenklöver, T., Kurtanska, S., Bartoszek, I., Junek, S., Schild, D., and Manzini, I. (2008). Nucleotide-induced Ca2+ signaling in sustentacular supporting cells of the olfactory epithelium. Glia *56*, 1614–1624.

Hegg, C.C., Irwin, M., and Lucero, M.T. (2009). Calcium store-mediated signaling in sustentacular cells of the mouse olfactory epithelium. Glia *57*, 634–644.

Keller, A., and Margolis, F.L. (1975). Immunological studies of the rat olfactory marker protein. J. Neurochem. *24*, 1101–1106.

Ling, G., Gu, J., Genter, M.B., Zhuo, X., and Ding, X. (2004). Regulation of cytochrome P450 gene expression in the olfactory mucosa. Chem. Biol. Interact. *147*, 247–258.

Lu, D.C., Zhang, H., Zador, Z., and Verkman, A.S. (2008). Impaired olfaction in mice lacking aquaporin-4 water channels. FASEB J. Off. Publ. Fed. Am. Soc. Exp. Biol. *22*, 3216–3223.

Maurya, D.K., and Menini, A. (2014). Developmental expression of the calcium-activated chloride channels TMEM16A and TMEM16B in the mouse olfactory epithelium. Dev. Neurobiol. *74*, 657–675.

Maurya, D.K., Henriques, T., Marini, M., Pedemonte, N., Galietta, L.J.V., Rock, J.R., Harfe, B.D., and Menini, A. (2015). Development of the Olfactory Epithelium and Nasal Glands in TMEM16A-/- and TMEM16A+/+ Mice. PloS One *10*, e0129171.

Menco, B.P., and Farbman, A.I. (1992). Ultrastructural evidence for multiple mucous domains in frog olfactory epithelium. Cell Tissue Res. *270*, 47–56.

Menco, B.P., Birrell, G.B., Fuller, C.M., Ezeh, P.I., Keeton, D.A., and Benos, D.J. (1998). Ultrastructural localization of amiloride-sensitive sodium channels and Na+,K(+)-ATPase in the rat's olfactory epithelial surface. Chem. Senses *23*, 137–149.

Merigo, F., Mucignat-Caretta, C., Cristofoletti, M., and Zancanaro, C. (2011). Epithelial membrane transporters expression in the developing to adult mouse vomeronasal organ and olfactory mucosa. Dev. Neurobiol. *71*, 854–869.

Pfister, S., Weber, T., Härtig, W., Schwerdel, C., Elsaesser, R., Knuesel, I., and Fritschy, J.-M. (2015). Novel role of cystic fibrosis transmembrane conductance regulator in maintaining adult mouse olfactory neuronal homeostasis. J. Comp. Neurol. *523*, 406–430.

Pietra, G., Dibattista, M., Menini, A., Reisert, J., and Boccaccio, A. (2016). The Ca2+-activated Cl- channel TMEM16B regulates action potential firing and axonal targeting in olfactory sensory neurons. J. Gen. Physiol. *148*, 293–311.

Rochelle, L.G., Li, D.C., Ye, H., Lee, E., Talbot, C.R., and Boucher, R.C. (2000). Distribution of ion transport mRNAs throughout murine nose and lung. Am. J. Physiol. Lung Cell. Mol. Physiol. *279*, L14-24.

Rock, J.R., Futtner, C.R., and Harfe, B.D. (2008). The transmembrane protein TMEM16A is required for normal development of the murine trachea. Dev. Biol. *321*, 141–149.

Seo, Y., Lee, H.K., Park, J., Jeon, D.-K., Jo, S., Jo, M., and Namkung, W. (2016). Ani9, A Novel Potent Small-Molecule ANO1 Inhibitor with Negligible Effect on ANO2. PloS One *11*, e0155771.

Shimazaki, R., Boccaccio, A., Mazzatenta, A., Pinato, G., Migliore, M., and Menini, A. (2006). Electrophysiological properties and modeling of murine vomeronasal sensory neurons in acute slice preparations. Chem. Senses *31*, 425–435.

Suzuki, Y., Takeda, M., and Farbman, A.I. (1996). Supporting cells as phagocytes in the olfactory epithelium after bulbectomy. J. Comp. Neurol. *376*, 509–517.

Vogalis, F., Hegg, C.C., and Lucero, M.T. (2005). Ionic conductances in sustentacular cells of the mouse olfactory epithelium. J. Physiol. *562*, 785–799.

Whitby-Logan, G.K., Weech, M., and Walters, E. (2004). Zonal expression and activity of glutathione S-transferase enzymes in the mouse olfactory mucosa. Brain Res. *995*, 151–157.

Wong, W.M., Nagel, M., Hernandez-Clavijo, A., Pifferi, S., Menini, A., Spehr, M., and Meeks, J.P. (2018). Sensory Adaptation to Chemical Cues by Vomeronasal Sensory Neurons. ENeuro *5*.

3.3. Purinergic receptor-induced Ca^{2+} signaling in the supporting cells of mouse vomeronasal organ

Purinergic receptor-induced Ca^{2+} signaling in the supporting cells of the mouse vomeronasal organ.

Tiago Henriques*, Andres Hernandez-Clavijo*, Anna Menini and Simone Pifferi

Neurobiology Group, SISSA, International School for Advanced Studies, Trieste, Italy

* These authors equally contributed to this work

MATERIALS AND METHODS

Preparation of acute VNO slices

Experiments were performed on two months old male C57BL/6 mice. All animal procedures were carried out in accordance with the guidelines of the Italian Animal Welfare Act and European Union guidelines on animal research under a protocol approved by the ethic committee of SISSA. VNO slices were prepared as previously described with small modifications (Shimazaki et al., 2006). Briefly, after VNO dissection, all cartilaginous tissues were removed and the two halves of VNO were separately embedded in 3% Type I-A agarose prepared in artificial cerebrospinal fluid (ACSF) solution once the solution cooled to 38℃. Coronal slices of 200 µm thickness were cut with a vibratome (Vibratome 1000 Plus Sectioning System) and kept in cold oxygenated ACSF until use. ACSF contained (in mM) 120 NaCl, 20 $NaHCO_3$, 3mM KCl, 2 mM $CaCl_2$, 1 mM $MgSO_4$, 10 mM HEPES, and10 mM glucose adjusted at pH 7.4 with NaOH.

Confocal calcium imaging

Slices were loaded with 20 µM Cal-520AM (Santa Cruz Biotechnologies) for 90 minutes at room temperature in ASCF. To help dye uptake, Pluronic F-127 was added at final concentration of 0.2 mg/ml. After wash, the slices

were kept in ACSF solution until use. Stock solution of Cal-520AM was prepared in dimethyl sulfoxide (DMSO) at 2 mM and stored at -20℃. Pluronic F-127 was weekly dissolved in DMSO at 200 mg/ml concentration. A gravity-driven multivalve perfusion system (Automate Scientific) was used to deliver the stimuli.

An inverted Nikon A1R confocal microscope was used for data acquisition with 60X oil-immersion objective (NA 1.4) through the NIS Element software (Nikon). Cal-520 fluorescence was excited using a krypton-argon ion laser. To reduce dye bleaching and photodamage, only 1-4% of the laser power and a resonance scanning mirror was used. Fluorescence emission between 500 and 600 nm was captured using a variable band bass system. Data was recorded after averaging 8 or 4 frames to get a final acquisition frequency of 1 or 2 Hz with 1024 x 1024 pixels resolution. Recordings were obtained 50-100 µm below the slice surface to avoid damaged cells.

Ca^{2+}-free solution was the same as ACSF with the omission of 2 mM $CaCl_2$ and the addition of 5 mM EGTA. Stock solutions of ATP and UTP were prepared in ACSF solution at 30 mM and 100 mM respectively and stored at -20℃. Chemicals were purchased form Sigma-Aldrich, unless otherwise stated.

Imaging data analysis

Changes in fluorescence were measured in regions of interest (ROIs) drawn around a single supporting cell using ImageJ 1.51s (NIH). Small drift in the recording was correct using the StackReg plug-in of ImageJ. Data are presented as normalized fluorescence changes, $\Delta F/F_0=(F(t)-F_0)/F_0$, where F_0 was the average of fluorescence intensity before the application of the first stimulus and F(t) was the fluorescence amplitude at time t. Further analysis and figures were made with IgorPro 6.3.7.2 (Wavemetrics). In some experiments, the reduction of fluorescence signal due to photobleaching was mathematically corrected using the exponential decay observed in non-responding cells (Thomas et al., 2000). We considered a cell responsive if: (i) there was no spontaneous activity, (ii) after stimulation $\Delta F/F_0$ was higher than the average of the prestimulus (10 s time window) plus five standard deviation for at least 3 seconds, (ii) there was no response to ACSF solution application.

RESULTS

VNO supporting cells express purinergic ATP receptors

Supporting cells of the VNO can be identified by their morphology and localization in the vomeronasal sensory epithelium. The supporting cells have a columnar cell body and form a monolayer at the apical surface of the epithelium. The top panel of Figure 1A show the apical monolayer of column shaped cells, which correspond to somata of supporting cells.

Application of 30 µM ATP to the VNO slices loaded with Cal-520AM lead to transient Ca^{2+} responses in supporting cells (Figure 1). Figure 1A shows a sequence of confocal images recorded from VNO slices, before (1), at the peak of (2) and after (3) the ATP induced response. Representative traces of the normalized fluorescence change ($\Delta F/F_0$) from the three supporting cells highlighted in the top panel of Figure 1A are shown in Figure 1B. The application of ACSF solution as a control for possible perfusion artifacts did not significantly change the Cal520 fluorescence. In contrast, 30 µM ATP induced a transient increase of intracellular calcium concentration. Recordings from several slices showed that about 85% of the supporting cells (157 of 183) are responsive to the ATP stimulation, indicating that these VNO supporting cells express purinergic ATP receptors (Fig 1C).

A subset of VNO supporting cells express metabotropic purinergic receptors

To determine if the Ca^{2+} response to ATP in VNO supporting cells is mediated by ionotropic (P2X) or (P2Y) metabotropic ATP receptors (Nishimura et al., 2017), we conducted a series of experiments in which we examined if the presence of extracellular Ca^{2+} is necessary for the generation of these Ca^{2+} transients induced by ATP. Figure 2 A shows representative traces of the normalized fluorescence change from two different VNO supporting cells. In the cell shown at the top, 30 µM ATP was still able to induce a significant increase in intracellular Ca^{2+}, even when the slice was perfused with Ca^{2+}-free ACSF solution, suggesting that ATP evokes a release of Ca^{2+} from intracellular stores mediated by the activation of metabotropic ATP receptors. In contrast, in the other cell ATP induced a Ca^{2+} signal only in the presence of extracellular Ca^{2+}, indicating that ATP caused an influx of Ca^{2+} by the activation of ionotropic receptors. Recordings from several slices show that 75% of the cells (39 of 52) responded to ATP application with a transient increase of intracellular Ca^{2+} in the absence of extracellular Ca^{2+} (Fig. 2 B), indicating the mobilization of intracellular stores.

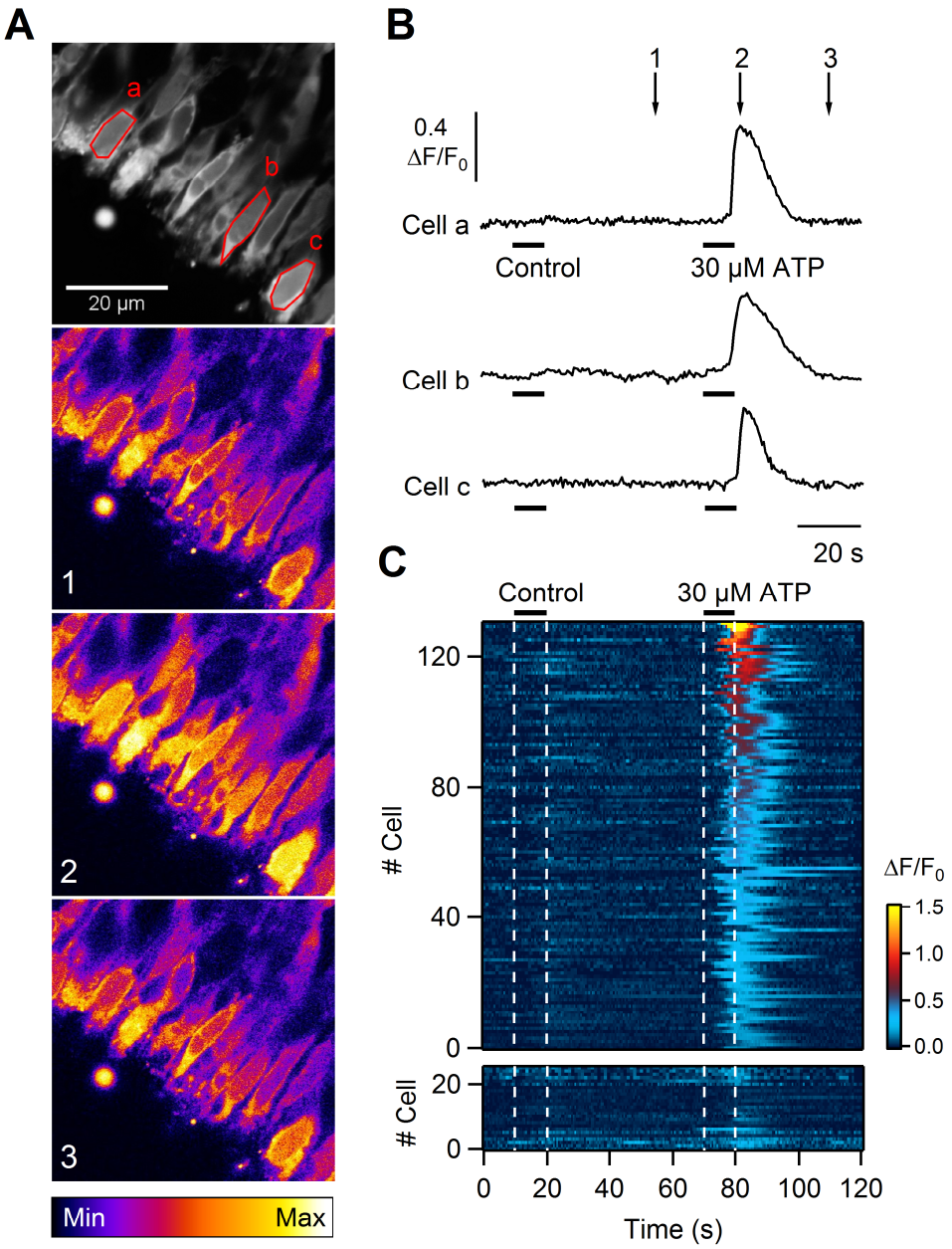

Figure 1. ATP stimulation induces Ca^{2+} signal in VNO supporting cells. (A) Confocal images in pseudocolor from a Cal 520-AM loaded VNO slice, representing the sequence of events, before (1), at the peak of (2), and after (3) the response induced by stimulation with 30 µM ATP for 10 s. The top panel shows the median of fluorescence intensity of all frames in the recording and it was used to better recognize supporting cells morphology, and to identify and delimit individual cells. (B) Calcium transients recorded in the cells highlighted in the top panel of A, showing the response to 30 µM ATP stimulation but not to the control with ACSF. Time points identified by arrows correspond to the frames numbered in A. (C) Heat map of the normalized change in fluorescence intensity following stimulation with ACSF and 30 µM ATP. Data is sorted for the largest response. Dashed lines and black bar delimit the stimuli delivery period. The lower panel shows the non-responding cells.

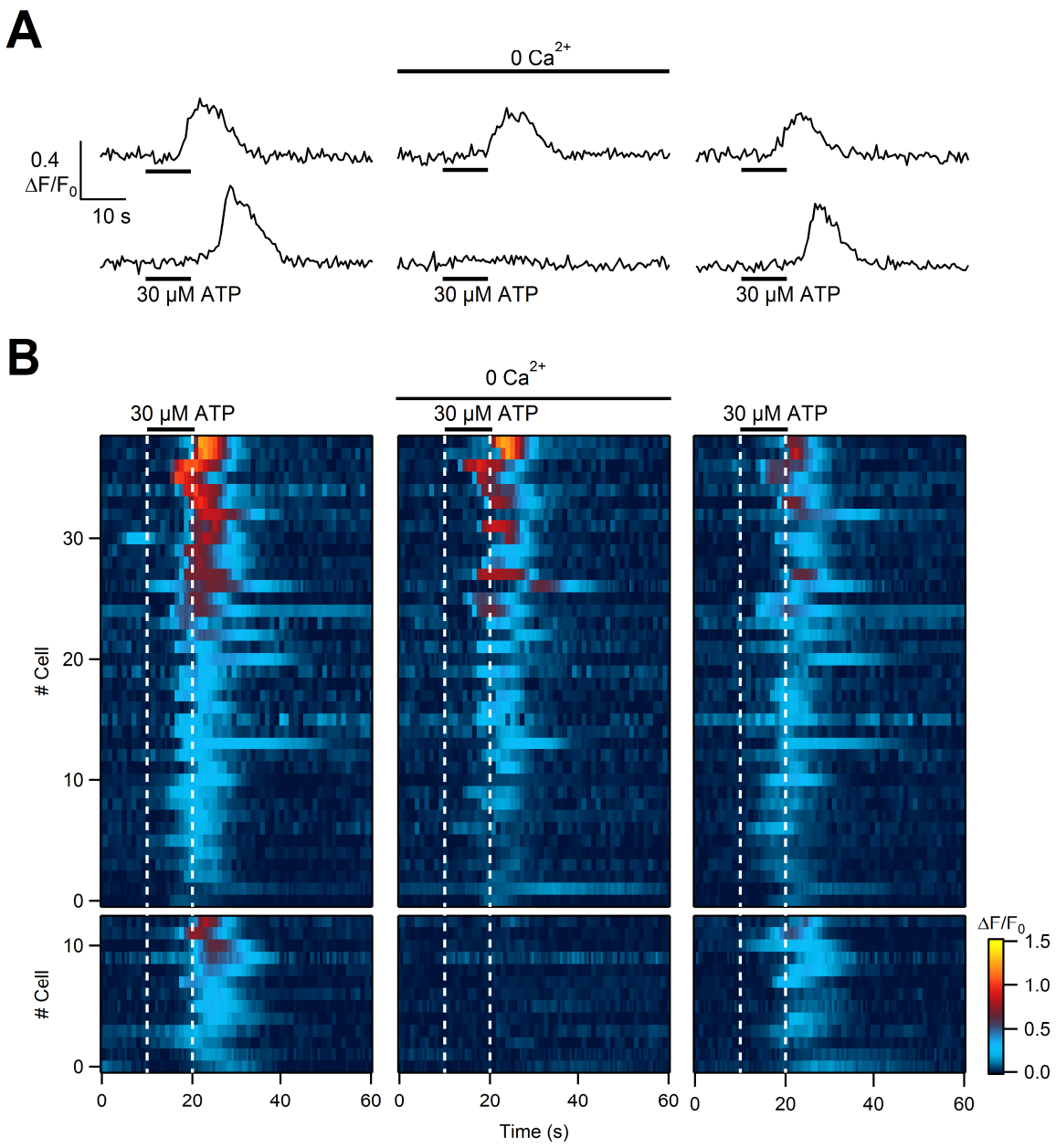

Figure 2 Absence of extracellular Ca^{2+} ATP-induced Ca^{2+} signal in a subpopulation of VNO supporting cells. (A) Representative calcium transients recorded from two different VNO supporting cells repeatedly stimulated with 30 μM ATP in control ACSF solution or in the absence of extracellular Ca^{2+}. (B) Heat map of the normalized change in fluorescence intensity following stimulation with 30 μM ATP in control ACSF solution or in the absence of extracellular Ca^{2+}. Data are sorted by the largest response to the first application of ATP. Dashed lines and black bar delimit stimuli delivery period. The lower panels show the non-responding cells upon ATP stimulation in the absence of extracellular Ca^{2+}.

To further narrow down the identity of the purinergic receptors functionally expressed in supporting cells of the VNO, we examined if ATP responsive supporting cells respond also to UTP (Figure 3). UTP has been shown to activate only the metabotropic P2Y2 and P2Y4 receptors (Nishimura et al., 2017). Figure 3 A shows representative traces of the normalized fluorescence change from two different VNO supporting cells. In the cell at the top, both 30 µM ATP and 20 µM UTP induced a significant increase in intracellular Ca^{2+}. In contrast, in the other cell, only ATP evoked a Ca^{2+} signal, while UTP failed to induce a significant increase of intracellular Ca^{2+} concentration. Recordings from several slices show that about 38% of the ATP-responsive cells (33 of 87) responded also to UTP.

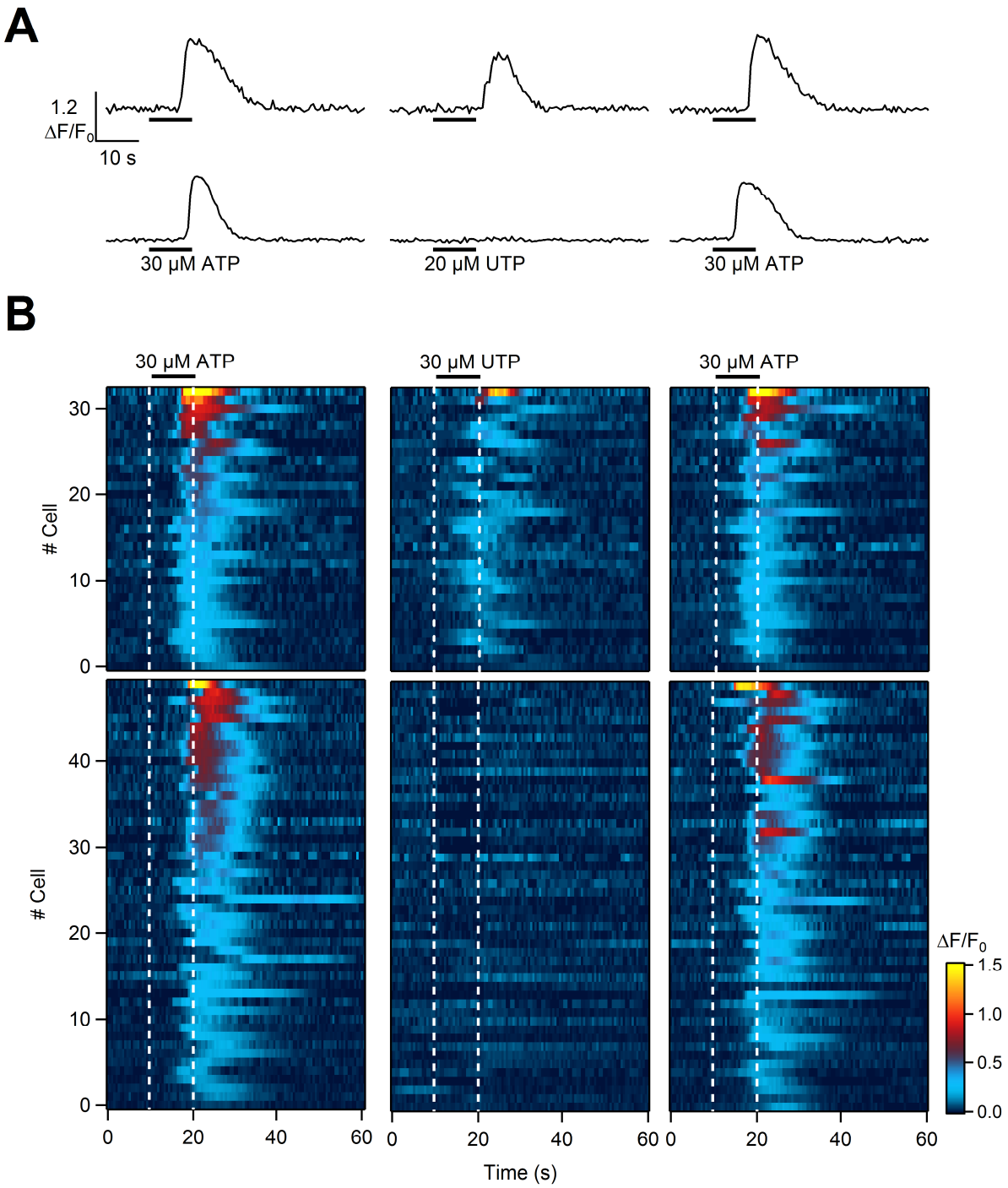

Figure 3 UTP stimulation induces Ca2+ signal in a subset of ATP-responsive VNO supporting cells.

(a) Representative calcium transients recorded from two different VNO supporting cells repeatedly stimulated with 30 μM ATP or with 20 μM UTP. (B) Heat map of the normalized change in fluorescence intensity following stimulation with 30 μM ATP or with 20 μM UTP Ca2+. Data are sorted by the largest response to the first application of ATP. Dashed lines and black bar delimit stimuli delivery period. The lower panels show the non-responding cells upon UTP stimulation.

REFERENCES

Nishimura, A., Sunggip, C., Oda, S., Numaga-Tomita, T., Tsuda, M., and Nishida, M. (2017). Purinergic P2Y receptors: Molecular diversity and implications for treatment of cardiovascular diseases. Pharmacol, Ther. *180*, 113-128.

Shimazaki, R., Boccaccio, A., Mazzatenta, A., Pinato, G., Migliore, M., and Menini, A. (2006). Electrophysiological properties and modeling of murine vomeronasal sensory neurons in acute slice preparations. Chem. Senses *31*, 425–435.

Thomas, D., Tovey, S.C., Collins, T.J., Bootman, M.D., Berridge, M.J., and Lipp, P. (2000). A comparison of fluorescent Ca2+ indicator properties and their use in measuring elementary and global Ca2+ signals. Cell Calcium *28*, 213-233.

4. Conclusions

Previous studies conducted in our lab showed that TMEM16A, a calcium-activated chloride channel, is expressed in the microvilli of the supporting cells of the olfactory epithelium (Maurya and Menini, 2014). The supporting cells form a columnar monolayer on the most apical part of the olfactory epithelium and they protrude many microvilli towards the luminal surface intermingling with the cilia of olfactory sensory neurons, completely covering the surface of the olfactory epithelium. Supporting cells share properties of both glial cells and epithelial cells, and they have been shown to be involved in xenobiotic metabolism and phagocytosis of dead neurons.

In the first part of this project, we investigated if the genetic ablation of TMEMA alter the development of olfactory epithelium. Using immunohistochemical approach, we analyzed the morphology of different cellular components of the olfactory epithelium starting E12.5. We did not observe significant differences in the morphology of olfactory sensory neurons and supporting cells from wt and TMEM16A knockout mice. Since previous studies have shown that TMEM16A is involved in cell proliferation (Oh and Jung, 2016), we also investigated if the lack of TMEM16A alters the regeneration in the olfactory epithelium. Using specific marker for different cell type we found no significant differences in the number of mature olfactory sensory neurons, supporting cell and globose or horizontal basal cells, indicating that TMEM16A in the olfactory epithelium was not connected with proliferation.

In the second part of the project, we used an electrophysiological approach to functional characterize the supporting cells of the olfactory epithelium. We found that in the majority of the supporting cells is present a calcium-activated chloride current which resembled the properties of TMEM16A. Using TMEM16A knock out mice we found that this current was completely abolished showing that TMEM16A expression is necessary to mediate the calcium-activated chloride current in the supporting cells of the olfactory epithelium. Previous work found that stimulation of supporting cells with ATP or UTP was able to induce an increase of intracellular calcium concentration by the release of calcium from internal stores mediated by the activation of metabotropic ATP receptors (Hegg et al., 2009). We found that the stimulation with extracellular 30 µM ATP resulted in an increase of intracellular calcium concentration, which is high enough to allow the opening of the TMEM16A channel and the

activation of a chloride current. Additional experiments will be necessary to understand the physiological role of TMEM16A–mediated current in the olfactory epithelium.

Finally we started the first investigation of calcium signaling in the supporting cells of mouse vomeronasal sensory epithelium. We were able to demonstrate that also these supporting cells express purinergic ATP receptors, responding to the stimulation with 30 µM extracellular ATP with a transient increase in intracellular calcium concentrations. Moreover, we found that in 75% of these responsive cells ATP-induced calcium transients are mediated by metabotropic purinergic receptors, as the response was still present in the absence of extracellular calcium, indicating that the intracellular calcium increase results from the recruitment of intracellular calcium stores. We were able to further narrow down the identity of the purinergic receptors involved in this calcium transients by the observation that about 38% of these ATP-responsive cells are also UTP-responsive, which indicates that a subset of VNO supporting cells express a combination of P2Y2 and/or P2Y4 receptors. Further investigation will clarify the physiological or pathological conditions of the release of ATP and the possible function of ATP-mediate calcium signaling in sensory response of the VNO.

5. References

Ablimit, A., Matsuzaki, T., Tajika, Y., Aoki, T., Hagiwara, H., and Takata, K. (2006). Immunolocalization of water channel aquaporins in the nasal olfactory mucosa. Arch. Histol. Cytol. *69*, 1–12.

Amiry-Moghaddam, M., Williamson, A., Palomba, M., Eid, T., de Lanerolle, N.C., Nagelhus, E.A., Adams, M.E., Froehner, S.C., Agre, P., and Ottersen, O.P. (2003). Delayed K+ clearance associated with aquaporin-4 mislocalization: phenotypic defects in brains of alpha-syntrophin-null mice. Proc. Natl. Acad. Sci. U. S. A. *100*, 13615–13620.

Amjad, A., Hernandez-Clavijo, A., Pifferi, S., Maurya, D.K., Boccaccio, A., Franzot, J., Rock, J., and Menini, A. (2015). Conditional knockout of TMEM16A/anoctamin1 abolishes the calcium-activated chloride current in mouse vomeronasal sensory neurons. J. Gen. Physiol. *145*, 285–301.

Asakawa, M., Fukutani, Y., Savangsuksa, A., Noguchi, K., Matsunami, H., and Yohda, M. (2017). Modification of the response of olfactory receptors to acetophenone by CYP1a2. Sci. Rep. *7*, 10167.

Bellot-Saez, A., Kékesi, O., Morley, J.W., and Buskila, Y. (2017). Astrocytic modulation of neuronal excitability through K+ spatial buffering. Neurosci. Biobehav. Rev. *77*, 87–97.

Benedetto, R., Ousingsawat, J., Wanitchakool, P., Zhang, Y., Holtzman, M.J., Amaral, M., Rock, J.R., Schreiber, R., and Kunzelmann, K. (2017). Epithelial Chloride Transport by CFTR Requires TMEM16A. Sci. Rep. *7*, 12397.

Bodin, P., and Burnstock, G. (2001). Purinergic signalling: ATP release. Neurochem. Res. *26*, 959–969.

Brown, P.D., Davies, S.L., Speake, T., and Millar, I.D. (2004). Molecular mechanisms of cerebrospinal fluid production. Neuroscience *129*, 957–970.

Chen, X., Fang, H., and Schwob, J.E. (2004). Multipotency of purified, transplanted globose basal cells in olfactory epithelium. J. Comp. Neurol. *469*, 457–474.

Choi, R., and Goldstein, B.J. (2018). Olfactory epithelium: Cells, clinical disorders, and insights from an adult stem cell niche. Laryngoscope Investig. Otolaryngol. *3*, 35–42.

Coles, J.A., and Orkand, R.K. (1983). Modification of potassium movement through the retina of the drone (Apis mellifera male) by glial uptake. J. Physiol. *340*, 157–174.

Connors, B.W., and Long, M.A. (2004). Electrical synapses in the mammalian brain. Annu. Rev. Neurosci. *27*, 393–418.

Dauner, K., Lissmann, J., Jeridi, S., Frings, S., and Möhrlen, F. (2012). Expression patterns of anoctamin 1 and anoctamin 2 chloride channels in the mammalian nose. Cell Tissue Res. *347*, 327–341.

David, Y., Cacheaux, L.P., Ivens, S., Lapilover, E., Heinemann, U., Kaufer, D., and Friedman, A. (2009). Astrocytic dysfunction in epileptogenesis: consequence of altered potassium and glutamate homeostasis? J. Neurosci. Off. J. Soc. Neurosci. *29*, 10588–10599.

Davidson, J.S., and Baumgarten, I.M. (1988). Glycyrrhetinic acid derivatives: a novel class of inhibitors of gap-junctional intercellular communication. Structure-activity relationships. J. Pharmacol. Exp. Ther. *246*, 1104–1107.

Dibattista, M., Amjad, A., Maurya, D.K., Sagheddu, C., Montani, G., Tirindelli, R., and Menini, A. (2012). Calcium-activated chloride channels in the apical region of mouse vomeronasal sensory neurons. J. Gen. Physiol. *140*, 3–15.

Dittrich, K., Sansone, A., Hassenklöver, T., and Manzini, I. (2014). Purinergic receptor-induced Ca2+ signaling in the neuroepithelium of the vomeronasal organ of larval Xenopus laevis. Purinergic Signal. *10*, 327–336.

Eisthen, H.L. (1992). Phylogeny of the vomeronasal system and of receptor cell types in the olfactory and vomeronasal epithelia of vertebrates. Microsc. Res. Tech. *23*, 1–21.

Elsaesser, R., and Paysan, J. (2007). The sense of smell, its signalling pathways, and the dichotomy of cilia and microvilli in olfactory sensory cells. BMC Neurosci. *8 Suppl 3*, S1.

Ferrera, L., Caputo, A., Ubby, I., Bussani, E., Zegarra-Moran, O., Ravazzolo, R., Pagani, F., and Galietta, L.J.V. (2009). Regulation of TMEM16A chloride channel properties by alternative splicing. J. Biol. Chem. *284*, 33360–33368.

Fletcher, R.B., Das, D., Gadye, L., Street, K.N., Baudhuin, A., Wagner, A., Cole, M.B., Flores, Q., Choi, Y.G., Yosef, N., et al. (2017). Deconstructing Olfactory Stem Cell Trajectories at Single-Cell Resolution. Cell Stem Cell *20*, 817-830.e8.

Francia, S., Pifferi, S., Menini, A., and Tirindelli, R. (2014). Vomeronasal Receptors and Signal Transduction in the Vomeronasal Organ of Mammals. In Neurobiology of Chemical Communication, C. Mucignat-Caretta, ed. (Boca Raton (FL): CRC Press/Taylor & Francis), p.

Gayle, S., and Burnstock, G. (2005). Immunolocalisation of P2X and P2Y nucleotide receptors in the rat nasal mucosa. Cell Tissue Res. *319*, 27–36.

Getchell, M.L., Zielinski, B., and Getchell, T.V. (1988). Odorant and Autonomic Regulation of Secretion in the Olfactory Mucosa. In Molecular Neurobiology of the Olfactory System: Molecular, Membranous, and Cytological Studies, F.L. Margolis, and T.V. Getchell, eds. (Boston, MA: Springer US), pp. 71–98.

Ghiaroni, V., Fieni, F., Pietra, P., and Bigiani, A. (2003). Electrophysiological heterogeneity in a functional subset of mouse taste cells during postnatal development. Chem. Senses *28*, 827–833.

Graziadei, P. (1966). The ultrastructure of the motor nerve endings in the muscles of cephalopods. J. Ultrastruct. Res. *15*, 1–13.

Graziadei, P.P., Levine, R.R., and Graziadei, G.A. (1978). Regeneration of olfactory axons and synapse formation in the forebrain after bulbectomy in neonatal mice. Proc. Natl. Acad. Sci. U. S. A. *75*, 5230–5234.

Guengerich, F.P. (1999). Cytochrome P-450 3A4: regulation and role in drug metabolism. Annu. Rev. Pharmacol. Toxicol. *39*, 1–17.

Hansen, A. (2007). Olfactory and solitary chemosensory cells: two different chemosensory systems in the nasal cavity of the American alligator, Alligator mississippiensis. BMC Neurosci. *8*, 64.

Harris, A.L. (2001). Emerging issues of connexin channels: biophysics fills the gap. Q. Rev. Biophys. *34*, 325–472.

Hayoz, S., Jia, C., and Hegg, C. (2012). Mechanisms of constitutive and ATP-evoked ATP release in neonatal mouse olfactory epithelium. BMC Neurosci. *13*, 53.

Hegg, C.C., Greenwood, D., Huang, W., Han, P., and Lucero, M.T. (2003). Activation of purinergic receptor subtypes modulates odor sensitivity. J. Neurosci. Off. J. Soc. Neurosci. *23*, 8291–8301.

Hegg, C.C., Irwin, M., and Lucero, M.T. (2009). Calcium store-mediated signaling in sustentacular cells of the mouse olfactory epithelium. Glia *57*, 634–644.

Hertz, L. (1965). Possible role of neuroglia: a potassium-mediated neuronal--neuroglial--neuronal impulse transmission system. Nature *206*, 1091–1094.

Hille, B. (2001). Ion Channel of Excitable Membranes (Sunderland, MA: Sinauer Asscoiated, Inc).

Hodgkin, A.L., and Huxley, A.F. (1952). A quantitative description of membrane current and its application to conduction and excitation in nerve. J. Physiol. *117*, 500–544.

Huang, F., Rock, J.R., Harfe, B.D., Cheng, T., Huang, X., Jan, Y.N., and Jan, L.Y. (2009). Studies on expression and function of the TMEM16A calcium-activated chloride channel. Proc. Natl. Acad. Sci. U. S. A. *106*, 21413–21418.

References

Keverne, E.B. (1999). The vomeronasal organ. Science *286*, 716–720.

Linforth, R., Martin, F., Carey, M., Davidson, J., and Taylor, A.J. (2002). Retronasal transport of aroma compounds. J. Agric. Food Chem. *50*, 1111–1117.

Liu, B., Linley, J.E., Du, X., Zhang, X., Ooi, L., Zhang, H., and Gamper, N. (2010). The acute nociceptive signals induced by bradykinin in rat sensory neurons are mediated by inhibition of M-type K+ channels and activation of Ca2+-activated Cl- channels. J. Clin. Invest. *120*, 1240–1252.

Lu, D.C., Zhang, H., Zador, Z., and Verkman, A.S. (2008). Impaired olfaction in mice lacking aquaporin-4 water channels. FASEB J. Off. Publ. Fed. Am. Soc. Exp. Biol. *22*, 3216–3223.

Lucero, M.T. (2013). Peripheral modulation of smell: fact or fiction? Semin. Cell Dev. Biol. *24*, 58–70.

Mackay-Sim, A., and Kittel, P. (1991). Cell dynamics in the adult mouse olfactory epithelium: a quantitative autoradiographic study. J. Neurosci. Off. J. Soc. Neurosci. *11*, 979–984.

Mahalik, T.J. (1996). Apparent apoptotic cell death in the olfactory epithelium of adult rodents: death occurs at different developmental stages. J. Comp. Neurol. *372*, 457–464.

Matsuoka, M., Yoshida-Matsuoka, J., Costanzo, R.M., and Ichikawa, M. (2000). Surface changes in the rat vomeronasal epithelium during degeneration and regeneration of sensory receptor cells. Anat. Embryol. (Berl.) *201*, 467–473.

Maurya, D.K., and Menini, A. (2014). Developmental expression of the calcium-activated chloride channels TMEM16A and TMEM16B in the mouse olfactory epithelium. Dev. Neurobiol. *74*, 657–675.

Mazzone, A., Bernard, C.E., Strege, P.R., Beyder, A., Galietta, L.J.V., Pasricha, P.J., Rae, J.L., Parkman, H.P., Linden, D.R., Szurszewski, J.H., et al. (2011). Altered expression of Ano1 variants in human diabetic gastroparesis. J. Biol. Chem. *286*, 13393–13403.

Menco, B.P., Birrell, G.B., Fuller, C.M., Ezeh, P.I., Keeton, D.A., and Benos, D.J. (1998). Ultrastructural localization of amiloride-sensitive sodium channels and Na+,K(+)-ATPase in the rat's olfactory epithelial surface. Chem. Senses *23*, 137–149.

Montani, G., Tonelli, S., Elsaesser, R., Paysan, J., and Tirindelli, R. (2006). Neuropeptide Y in the olfactory microvillar cells. Eur. J. Neurosci. *24*, 20–24.

Nagashima, A., and Touhara, K. (2010). Enzymatic conversion of odorants in nasal mucus affects olfactory glomerular activation patterns and odor perception. J. Neurosci. Off. J. Soc. Neurosci. *30*, 16391–16398.

Nagra, G., Koh, L., Zakharov, A., Armstrong, D., and Johnston, M. (2006). Quantification of cerebrospinal fluid transport across the cribriform plate into lymphatics in rats. Am. J. Physiol. Regul. Integr. Comp. Physiol. *291*, R1383-1389.

Ogura, T., Szebenyi, S.A., Krosnowski, K., Sathyanesan, A., Jackson, J., and Lin, W. (2011). Cholinergic microvillous cells in the mouse main olfactory epithelium and effect of acetylcholine on olfactory sensory neurons and supporting cells. J. Neurophysiol. *106*, 1274–1287.

Oh, U., and Jung, J. (2016). Cellular functions of TMEM16/anoctamin. Pflugers Arch. *468*, 443–453.

Orkand, R.K., Nicholls, J.G., and Kuffler, S.W. (1966). Effect of nerve impulses on the membrane potential of glial cells in the central nervous system of amphibia. J. Neurophysiol. *29*, 788–806.

Pedemonte, N., and Galietta, L.J.V. (2014). Structure and function of TMEM16 proteins (anoctamins). Physiol. Rev. *94*, 419–459.

Pifferi, S., Menini, A., and Kurahashi, T. (2010). Signal Transduction in Vertebrate Olfactory Cilia. In The Neurobiology of Olfaction, A. Menini, ed. (Boca Raton (FL): CRC Press/Taylor & Francis), p.

Ponissery Saidu, S., Stephan, A.B., Talaga, A.K., Zhao, H., and Reisert, J. (2013). Channel properties of the splicing isoforms of the olfactory calcium-activated chloride channel Anoctamin 2. J. Gen. Physiol. *141*, 691–703.

Rash, J.E., Davidson, K.G.V., Kamasawa, N., Yasumura, T., Kamasawa, M., Zhang, C., Michaels, R., Restrepo, D., Ottersen, O.P., Olson, C.O., et al. (2005). Ultrastructural localization of connexins (Cx36, Cx43, Cx45), glutamate receptors and aquaporin-4 in rodent olfactory mucosa, olfactory nerve and olfactory bulb. J. Neurocytol. *34*, 307–341.

Rendic, S., and Di Carlo, F.J. (1997). Human cytochrome P450 enzymes: a status report summarizing their reactions, substrates, inducers, and inhibitors. Drug Metab. Rev. *29*, 413–580.

Reuter, D., Zierold, K., Schröder, W.H., and Frings, S. (1998). A depolarizing chloride current contributes to chemoelectrical transduction in olfactory sensory neurons in situ. J. Neurosci. Off. J. Soc. Neurosci. *18*, 6623–6630.

Rock, J.R., O'Neal, W.K., Gabriel, S.E., Randell, S.H., Harfe, B.D., Boucher, R.C., and Grubb, B.R. (2009). Transmembrane protein 16A (TMEM16A) is a Ca2+-regulated Cl- secretory channel in mouse airways. J. Biol. Chem. *284*, 14875–14880.

Scemes, E., and Giaume, C. (2006). Astrocyte calcium waves: what they are and what they do. Glia *54*, 716–725.

Scholl, U.I., Choi, M., Liu, T., Ramaekers, V.T., Häusler, M.G., Grimmer, J., Tobe, S.W., Farhi, A., Nelson-Williams, C., and Lifton, R.P. (2009). Seizures, sensorineural deafness, ataxia, mental retardation, and electrolyte imbalance (SeSAME syndrome) caused by mutations in KCNJ10. Proc. Natl. Acad. Sci. U. S. A. *106*, 5842–5847.

Shipley, M.T., and Ennis, M. (1996). Functional organization of olfactory system. J. Neurobiol. *30*, 123–176.

Solbu, T.T., and Holen, T. (2012). Aquaporin pathways and mucin secretion of Bowman's glands might protect the olfactory mucosa. Chem. Senses *37*, 35–46.

Somjen, G.G. (2002). Ion regulation in the brain: implications for pathophysiology. Neurosci. Rev. J. Bringing Neurobiol. Neurol. Psychiatry *8*, 254–267.

Sondo, E., Caci, E., and Galietta, L.J.V. (2014). The TMEM16A chloride channel as an alternative therapeutic target in cystic fibrosis. Int. J. Biochem. Cell Biol. *52*, 73–76.

Storan, M.J., and Key, B. (2006). Septal organ of Grüneberg is part of the olfactory system. J. Comp. Neurol. *494*, 834–844.

Strohschein, S., Hüttmann, K., Gabriel, S., Binder, D.K., Heinemann, U., and Steinhäuser, C. (2011). Impact of aquaporin-4 channels on K+ buffering and gap junction coupling in the hippocampus. Glia *59*, 973–980.

Suzuki, J., and Osumi, N. (2015). Neural crest and placode contributions to olfactory development. Curr. Top. Dev. Biol. *111*, 351–374.

Suzuki, J., Yoshizaki, K., Kobayashi, T., and Osumi, N. (2013). Neural crest-derived horizontal basal cells as tissue stem cells in the adult olfactory epithelium. Neurosci. Res. *75*, 112–120.

Suzuki, Y., Takeda, M., and Farbman, A.I. (1996). Supporting cells as phagocytes in the olfactory epithelium after bulbectomy. J. Comp. Neurol. *376*, 509–517.

Swaney, W.T., and Keverne, E.B. (2009). The evolution of pheromonal communication. Behav. Brain Res. *200*, 239–247.

Thiebaud, N., Veloso Da Silva, S., Jakob, I., Sicard, G., Chevalier, J., Ménétrier, F., Berdeaux, O., Artur, Y., Heydel, J.-M., and Le Bon, A.-M. (2013). Odorant metabolism catalyzed by olfactory mucosal enzymes influences peripheral olfactory responses in rats. PloS One *8*, e59547.

Tirindelli, R., Dibattista, M., Pifferi, S., and Menini, A. (2009). From pheromones to behavior. Physiol. Rev. *89*, 921–956.

Vick, J.S., and Delay, R.J. (2012). ATP excites mouse vomeronasal sensory neurons through activation of P2X receptors. Neuroscience *220*, 341–350.

Vogalis, F., Hegg, C.C., and Lucero, M.T. (2005a). Ionic conductances in sustentacular cells of the mouse olfactory epithelium. J. Physiol. *562*, 785–799.

Vogalis, F., Hegg, C.C., and Lucero, M.T. (2005b). Electrical coupling in sustentacular cells of the mouse olfactory epithelium. J. Neurophysiol. *94*, 1001–1012.

Wang, B., Li, C., Huai, R., and Qu, Z. (2015). Overexpression of ANO1/TMEM16A, an arterial Ca2+-activated Cl- channel, contributes to spontaneous hypertension. J. Mol. Cell. Cardiol. *82*, 22–32.

Wang, H., Zou, L., Ma, K., Yu, J., Wu, H., Wei, M., and Xiao, Q. (2017). Cell-specific mechanisms of TMEM16A Ca2+-activated chloride channel in cancer. Mol. Cancer *16*, 152.

Weber, P.A., Chang, H.-C., Spaeth, K.E., Nitsche, J.M., and Nicholson, B.J. (2004). The permeability of gap junction channels to probes of different size is dependent on connexin composition and permeant-pore affinities. Biophys. J. *87*, 958–973.

Wei, C.-J., Xu, X., and Lo, C.W. (2004). Connexins and cell signaling in development and disease. Annu. Rev. Cell Dev. Biol. *20*, 811–838.

References

Weiler, E., and Farbman, A.I. (1997). Proliferation in the rat olfactory epithelium: age-dependent changes. J. Neurosci. Off. J. Soc. Neurosci. *17*, 3610–3622.

Weissman, T.A., Riquelme, P.A., Ivic, L., Flint, A.C., and Kriegstein, A.R. (2004). Calcium waves propagate through radial glial cells and modulate proliferation in the developing neocortex. Neuron *43*, 647–661.

Zancanaro, C., Merigo, F., Mucignat-Caretta, C., and Cavaggioni, A. (2002). Neuronal nitric oxide synthase expression in the mouse vomeronasal organ during prenatal development. Eur. J. Neurosci. *16*, 659–664.

Zhang, Y., Wang, X., Wang, H., Jiao, J., Li, Y., Fan, E., Zhang, L., and Bachert, C. (2015). TMEM16A-Mediated Mucin Secretion in IL-13-Induced Nasal Epithelial Cells From Chronic Rhinosinusitis Patients. Allergy Asthma Immunol. Res. *7*, 367–375.

Zhuo, X., Gu, J., Behr, M.J., Swiatek, P.J., Cui, H., Zhang, Q.-Y., Xie, Y., Collins, D.N., and Ding, X. (2004). Targeted disruption of the olfactory mucosa-specific Cyp2g1 gene: impact on acetaminophen toxicity in the lateral nasal gland, and tissue-selective effects on Cyp2a5 expression. J. Pharmacol. Exp. Ther. *308*, 719–728.